

Exotic Superconducting States in FeSe-based Materials

Takasada Shibauchi^{1*}, Tetsuo Hanaguri^{2†}, and Yuji Matsuda^{3‡},

¹Department of Advanced Materials Science, University of Tokyo, Kashiwa 277-8561, Japan

²RIKEN Center for Emergent Matter Science, Wako 351-0198, Japan

³Department of Physics, Kyoto University, Kyoto 606-8502, Japan

High-temperature superconductivity and a wide variety of exotic superconducting states discovered in FeSe-based materials have been at the frontier of research on condensed matter physics in the past decade. Unique properties originated from multiband electronic structure, strongly orbital-dependent phenomena, extremely small Fermi energy, electronic nematicity, and topological aspects, give rise to many distinct and fascinating superconducting states. Here, we provide an overview of our current understanding of the superconductivity of *bulk* FeSe-based materials, focusing on FeSe and the isovalent substituted $\text{FeSe}_{1-x}\text{S}_x$ and $\text{FeSe}_{1-x}\text{Te}_x$. We discuss the highly non-trivial superconducting properties in FeSe, including extremely anisotropic pairing states, crossover phenomena from Bardeen-Cooper-Schrieffer (BCS) to Bose-Einstein-condensation (BEC) states, novel field-induced superconducting phase, and broken time reversal symmetry. We also discuss the evolution of the superconducting gap function with sulfur and tellurium doping, paying particular attention to the impact of quantum critical nematic fluctuations and the topological superconductivity. FeSe-based materials provide an excellent playground to study various kinds of exotic superconducting states.

KEYWORDS: Iron-based superconductors, Electronic nematicity, BCS-BEC crossover, Quantum criticality, FFLO state, Time-reversal symmetry breaking, Topological superconductivity

CONTENTS

1. Introduction

2. Electronic Structure and Phase Diagram

- 2.1 Band structure of FeSe
- 2.2 Electronic nematic state
- 2.3 Nematic quantum critical point (QCP)

3. Superconducting Gap Structure

- 3.1 Bulk measurements
 - 3.1.1 Temperature dependence
 - 3.1.2 Field dependence
- 3.2 Angle resolved photoemission spectroscopy (ARPES)
- 3.3 Scanning Tunneling Microscopy / Spectroscopy (STM / STS)

4. BCS-BEC Crossover

- 4.1 BCS-BEC crossover
- 4.2 Evidence for the crossover in FeSe
 - 4.2.1 Penetration depth
 - 4.2.2 ARPES
 - 4.2.3 Quasiparticle interference (QPI)
 - 4.2.4 Quantum-limit vortex core
- 4.3 Superconducting fluctuations, preformed pairs and pseudogap
 - 4.3.1 Giant superconducting fluctuations
 - 4.3.2 Pseudogap
 - 4.3.3 Evolution of BCS-BEC crossover in $\text{FeSe}_{1-x}\text{S}_x$

5. Exotic Superconducting State Induced by Magnetic Field

- 5.1 Field-induced superconducting phase
- 5.2 FeSe in strong magnetic field
- 5.3 Fulde-Ferrell-Larkin-Ovchinnikov (FFLO) state

5.4 Highly spin polarized field-induced state in the BCS-BEC crossover regime

6. Superconductivity near the Nematic Critical Point

- 6.1 Abrupt change of superconducting gap
- 6.2 Possible ultranodal pair state with Bogoliubov Fermi surface

7. Time Reversal Symmetry Breaking (TRSB)

- 7.1 Effect of nematic twin boundary
- 7.2 Evidence from gap structure
- 7.3 Evidence from muon spin rotation (μSR)
- 7.4 TRSB in the bulk

8. Topological Superconducting State

- 8.1 Topological quantum phenomena
- 8.2 Topological superconductivity and Majorana quasi-particle
- 8.3 Potential platforms for topological superconductivity
- 8.4 Basic properties of $\text{FeSe}_{1-x}\text{Te}_x$
- 8.5 Topological phenomena in $\text{FeSe}_{1-x}\text{Te}_x$
 - 8.5.1 Band structure and ARPES experiments
 - 8.5.2 Majorana bound state (MBS) in the vortex core
 - 8.5.3 Search for other Majorana features

9. Summary

1. Introduction

The discovery of high-temperature superconductivity in iron-pnictide compounds has been a significant breakthrough in the condensed matter community. In 2006, H. Hosono's research group discovered superconductivity at superconducting transition temperature $T_c \approx 6$ K in iron-pnictide LaFePO.¹⁾ By replacing phosphorus with arsenic and by partially substituting oxygen with fluorine, T_c increases to 26 K.²⁾ By replacing La with other rare earth elements, T_c raises up to 56 K.³⁾ The iron-chalcogenide superconductors have also been extensively studied. In particular, iron-selenide

*shibauchi@k.u-tokyo.ac.jp

†hanaguri@riken.jp

‡matsuda@scphys.kyoto-u.ac.jp

FeSe with $T_c \approx 9$ K, discovered by M. K. Wu's group in 2008,⁴⁾ has drawn considerable attention because T_c increases to 37 K under pressure.⁵⁾ Moreover, T_c increases more than 50 K in monolayer FeSe thin films grown on SrTiO₃.⁶⁾ Thus iron-pnictides/chalcogenides became a new class of high- T_c superconductors, knocking the cuprates off their pedestal as a unique class of high- T_c superconductors. There is almost complete consensus that high- T_c superconductivity in these iron-based superconductors cannot be explained theoretically by the conventional electron-phonon pairing mechanism. Thus, the origin of superconductivity is unconventional.^{7–9)}

Iron-based superconductors are two-dimensional (2D) layered materials with metallic Fe-pnictogen/chalcogen tetrahedral FeAs₄ (or P/Se/Te) layers.^{10–13)} The pnictogen/chalcogen atoms reside above and below the Fe layers, alternately, and are located at the center of the Fe-atom squares. There are several different types of iron-pnictide superconductors, which are often abbreviated by the ratio of the elements in their parent compositions and are known, such as 111, 122, 1111 types, and iron-chalcogenide superconductors, such as 11 and 122 types. The parent compounds are metals, in contrast to Mott insulators as parent compounds of the cuprates. Moreover, whereas in cuprates the physics is captured by a single band originating from one $3d_{x^2-y^2}$ -orbital per Cu site, iron-based superconductors have about six electrons occupying the nearly degenerate $3d$ Fe-orbitals. Therefore the systems are intrinsically multiband/multi-orbital systems, and the inter-orbital Coulomb interaction plays an essential role. The Fermi surface in these materials mainly consists of d_{xy} , d_{yz} and d_{xz} orbitals, forming well-separated hole pockets near the center of the Brillouin zone and electron pockets near the zone corners.

The parent compound of iron-pnictides is a spin-density-wave (SDW) metal, which exhibits a transition at T_N .¹⁴⁾ Below T_N , a stripe-type long-range antiferromagnetic (AFM) order sets in, which breaks the lattice four-fold (C_4) rotational symmetry. The high- T_c superconductivity appears when the SDW is suppressed either by chemical substitution or by pressure. The highest T_c is often achieved in the vicinity of an AFM quantum critical point (QCP), where the SDW transition vanishes.¹⁵⁾ Therefore, a pairing mechanism mediated by the exchange of AFM fluctuations, which stem from the intra-atomic Coulomb repulsion associated with the quasinesting between electron and hole pockets, has been widely discussed. This scenario predicts the so-called s_{\pm} order parameter, in which the sign of the superconducting gap changes between the electron and hole pockets of the Fermi surface.^{7–9, 16)}

On the other hand, the orbital degrees of freedom in iron-pnictides give rise to various phenomena. Almost all families of iron-pnictides exhibit a tetragonal-to-orthorhombic structural transition at T_s , which is accompanied by the orbital ordering that splits the degenerate d_{xz} and d_{yz} orbitals.¹⁷⁾ This transition that breaks C_4 symmetry of the crystal lattice is referred to as an electronic nematic transition.¹⁸⁾ This nematic transition is believed to be a result of intrinsic electronic instability because the effect on the electronic properties is much larger than expected based on the observed structural distortion. This nematic transition either precedes or is coincident with the SDW transition, and the endpoint of the nematic tran-

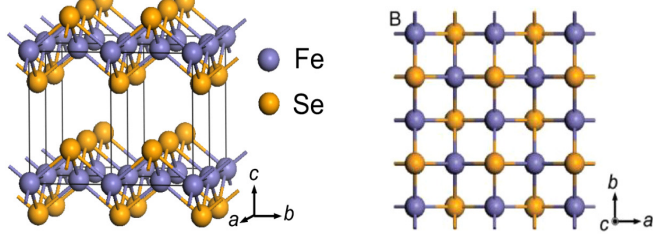


Fig. 1. Crystal structure of FeSe. Adopted from Ref. 4.

sition is located very close to the AFM QCP. Moreover, it has been reported that the electronic nematic order persists even above the superconducting dome in the tetragonal lattice phase in some of the iron-based superconductors.^{19–21)} It has been shown that the nematic susceptibility, which is measured as an induced resistivity anisotropy in response to an external strain,²²⁾ exhibits a divergent behavior at $T \rightarrow 0$ with approaching the endpoint of the structural transition, indicating the presence of a nematic QCP.²³⁾ Consequently, an alternative scenario of the pairing mechanism, which is mediated by orbital fluctuations, has been proposed.²⁴⁾ This scenario can hardly support the s_{\pm} gap function.

Thus a question as to whether the nematic order is driven by spin and/or orbital degrees of freedom has been a topic of intense research, which is intimately related to the driving mechanism of iron-based superconductivity. The nematic correlations intertwined with AFM order in iron-pnictides prevent us from identifying the essential role of nematic fluctuations, raising a fundamental question as to which fluctuations are the main driving force of the Cooper pairing. Identifying the relationship between nematic and SDW orders presents a “chicken-or-egg” problem: Does the SDW order induces the nematic order, or does the nematic order facilitate the SDW order? Although an intricate coupling between magnetic and orbital degrees of freedoms is crucial to understand the underlying physics responsible for their wide variety of exotic properties of iron-pnictides, these questions have been the topic of many debates.^{18, 25–27)} The nematic order is directly linked to the superconductivity because nematic instability is a characteristic feature of the normal state, upon which superconductivity emerges at lower temperatures. Moreover, the nematicity has now been extensively discussed not only in iron-based superconductors but also in cuprates.^{28–34)}

Recently iron-chalcogenide FeSe ($T_c \approx 9$ K) and the isovalently substituted FeSe_{1-x}S_x and FeSe_{1-x}Te_x have become a central system in the research of exotic superconducting states. FeSe is structurally the simplest among the iron-based superconductors, which consists only of a stack of 2D FeSe layers weakly coupled by the van der Waals interaction (see Fig. 1). The experimental progress has been largely accelerated owing to the significant advances in the material quality of FeSe. In particular, the chemical vapor transport technique has enabled us to grow high-quality millimeter-sized single crystals of FeSe free of impurity phases,³⁵⁾ making detailed studies of the intrinsic bulk properties of FeSe possible. FeSe is a strongly correlated semimetal, as revealed by the quasi-particle effective masses determined by the quantum oscillations, angle-resolved photoemission spectroscopy (ARPES)

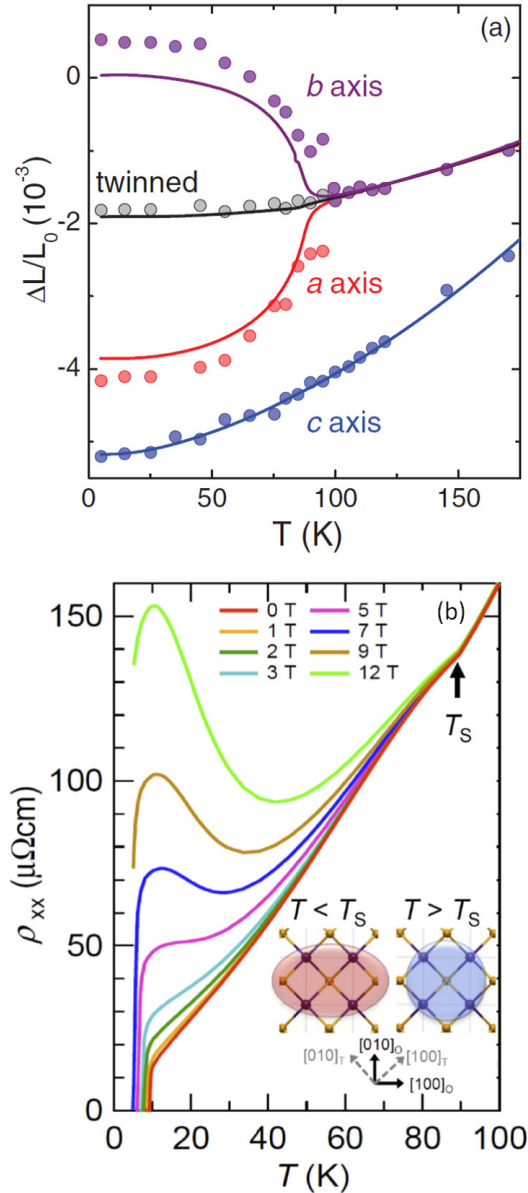


Fig. 2. (a) Temperature dependence of relative length changes along the three axes. Tiny orthorhombic lattice distortion of $\sim 0.2\%$ develops below the nematic phase transition at $T_s \approx 90$ K. This is too small to account for the very large electronic anisotropy discussed in this review, and thus the nematicity is not due to the lattice instability but electronic in origin. Adopted from 35. (b) Temperature dependence of the resistivity of FeSe for $\mathbf{H} \parallel c$.⁹¹⁾ Below T_s , very large magnetoresistance is observed, which is a signature of long mean free path in compensated semimetals. Inset illustrates appearance of the electronic nematicity.

and heat capacity measurements, which are strongly enhanced from those calculated by density functional theory (DFT).

FeSe-based materials provide a unique opportunity to explore the effect of nematicity. FeSe also exhibits a nematic transition at $T_s \approx 90$ K, as shown in Fig. 2. In contrast to iron-pnictides, however, FeSe exhibits no magnetic order down to $T \rightarrow 0$ despite its high T_s , and still its ground state is an unconventional superconducting state. The nematicity is remarkably tunable by hydrostatic pressure P and chemical substitution. In FeSe, the structural (nematic) transition is rapidly suppressed by pressure, and T_s goes to zero at $P \approx 2$ GPa. The AFM static order is induced before the complete suppression of T_s and nematicity appears to coexist with the AFM order. Nuclear magnetic resonance (NMR) and inelastic neutron scattering experiments reveal that the nematicity and magnetism are still highly entangled in FeSe.

The nematicity in $\text{FeSe}_{1-x}\text{S}_x$ is also strongly suppressed with sulfur doping, and T_s goes to zero at $x \approx 0.17$. The nematic fluctuations are strongly enhanced with sulfur doping, and the nematic susceptibility diverges towards absolute zero, revealing the presence of a nematic QCP at $x \approx 0.17$.³⁶⁾ Near the nematic QCP, no sizable AFM fluctuations are observed, indicating that the nematicity is disentangled from magnetic order.

What makes FeSe-based materials distinguished from other superconductors is the unique electronic structure, particularly the extremely shallow Fermi surface associated with very small carrier number, multiband nature and orbital dependent electron correlations. Remarkably, the superconductivity, magnetism and nematicity, all of these most fundamental properties can be largely tuned. Because of these properties, FeSe-based materials serve as not only a model system for the understanding of the influence of the nematicity on the normal and superconducting states, but also a new playground for exotic pairing states, which have been a long standing issue of superconductivity.

In this review article, we shall attempt to bring the readers up to date in the rapidly expanding field of research on the superconductivity of FeSe-based materials, focusing on the *bulk* properties. Excellent reviews of research on atomic layer thin films of FeSe were recently published.^{37,38)} In §2, we discuss the electronic structure and phase diagram of FeSe briefly. We then discuss several topics of active research among exotic superconducting states in FeSe-based materials, such as superconducting gap structure (§3), crossover phenomena from weak coupling Bardeen-Cooper-Schrieffer (BCS) to strong coupling Bose-Einstein condensation (BEC) (§4), magnetic field induced superconducting phase (§5), superconducting state near the nematic QCP (§6), broken time reversal symmetry (§7), and topological superconducting state (§8).

2. Electronic Structure and Phase Diagram

2.1 Band structure of FeSe

First of all, we will not attempt to give an exhaustive survey of current research on the band structure of FeSe in the limited space here. We will direct the reader to more exten-

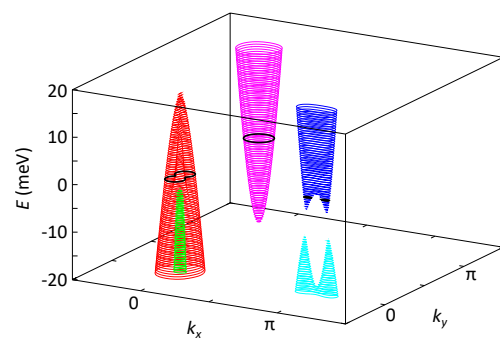


Fig. 3. Schematic energy dispersion of the hole and electron pockets in the nematic phase including spin-orbit interaction. The orbital-dependent energy shift is taken into account so that each band can be fitted to the ARPES data. By courtesy of Y. Yamakawa and H. Kontani.

sive reviews.^{39–41)} As FeSe is a compensated semimetal with equal numbers of electron and hole carriers, it is essentially a multiband superconductor. The Fermi surface consists of well separated hole pockets near the center of the Brillouin zone and electron pockets near the zone corners. Compared with the Fermi surface obtained by the DFT calculations, the actual Fermi surface in the tetragonal phase above T_s is much smaller and dispersions are significantly renormalized.^{42,43)}

In the tetragonal phase, the DFT calculations show three hole pockets,⁴⁴⁾ but ARPES measurements report two pockets, showing that one hole band shifts below the Fermi level. Below the nematic transition at $T_s \approx 90$ K, the orbital ordering lifts the degeneracy of d_{xz} and d_{yz} orbitals. The splitting of the d_{xz} and d_{yz} energy bands is ~ 50 meV at the M_x point in the unfolded Brillouin zone.^{45–50)} Then one hole pocket in the tetragonal phase is shifted below the Fermi level below T_s . As a result, there is only one quasi-2D hole pocket around Γ point in the nematic phase. The hole pocket is strongly distorted to elliptical shape, which consists of d_{yz} orbital along the longer axis and d_{xz} orbital along the shorter axis of the ellipse.

Although the shape and orbital character of the hole pocket appear to be well understood, the consensus about the shape of the electron pockets has not yet been reached. This is mainly because both hole and electron pockets are extremely shallow and therefore high-resolution ARPES measurements are prerequisite to determine the detailed structure of the Fermi surfaces. Unfortunately, such high-resolution ARPES measurements are available only in a limited momentum range around the Γ point. The schematic energy dispersion of the hole and electron pockets in the nematic phase including spin-orbit interaction is shown in Fig. 3.⁵¹⁾ As a result of the finite spin-orbit interaction, Dirac cones around M_x point have a small gap, forming massive Dirac cones. Moreover, the degeneracy at the Γ point of the hole bands is lifted. In this energy shift, there is only one hole pocket around Γ point and one electron pocket around M_y point.

Figures 4(a)–(d) illustrate four possible Fermi surface structures proposed by ARPES and quantum oscillations. Figures 4(a) and (b) show the Fermi surface reported by some ARPES measurements, where the electron pocket has a bow-tie-shape around the M_x point.^{47,50,52,53)} On the other hand, quantum oscillation measurements report the presence of tiny pocket having a non-trivial Berry phase.⁵⁴⁾ This suggests that electron pocket around the M_x point is disconnected, forming the Dirac-core-like band structure, as shown in Fig. 4(c). As shown in Fig. 3, the electron pockets around M_x point shown by red has a fork-tailed shape near the Fermi level. Therefore, the shape of electron pocket strongly depends on the position of the Fermi level, which is expected to be sensitive to the carrier number. Then a slight deviation from the compensation condition may change the shape of the electron pocket dramatically.

Besides these Fermi surfaces, petal-like electron pockets both at M_x and M_y points has also been proposed by some of the ARPES experiments.^{49,55,56)} However, as these ARPES measurements have been performed by using heavily twinned crystals, careful interpretation may be necessary. Recent experiments by using nano-ARPES on twinned crystal report single electron pocket at M_x point shown in Fig. 4 (a) and (b).⁵⁷⁾ The electron pocket at M_y point is also controversial between ARPES measurements using detwinned crystals. While

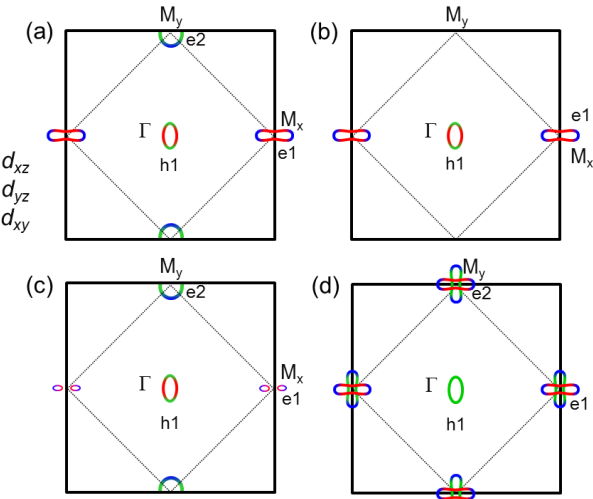


Fig. 4. Four possible Fermi surface structures proposed by ARPES and quantum oscillations. Solid and dotted black lines represent the unfolded and folded Brillouin zone boundaries, respectively. In all the possibilities, there is one hole pocket around the Γ -pocket. For (a), (b) and (c), the hole pocket consists of d_{yz} and d_{xz} orbitals, while for (d), it consists only of d_{xz} orbital. The electron pocket around M_x point has a bow-tie shape for (a) and (b), while electron pocket around M_y point is present for (a) and absent for (b). For (c), the electron pocket around M_x point is disconnected, forming a double Dirac-core-like structure. For (d), petal-like electron pockets appear both at M_x - and M_y points. Note that here the axes are defined as $b < a < c$, which is different from some experimental definition.

a very tiny electron pocket at M_y point is reported⁵³⁾ as illustrated in Fig. 4(a), the absence of such a pocket is reported⁵⁸⁾ as shown in Fig. 4(b). It has been pointed out that the presence or absence of electron pocket at M_y point strongly depends on the level of d_{xy} orbital. Besides the above four types of the Fermi surface, an additional inner hole pocket with d_{xz} orbital character has been suggested very recently.⁵⁹⁾ However, we assume that there is only one hole pocket in the following arguments.

Quantum oscillations of the resistivity, known as Shubnikov-de Haas (SdH) effect, have been reported by several groups.^{43,44)} Four branches are observed in the SdH oscillations. It has been suggested that two of the branches correspond to the extremal orbits of the hole pocket and the other two of the branches correspond to those of electron pocket. The cross section of each Fermi surface is extremely small, which occupies at most 2–3% of the Brillouin zone. The electronic specific heat coefficient γ estimated from the effective masses and Fermi surface volume assuming 2D cylindrical Fermi surface is close to the observed γ -value, suggesting that most parts of the Fermi surface are mapped out by the SdH measurements.⁴⁴⁾

2.2 Electronic nematic state

Pressure and chemical substitution are non-thermal control parameters, which provide a continuous means to modify the electronic structure. The ground state of iron-based materials can be significantly tuned by these parameters, which have been widely employed to access the QCP.¹⁵⁾ The hydrostatic pressure experiments on FeSe have been performed by many groups.^{5,60–69)} As shown in Fig. 5, the structural (nematic) transition at T_s is rapidly suppressed by pressure ($P < 2$ GPa).

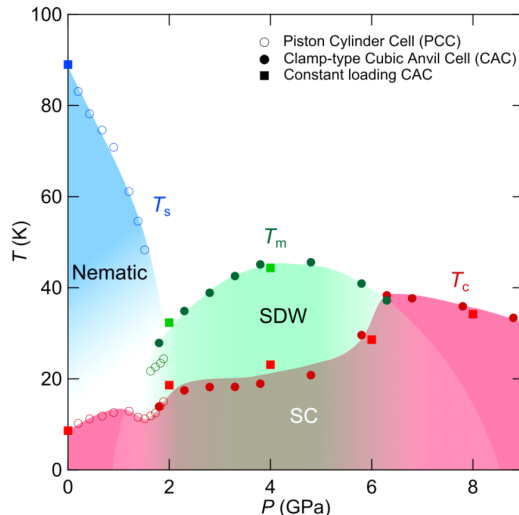


Fig. 5. Pressure-temperature (P - T) phase diagram of FeSe. The structural or nematic (T_s , blue), SDW (T_m , green), and superconducting transition temperatures (T_c , red) as functions of hydrostatic pressure determined by the resistive anomalies measured in the piston-cylinder cell (PCC, open circles), clamp-type cubic anvil cells (CAC, closed circles), and constant-loading type CAC (closed squares). Color shades for the nematic, SDW, and superconducting (SC) states are guides to the eyes. Adopted from Ref. 63.

Before the complete suppression of T_s , the static magnetic order is induced at T_m , suggesting the presence of an overlap region of nematic and pressure-induced magnetic phases. The presence of a static long-range magnetic order has been confirmed by the muon spin rotation (μ SR), Mössbauer spectroscopy and NMR measurements, and the magnetic phase is most likely to be an SDW phase of stripe type similar to the one observed in iron-pnictides. With increasing pressure, T_m increases and intersects with T_s at ~ 2 GPa. At ~ 4.2 GPa, T_m peaks and vanishes abruptly at ~ 6.3 GPa. Thus the pressure-induced magnetic state has a dome-like shape in the P - T phase diagram. It has been reported that superconductivity is filamentary rather than a bulk phenomenon inside the magnetic dome, implying that the ground state in this dome pressure range is likely to be AFM metal. Near the end point of magnetic order, T_c is sharply enhanced up to ~ 38 K.

Electronic nematicity is a ubiquitous property of the iron-based superconductors. There are two scenarios for the driving mechanism of the nematicity. One route to the nematicity is via critical magnetic (spin) fluctuations and the other is via the critical orbital fluctuations. In iron-pnictides, where the nematicity is always accompanied by the AFM order, strong AFM fluctuations are observed above T_s .¹⁴⁾ Then, the critical spin fluctuations have been suggested to be responsible for the nematicity.¹⁸⁾ It has been argued that this spin nematic scenario envisaged in iron-pnictides may be still applicable to FeSe.^{70–73)} In fact, the magnitude of the lattice distortion, elastic softening, and elasto-resistivity associated with the structural transition in FeSe are comparable with those of Fe-pnictides.^{43,74)} It has been shown that the nematic order could be driven by the AFM spin fluctuations without the requirement of magnetic order.^{25,26,72)} Spin excitations measured by the inelastic neutron scattering experiments show that the dynamic susceptibility $\chi(\mathbf{q}, \omega)$ peaks at $\mathbf{q} = (\pi, 0)$, where \mathbf{q} is the scattering vector and $\hbar\omega$ is the energy change between incident and outgoing neutrons. The results suggest the presence

of both stripe and Néel spin fluctuations over a wide energy range even above T_s .^{75,76)} In the nematic state well below T_s , the NMR spin-lattice relaxation rate $1/T_1$ shows the presence of strong AFM fluctuations down to T_c .⁷⁷⁾

There is an alternative scenario where charge or orbital degrees of freedom play a more predominant role than spins.^{43,78–80)} In FeSe, where the nematic transition occurs without magnetic order, no sizable low energy spin fluctuations are observed above T_s by NMR,^{77,78,81)} in contrast to iron-pnictides. It has been shown that the orbital ordering is unequivocally the origin of the nematic order in FeSe.^{45,46,48)} In the nematic phase where the splitting of the d_{xz} and d_{yz} energy bands occurs, a momentum-dependent orbital polarization has been found in ARPES measurements, indicating that the nematicity is most likely to be orbital in origin.⁴⁷⁾ Moreover, NMR measurements report that the difference of the static internal field in the *ab*-plane in the orthorhombic phase at the Se-nucleus is predominantly from the Fe-ion 3d electron orbitals, not from the electron spins.⁸²⁾ Recently, symmetry-resolved electronic Raman scattering measurements provide a direct experimental observation of critical fluctuations associated with electronic charge or orbital nematicity near T_s .⁸³⁾ These results put into question the spin nematic scenario for the nematicity in FeSe.

The appearance of the AFM order induced at low pressure is consistent with the fact that the nematic order is close to the magnetic instability as suggested by *ab initio* calculations.⁸⁴⁾ It has been suggested that the pressure changes the Fermi surface topology of FeSe. A hole band with d_{xy} orbital character is nearly 10 meV below the Fermi level around the (π, π) point in the unfolded Brillouin zone at ambient pressure. The top of the hole band crosses the Fermi energy under pressure, giving rise to a hole pocket. This hole pocket largely enhances the AFM nesting properties, leading to an appearance of the static AFM order.⁸⁵⁾ Therefore the spin and orbital degrees of freedom are highly entangled even in nonmagnetic FeSe, which makes it difficult to pin down the driving mechanism of the nematicity and superconductivity.

Until now, most studies have been conducted in thermal equilibrium, where the dynamical property and excitation can be masked by the coupling with the lattice. Recently, by using femtosecond optical pulse, the ultrafast dynamics of electronic nematicity has been detected. A short-life nematicity oscillation, which is related to the imbalance of Fe d_{xz} and d_{yz} orbitals, has been reported. Such real-time observations of the electronic nematic excitation that is instantly decoupled from the underlying lattice would be important for the future investigation of the nematicity.⁸⁶⁾

2.3 Nematic quantum critical point (QCP)

Next we discuss that $\text{FeSe}_{1-x}\text{S}_x$ is a more suitable system to explore the effect of nematicity disentangled from that of the static AFM order. The nematicity can be tuned continuously by isoelectronic sulfur substitution and T_s vanishes at $x \approx 0.17$. The compensated metal character should be unaffected by the isovalent substitution of Se. Moreover, in contrast to the application of pressure, the sulfur substitution appears not to change the Fermi surface topology.^{87,88)} The NMR $1/T_1$ measurements report that the AFM fluctuations are slightly enhanced at small x but strongly suppressed by further sulfur substitutions, leading to no sizable AFM fluc-

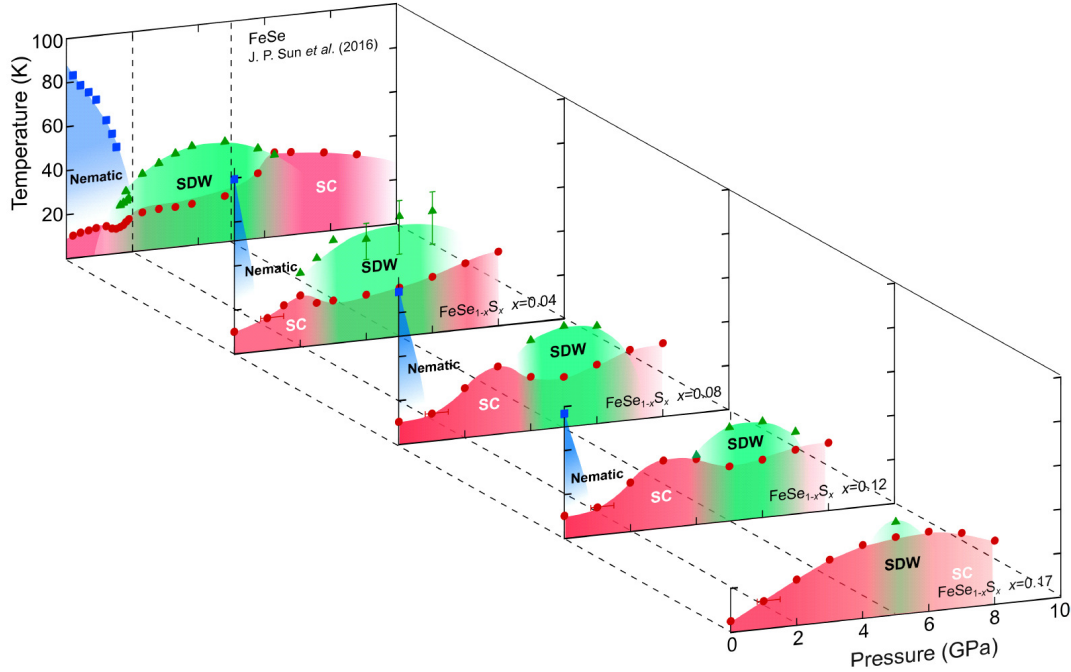


Fig. 6. Temperature-pressure-concentration (T - P - x) phase diagram in $\text{FeSe}_{1-x}\text{S}_x$. The structural or nematic (T_s , blue squares), SDW (T_m , green triangles) and superconducting transition temperatures (T_c , red circles) determined by the resistivity anomalies are plotted against hydrostatic pressure P and sulfur content x . T_c is also determined by the magnetic susceptibility. Adopted from Ref. 64.

tuations near the nematic QCP.^{78,81} Figure 6 displays the temperature-pressure-concentration (T - P - x) phase diagram in $\text{FeSe}_{1-x}\text{S}_x$ in wide ranges of pressure up to 8–10 GPa and sulfur content ($0 \leq x \leq 0.17$), where T_s and T_m are determined by the resistivity anomalies.⁶⁴ The T_c values are determined from the zero resistivity as well as the magnetic susceptibility measurements. As shown in Fig. 6, the magnetic dome shrinks with increasing x , and disappears at $x \approx 0.17$.⁶⁴ This indicates that in contrast to the pressure, sulfur substitution moves the magnetic instability away from the nematic order.

Then an important issue is how the nematic fluctuations evolve with the sulfur substitution. An elegant way to evaluate experimentally the nematic fluctuations has been developed by the Stanford group, that is based on the elasto-resistivity measurements by using a piezoelectric device.²² Nematic susceptibility is defined as $\chi_{\text{nem}} \equiv d\eta/d\epsilon$, where $\eta = (\rho_{xx} - \rho_{yy})/\rho \sim \Delta\rho/\rho$ is the change of the resistivity induced by the lattice strain ϵ . The nematic susceptibility can probe fluctuations associated with the phase transition, which bears some resemblance to the magnetic susceptibility $\chi_{\text{mag}} = dM/dH$ in the magnetic system. It has been reported that χ_{nem} of $\text{FeSe}_{1-x}\text{S}_x$ exhibits the Curie-Weiss like temperature dependence as,

$$\chi_{\text{nem}}(T) = \frac{a}{T - T_\theta} + \chi_0, \quad (1)$$

where a and χ_0 are constants and T_θ corresponds to the Curie-Weiss temperature of the electronic system.³⁶ As shown in Fig. 7, the nematic fluctuations are strongly enhanced with sulfur content x . Near $x \approx 0.17$, T_θ goes to zero, indicating that the nematic susceptibility diverges towards absolute zero. Moreover, quantum oscillations and quasiparticle interference (QPI) measurements reported that the Fermi surface changes smoothly when crossing the nematic QCP. These results re-

veal the presence of a nematic QCP at $x \approx 0.17$.^{87,88}

In the nematic phase, T_c increases gradually, peaks at $x \sim 0.08$ and decreases gradually with x . Around the nematic QCP, T_c decreases and reaches ~ 4 K in the tetragonal

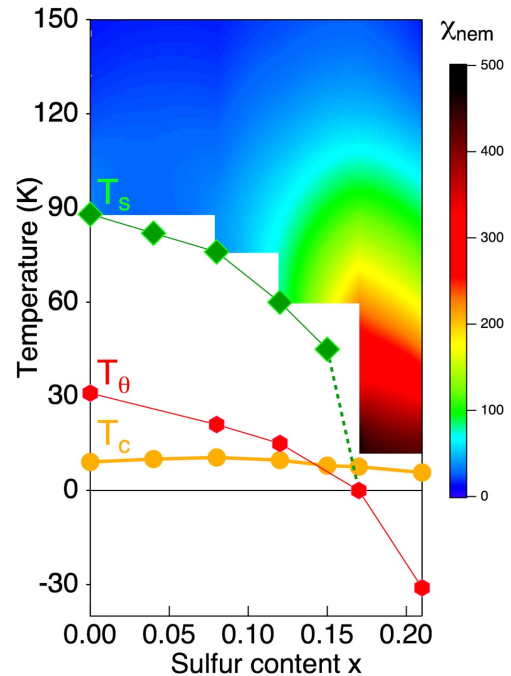


Fig. 7. Phase diagram and quantum criticality in $\text{FeSe}_{1-x}\text{S}_x$. Temperature dependence of the nematic transition (T_s , green diamonds) and the superconducting transition temperature (T_c , orange circles) determined by the zero resistivity criteria. The Curie-Weiss temperature is also plotted (T_θ , red hexagons). The magnitude of χ_{nem} in the tetragonal phase is superimposed on the phase diagram by a color contour (see the color bar for the scale). The lines are the guides for the eyes. Adopted from Ref. 36.

nal phase.^{88,89)} Very recently, linear-in-temperature resistivity, which is a hallmark of the non-Fermi liquid property, is reported at $x \approx 0.17$, indicating that the nematic critical fluctuations emanating from the QCP have a significant impact on the normal-state electronic properties.⁹⁰⁾ We will show that the nematicity also strongly influences on the superconductivity in §6.

3. Superconducting Gap Structure

3.1 Bulk measurements

3.1.1 Temperature dependence

One of the most important properties of unconventional superconductors is the characteristic structure of the superconducting gap $\Delta(\mathbf{k})$, which is intimately related to the pairing mechanism. In the phonon-mediated conventional superconductivity, the momentum-independent pairing interaction leads to BCS s -wave superconductivity with a constant $\Delta = 1.76k_B T_c$, and thus the bulk physical quantities that are related to quasiparticle excitations show exponential temperature dependence at low temperatures. For unconventional superconductors, however, the pairing interaction may have strong dependence on momentum \mathbf{k} leading to anisotropic $\Delta(\mathbf{k})$, which sometimes have zeros (nodes) at certain \mathbf{k} directions. In such cases, the existence of low-lying excitations in the quasiparticle energy spectrum changes the exponential temperature dependence to power-law behaviors. Therefore the low-temperature measurements of bulk quantities sensitive to low-energy quasiparticle excitations, such as magnetic penetration depth, specific heat, and thermal conductivity, are quite important to study the pairing mechanism of superconductors.

The temperature dependence of London penetration depth $\lambda(T)$, which is directly related to the number of superconducting electrons, is one of the sensitive probes of thermally excited quasiparticles. When the gap $\Delta(\mathbf{k})$ has line (point) nodes, the low-energy quasiparticle excitation spectrum depends on energy E as $\propto E$ ($\propto E^2$), and thus $\Delta\lambda(T) = \lambda(T) - \lambda(0)$ is proportional to T (T^2) at low temperatures unless the supercurrent direction is always perpendicular to the nodal directions. The precision measurements of penetration depth in the Meissner state by using the tunnel diode oscillator technique at 13 MHz have shown that $\Delta\lambda(T)$ in high-quality single crystals of FeSe has non-exponential, quasi-linear temperature dependence ($\sim T^{1.4}$) at low temperatures below $\sim 0.2T_c$, as shown in Fig. 8(a).⁹¹⁾ This result suggests the presence of line nodes in the superconducting gap. The deviation from the T -linear dependence may be attributed by the impurity scattering or multiband effect (combining nodal and full-gapped bands), which can increase the exponent α from unity in the power-law temperature dependence T^α .

A surface impedance study at higher frequencies of 202 and 658 MHz by using a cavity perturbation technique also reports strong temperature dependence of superfluid density $\rho_s(T) = \lambda^2(0)/\lambda^2(T)$, but as shown in Fig. 8(b), it exhibits a flattening at the lowest temperatures in contrast to the nodal gap behavior.⁹²⁾ The data can be fitted to two gaps with a small minimum gap $\Delta_{\min} \approx 0.25k_B T_c$ in one band. The implications of the presence of two different results, nodal and gap minima, will be discussed later.

The heat capacity is the most fundamental thermodynamic quantity that can also probe the quasiparticle excitations in the

superconducting state. In the analysis of specific heat $C(T)$, the contribution from the phonons that usually depends on temperature as $C \sim T^3$ at low temperatures needs to be subtracted to extract the electronic contribution. This can be done by comparing the data at zero field and above the upper critical field H_{c2} in the normal state. The temperature dependence of electronic specific heat divided by temperature, $C_e/T(T)$, also shows exponential behavior in fully gapped superconductors and T -linear behavior for the gap structure with line nodes, as in the case of $\Delta\lambda(T)$. While the low-temperature data of $C_e/T(T)$ show sometimes multigap behaviors suggesting the presence of a small full gap,^{94–96)} the most recent measurements using high-quality, vapor-grown single crystals clearly indicate the T -linear behavior at low temperatures down to ~ 0.3 K,⁹³⁾ as shown in Figs. 8(c) and (d). This also suggests the presence of line nodes or tiny gap minima in the superconducting gap in FeSe, which is in a similar situation as in the penetration depth studies.

Another sensitive probe of quasiparticle excitations is the thermal conductivity κ , which can be measured in the superconducting state. The temperature dependence of thermal conductivity also has phononic and electronic components, but in the zero-temperature limit κ/T gives a very important information on the superconducting gap structure. As κ/T is proportional to C/T as well as to the mean free path ℓ , $\kappa/T(T \rightarrow 0)$ always vanishes for fully gapped superconductors. This is understood by the fact that in the zero-temperature limit, C/T vanishes while ℓ is limited by the impurity scattering. In contrast, the presence of nodes in the gap leads to small but finite low-energy states due to impurity scattering, thus giving rise to the finite residual $\kappa_0/T \equiv \kappa/T(T \rightarrow 0)$. When the impurity scattering is increased, the residual density of states increases while the mean free path decreases, resulting in essentially no change in residual κ_0/T , which is called universal residual thermal conductivity in nodal superconductors. In FeSe bulk crystals, there are also two kinds of reports with different conclusions as shown in Figs. 8(e) and (f); one shows a sizable κ_0/T suggesting a nodal state,^{89,91)} and the other shows a much smaller residual values of κ_0/T from which the authors concluded a fully gapped state with small gap minima.⁹⁷⁾

3.1.2 Field dependence

Not only the temperature dependence but also the field dependence give important clues on the presence or absence of the superconducting gap nodes. When the magnetic field H is applied to induce vortices inside nodal superconductors, the supercurrent flowing around a vortex affects the quasiparticle energy spectrum through the Doppler shift mechanism $E(\mathbf{k}) \rightarrow E(\mathbf{k}) - \hbar \mathbf{k} \cdot \mathbf{v}_s$ (where \mathbf{v}_s is the supercurrent velocity around the vortex), and enhance the low-energy density of states (DOS). This Doppler shift effect (or Volovik effect) can be seen by a strong increase of specific heat and thermal conductivity in the zero-temperature limit with increasing magnetic field, and in the case of line nodes \sqrt{H} dependence of C_e/T and κ_0/T is expected. In the thermal conductivity study that reports on the absence of κ_0/T , one of the measured crystal clearly shows a strong increase of κ/T with field at low temperatures.⁹⁷⁾ This indicates that the superconducting gap $\Delta(\mathbf{k})$ has very strong momentum dependence even though the gap does not have any zeros; in other words, the minimum

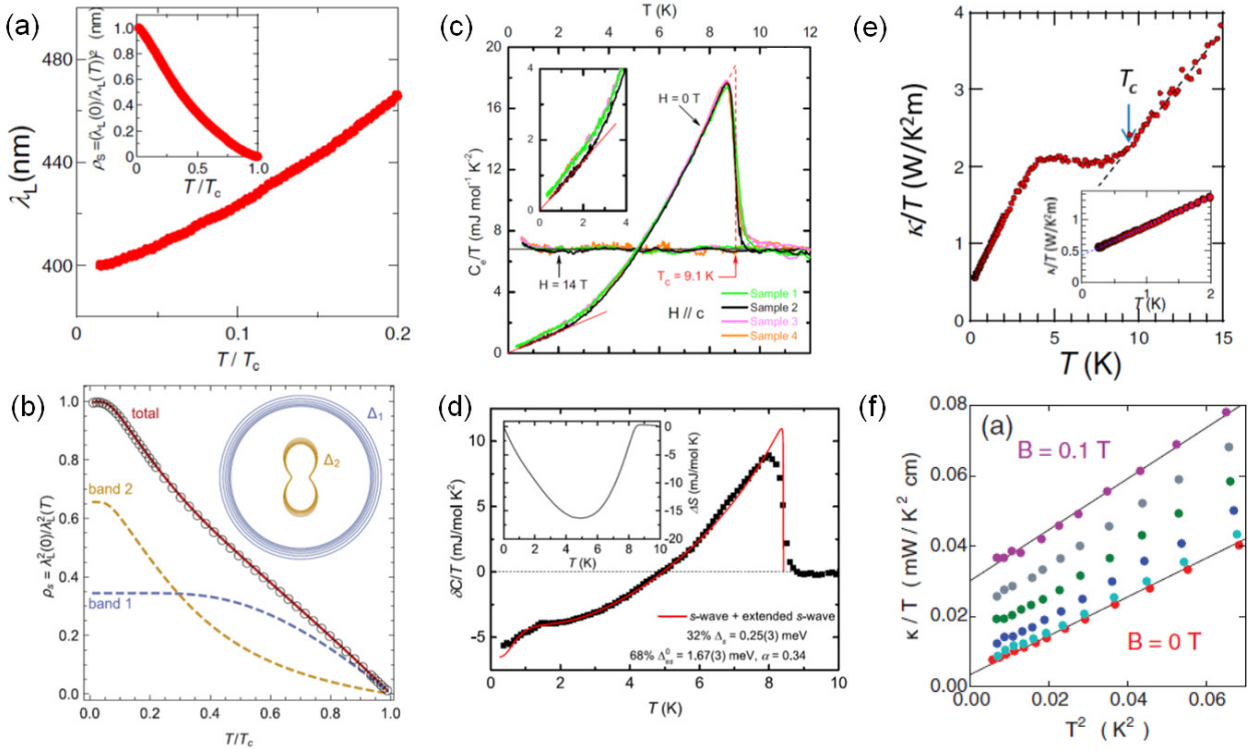


Fig. 8. Temperature dependence of bulk quantities in FeSe single crystals. (a) Temperature dependence of magnetic penetration depth at low temperatures, measured in the Meissner state by a tunnel diode oscillator technique. Adopted from Ref. 91. The inset shows the temperature dependence of superfluid density. (b) Superfluid density measured by a cavity perturbation technique. The data are fitted by a two-gap model (lines). Adopted from Ref. 92. (c) Electronic specific heat divided by temperature C_e/T as a function of temperature in the superconducting state at zero field and in the normal state at 14 T. The inset is an expanded view at low temperatures. Adopted from Ref. 93. (d) The difference of C_e/T between the superconducting and normal states, fitted by a two-gap model (red line). The inset is the temperature dependence of entropy change. Adopted from Ref. 94. (e) Thermal conductivity divided by temperature κ/T as a function of temperature. The inset is an expanded view at low temperatures. Adopted from Ref. 91. (f) κ/T as a function of T^2 at zero and low fields. Here the residual κ_0/T at zero field is an order of magnitude smaller than that in (e). Adopted from Ref. 97.

gap is very small. In the other study showing the presence of κ_0/T , however, the κ_0/T actually decreases with H at low fields.⁹¹⁾ This unusual behavior can be explained by the reduction of mean free path dominating over the increase of DOS, suggesting that the quasiparticles are scattered by vortices. Such scattering induced by vortices may be seen in very clean single crystals with very long ℓ , and in fact a similar reduction of κ_0/T at low fields has been observed in very clean crystals of CeCoIn₅.⁹⁸⁾ In S-substituted crystals of FeSe_{1-x}S_x, where mean free path is naturally suppressed by the chemical substitution, the low-field κ/T at low temperatures exhibits \sqrt{H} behavior, consistent with the presence of line nodes.⁸⁹⁾ In the recent field-dependence measurements of specific heat in FeSe, clear \sqrt{H} dependence of C_e/T is also resolved.⁹³⁾

Summarizing these bulk measurements, one can safely conclude that the superconducting gap structure of bulk FeSe has very strong \mathbf{k} dependence with line nodes or deep gap minima. The fact that some measurements suggest fully gapped behaviors although most results are consistent with the presence of line nodes, implies that the nodes are unlikely protected by symmetry, but are accidental ones. The symmetry protected nodes are robust against impurity scattering, but the accidental nodes may be lifted by various perturbations such as disorder. This is most consistent with the *s*-wave A_{1g} symmetry of the superconducting order parameter, either s_{\pm} or s_{++} , with strong anisotropy in at least one of the multi-bands. This strong anisotropy confirms the unconventional

nature of superconductivity in FeSe.

3.2 Angle resolved photoemission spectroscopy (ARPES)

The ARPES measurements have a strong advantage over other techniques, namely it can provide direct information on the momentum dependence of the energy spectrum. In the superconducting state, the momentum dependence of superconducting gap $\Delta(\mathbf{k})$ can be mapped out, and indeed the *d*-wave superconducting gap has been clearly found in cuprate superconductors. In FeSe with relatively low T_c , however, a very high energy resolution is required to resolve the relatively small energy gap, and a high momentum resolution is also needed to resolve \mathbf{k} dependence around the very small Fermi surfaces. Such high resolution ARPES measurements are available recently by using a laser light source with ~ 7 eV energy. However, this laser-based ARPES measurements, the momentum space that can be accessed is limited near the zone center (Γ point), and the electron bands near the zone edge cannot be explored. The laser ARPES results for single domain samples of FeSe, independently obtained in Institute for Solid State Physics, University of Tokyo,⁹⁹⁾ and Institute of Physics, Chinese Academy of Sciences,¹⁰⁰⁾ show that $\Delta(\mathbf{k})$ in the hole band near the Γ point is strongly anisotropic. The hole Fermi surface has an ellipsoidal shape (see Fig. 3), and $\Delta(\mathbf{k})$ is also two-fold symmetric. They found that along the long axis of the ellipsoid, the gap becomes almost zero suggesting the presence of nodes near this direction, as shown in

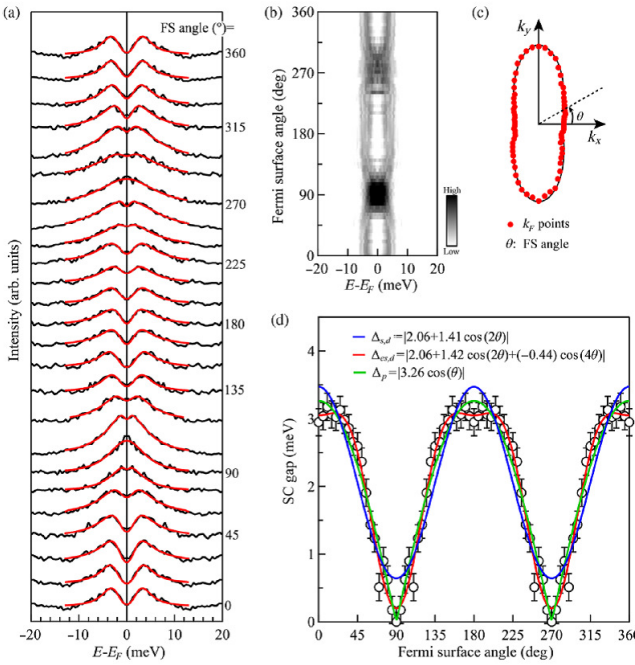


Fig. 9. Momentum dependence of the superconducting gap determined by ARPES measured at 1.6 K. (a) and (b) Symmetrized energy distribution curves at different Fermi momenta along the hole Fermi surface. A phenomenological gap formula (red curves) is used to extract $\Delta(\mathbf{k})$. (c) The location of the Fermi momentum is defined by the Fermi surface (FS) angle θ . (d) Momentum dependence of the superconducting gap, with averaging over the four quadrants. The measured gap (empty circles) is fitted by several gap forms. Adopted from Ref. 100.

Figs. 9(a)-(d). In the two-fold nematic phase, the *s*-wave and *d*-wave components can mix in the A_{1g} symmetry, and the observed two-fold anisotropic $\Delta(\mathbf{k})$ suggests that the *s*-wave and *d*-wave components are very close in magnitude, a pairing state with nascent nodes.¹⁰¹⁾ Although the gap structure of the electron band is not clear from ARPES measurements, this strong anisotropy in the hole band is consistent with the bulk measurements mentioned above.

3.3 Scanning Tunneling Microscopy / Spectroscopy (STM / STS)

The tunneling experiment is a quite powerful probe of superconducting gap structure, because it can extract the quasi-particle DOS as a function of energy in a direct way. Owing to the recent advances of scanning tunneling microscopy / spectroscopy (STM / STS) techniques, one can obtain highly reliable DOS data with a very high energy resolution at very low temperatures. The first evidence from STS for the presence of nodes is reported by Xue group from Tsinghua in thin films of FeSe.¹⁰²⁾ They found a V-shaped DOS in the energy dependence of tunneling conductance near zero energy, consistent with the line nodes in the gap. In bulk vapor-grown single crystals, similar V-shaped tunneling spectra are observed,^{91,103,104)} again suggesting line nodes (Fig. 10(a)). At higher energies, the spectra exhibit at least two distinct features of superconducting gaps at $\Delta_l \approx 3.5$ meV and $\Delta_s \approx 2.5$ meV.

This tunneling spectroscopy alone cannot resolve the positions of nodes in the momentum dependence of gap $\Delta(\mathbf{k})$. However, by analyzing the interference of standing waves in-

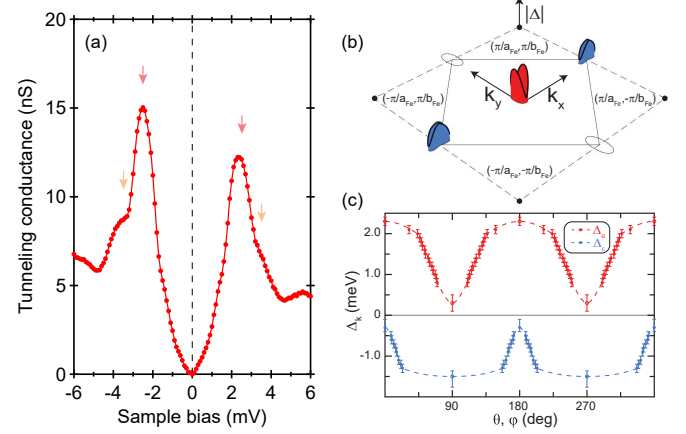


Fig. 10. Superconducting gap structure determined by STS measurements. (a) Typical conductance spectrum measured at 0.4 K at a cleaved surface of FeSe single crystal. The bottom of the gap is V-shaped and there are at least two features at the gap edges as indicated by arrows. Data adopted from Ref. 104. (b) and (c) Momentum dependence of the superconducting gap derived from the QPI analysis. The red and blue colors indicate the different signs of the two gap functions at the hole and electron bands. One of the electron bands has not been deduced from this analysis (thin ellipsoids). Adopted from Ref. 105.

duced by impurity scattering, which is called as Bogoliubov QPI imaging technique, the energy-dependent Fermi surface structures in the scattering wave vector plane can be mapped. From these analyses the superconducting gap structures $\Delta(\mathbf{k})$ of FeSe are extracted, which reveal very strong anisotropies of the gap in the hole band near the zone center as well as one of the electron bands near the zone edge (Fig. 10(b)).¹⁰⁵⁾ In addition, by comparing detailed energy dependence of QPI mapping with theoretical calculations,¹⁰⁶⁾ it is concluded that the sign changing order parameter between the hole and electron bands in FeSe. Although the extracted gap structure has no nodes but deep minima, the suggested pairing state is a strongly anisotropic s_{\pm} state, which has been discussed in terms of orbital-dependent pairing.

Previously, the QPI evidence for the sign-changing s_{\pm} state is found in $\text{FeSe}_{1-x}\text{Te}_x$, where the effect of magnetic field on QPI is analyzed.¹⁰⁷⁾ In $\text{FeSe}_{1-x}\text{Te}_x$, the tunneling spectra are more U-shaped and the gap is more isotropic. This non-universality of superconducting gap structure is also found in iron-pnictides;¹⁵⁾ optimally doped $\text{Ba}_{1-x}\text{K}_x\text{Fe}_2\text{As}_2$ exhibits a fully gapped state while $\text{BaFe}_2(\text{As}_{1-x}\text{P}_x)_2$ shows clear signatures of line nodes. It has also been revealed that in $\text{BaFe}_2(\text{As}_{1-x}\text{P}_x)_2$ system, in which the disorder can be controlled by electron irradiation, the nodes can be lifted by impurity scattering and that the observed non-monotonic changes of low-energy excitations with disorder indicates a sign-changing s_{\pm} state after node lifting.¹⁰⁸⁾ Such non-universal superconducting gap structure with A_{1g} symmetry may indicate the presence and importance of multiple pairing mechanisms in iron-based superconductors, which are most likely based on spin fluctuations that favor s_{\pm} symmetry and orbital fluctuations that favor s_{++} state.

4. BCS-BEC Crossover

4.1 BCS-BEC crossover

An ideal gas consisting of non-interacting Bose particles can exhibit a phase transition, called BEC; below some crit-

ical temperature T_B , a macroscopic fraction of the bosons is condensed into one single ground state. The BEC occurs when the thermal de Broglie wave length ($\propto 1/\sqrt{T}$) becomes comparable to the inter-particle distance $n_B^{-1/3}$ at low temperatures, where n_B is the number of Bose particles. Below T_B , wavefunction interference becomes apparent macroscopically. The superfluidity of the system is a consequence of BEC.

In Fermi systems, attractive interactions between fermions are needed to form bosonic-like molecules (Cooper pairs), which are driven to BEC. There are two limiting cases, weak-coupling BCS and strong-coupling BEC limits, where attractive interactions are weak and strong, respectively. The physics of the crossover between the BCS and BEC limits has been of considerable interest in the fields of condensed matter, ultracold atoms and nuclear physics,¹⁰⁹⁾ giving a unified framework of quantum superfluid states of interacting fermions.^{110–112)} The crossover has hitherto been realized experimentally in ultracold atomic gases.¹⁰⁹⁾ On the other hand, in solid, almost all superconductors are in the BCS regime. In this section, a unique feature of the superconductivity of FeSe is covered. There is growing evidence that FeSe and $\text{FeSe}_{1-x}\text{S}_x$ are in the BCS-BEC crossover regime.^{91, 104, 113, 114)} FeSe-based superconductors may provide new insights into fundamental aspects of the physics of the crossover.

In the BCS limit where the attraction is weak, the Cooper pairing is described as a momentum space pairing. The pairwise occupation of states ($\mathbf{k} \uparrow, -\mathbf{k} \downarrow$) with zero center-of-mass momentum for bosonic-like pairs leads to a profound rearrangement of the Fermi surface, leading to the formation of energy gap Δ , which corresponds to the pair condensation energy. The size of the Cooper pairs, i.e. coherence length ξ , is much larger than the average inter-electron distance $\sim k_F^{-1}$, where k_F is the Fermi momentum, indicating that Cooper pairs are strongly overlapped, $k_F\xi \gg 1$. This corresponds to $\Delta/\varepsilon_F \ll 1$, i.e. the pair condensation energy is much smaller than the Fermi energy. In this regime, the condensation occurs simultaneously with the pair formation. In the BEC limit where the attraction is strong, two electrons are tightly bounded, forming a bound molecule, and the Cooper pairs behave as independent bosons. In this limit, the size of the composite bosons is much smaller than the average inter-electron distance, $k_F\xi \ll 1$; composite bosons are non-overlapping, which can be regarded as a real-space pairing. Even when the pair formation occurs at T^* , the thermal de Broglie wave length is still much shorter than the inter-electron distance. As a result, the BEC transition occurs at T_c , a temperature much lower than the pair formation temperature ($T^* \gg T_c$).

$$T_c = \frac{2\pi}{(\zeta(3/2))^{2/3}} \frac{\hbar(n/2)^{2/3}}{2m} = 0.218T_F, \quad (2)$$

where n is the number of Fermion particles, $\zeta(z)$ is the Riemann zeta function ($\zeta(3/2) = 2.612$), and T_F is the Fermi temperature. Thus, in contrast to the BCS limit, the preformed Cooper pair regime extends over a wide range of temperature (Fig. 11). The appearance of the preformed pairs has been suggested to lead to the pseudogap formation, which is the precursor of the well-developed superconducting gap. The essential defining feature of the real space pairing is that the chemical potential becomes negative ($\mu < 0$), moving below

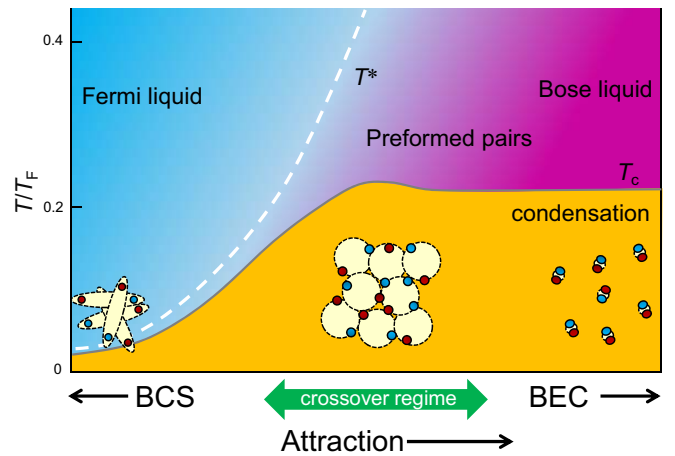


Fig. 11. Canonical phase diagram of the BCS-BEC crossover. With increasing attractive interaction, the superconducting condensation temperature T_c increases in the BCS regime, and becomes independent of interaction in the BEC regime. The dashed white line represents the pairing temperature T^* , where the preformed pairs appear. In the crossover regime, T_c exhibits a broad maximum. As the pairing strength is increased, T_c and T^* are separated. The pseudogap is expected at $T_c < T < T^*$.

the bottom of the band.

The bound energy of a Cooper pair is given by the superconducting gap in the BCS regime, while it is given by the chemical potential in the BEC regime. The excitation energy of the quasiparticles (Bogoliubov quasiparticles) in the superfluid phase of the fermionic condensate is given by

$$E_k = \pm \sqrt{(\varepsilon_k - \mu)^2 + \Delta^2}, \quad (3)$$

where $\varepsilon_k = \hbar^2 k^2 / 2m$ is the electron energy dispersion. In the BCS regime, the chemical potential coincides with the Fermi energy at $T = 0$, $\mu = \varepsilon_F (= \frac{\hbar^2 k_F^2}{2m})$. The minimum of the spectral gap $E_k = \Delta$ opens at $\varepsilon = \mu$ corresponding to $|\mathbf{k}| = k_F$, as displayed in Fig. 12(a). In the BEC regime, where μ is negative, the minimum spectral gap locates at $\mathbf{k} = 0$, as displayed in Fig. 12(b). In this regime where $|\mu| \gg \Delta$, $E_k = \sqrt{\mu^2 + \Delta^2} \approx |\mu|$. Thus the minimum energy that breaks the Cooper pairs is 2Δ and $2|\mu|$ for BCS and BEC regimes, respectively.

The BCS state with cooperative Cooper pairing and BEC state with composite bosons share the same kind of spontaneous symmetry breaking. The change between the two states is a continuous crossover at $T = 0$ ¹¹⁵⁾ and at finite temperature¹¹⁰⁾ connected through a progressive reduction of the size of electron pairs involved as fundamental entities in both phenomena. This crossover goes across the intermediate regime where the size of the pairs is comparable with the average inter-particle distance, $k_F\xi \sim 1$. The BCS-BEC crossover has been extensively studied in the ultracold atomic systems, in which the attractive interaction can be controlled experimentally by a Feshbach resonance,¹⁰⁹⁾ but is extremely difficult to be realized for electrons in solids. The interest in the BCS-BEC crossover has also grown up in high- T_c cuprate,¹¹⁶⁾ in which the size of the pairs appears to be comparable to the inter-particle spacing. In particular, the problem of the preformed pairs has attracted considerable attention in high- T_c cuprates as an origin of the pseudogap formation in the underdoped regime.^{111, 117, 118)} However, the pseudogap and pre-

formed pairs of cuprates remain highly controversial and unresolved issues.¹¹⁹⁾

In FeSe, values of $2\Delta_l/k_B T_c \approx 9$ and $2\Delta_s/k_B T_c \approx 6.5$ for the two gaps observed in spectroscopic measurements are significantly enhanced from the weak-coupling BCS value of 3.5, implying that the attractive interaction holding together the Cooper pairs takes on an extremely strong-coupling nature, as expected in the crossover regime. Recently, it has been suggested that FeSe is deep inside the BCS-BEC crossover regime. Below we discuss experimental signatures that FeSe provides a new platform to study the electronic properties in the crossover regime.

4.2 Evidence for the crossover in FeSe

4.2.1 Penetration depth

The high-quality single crystals of FeSe enable us to estimate the Fermi energies ε_F^e and ε_F^h from the band edges of electron and hole sheets, respectively, by using several techniques. All of them consistently point to extremely small Fermi energies. First we discuss the absolute value of penetration depth in FeSe.

In 2D systems ε_F is related to the London penetration depth $\lambda(0)$ as $\varepsilon_F = \frac{\pi\hbar^2 d}{\mu_0 e^2} \lambda^{-2}(0)$, where d is the interlayer distance.¹²⁰⁾ For FeSe, $\lambda(0) \approx 400$ nm.⁹¹⁾ As the Fermi surface consists of one hole sheet and one (compensating) electron sheet, λ can be written as $1/\lambda_L^2 = 1/(\lambda^e)^2 + 1/(\lambda^h)^2$, where λ^e and λ^h represent the contribution from the electron and hole sheets, respectively. Assuming that two sheets have similar effective masses, $\varepsilon_F^h \sim \varepsilon_F^e \approx 7\text{-}8$ meV is obtained.⁹¹⁾ The magnitude of the Fermi energy can also be inferred from the thermoelectric response in the normal state. From the Seebeck coefficient,¹²¹⁾ the upper limit of ε_F^e is deduced to be ~ 10 meV. These results indicate that both of the Fermi energies of the hole and electron pockets are extremely small.

To place FeSe in the context of other superconductors, T_c is plotted as a function of Fermi temperature $T_F \equiv \varepsilon_F/k_B$ or an equivalent critical temperature T_B for BEC of electron pairs for several materials including FeSe (Uemura plot, Fig. 13).¹¹⁶⁾ Because the relevant Fermi surface sheets are

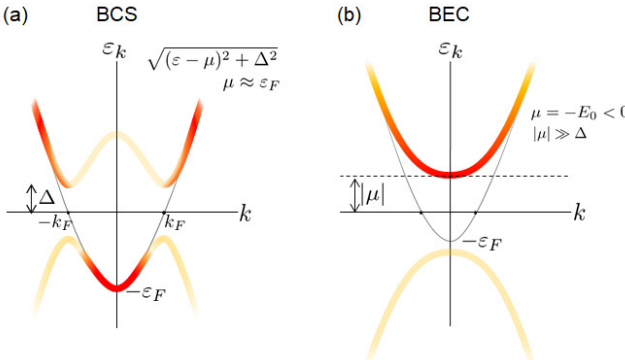


Fig. 12. Dispersion of the Bogoliubov quasiparticle (a) in the BCS and (b) in the BEC regimes for the parabolic electron band in the normal state. Intensity of color represents the spectral weight of the Bogoliubov quasiparticle. In the BCS regime, the minimum of the spectral gap $E_k = \Delta$ occurs at $|k| = k_F$. In the BEC regime, the minimum spectral gap occurs at $k = 0$. The minimum energy that breaks the Cooper pairs is 2Δ and $2|\mu|$ for BCS and BEC regimes, respectively.

nearly cylindrical, T_F for 2D systems may be estimated directly from $\lambda(0)$ via the relation $T_F = \frac{\pi\hbar^2 n_{2D}}{k_B m^*} \approx \left(\frac{\pi\hbar^2 d}{\mu_0 k_B e^2} \right) \lambda^{-2}(0)$, where n_{2D} is the carrier concentration within the superconducting planes and d is the interlayer distance. For three-dimensional (3D) systems, $T_F = (\hbar^2/2)(3\pi^2 n)^{2/3}/k_B m^*$. The dashed line corresponds to the BEC temperature for an ideal 3D Bose gas, $T_B = \frac{\hbar^2}{2\pi m^* k_B} \left(\frac{n}{\zeta(3/2)} \right)^{2/3}$. In a quasi-2D system, this value of T_B provides an estimate of the maximum condensate temperature. Notably, the magnitude of $T_c/T_F \approx 0.10$ of FeSe exceeds that of cuprates and reaches nearly 50% of the value of superfluid ${}^4\text{He}$. It has been shown that T_c/T_F in $\text{BaFe}_2(\text{As}_{1-x}\text{P}_x)_2$ is strikingly enhanced near an AFM QCP at $x_c \approx 0.30$ due to the enhancement of m^* .¹²²⁾ We note that T_c/T_F of FeSe is even larger than that of $\text{BaFe}_2(\text{As}_{1-x}\text{P}_x)_2$ at x_c . Thus Fig. 13 indicates that FeSe is located closer to the BEC line than any other superconductors.

4.2.2 ARPES

As discussed above, in the BCS-BEC regime, the Bogoliubov quasiparticles exhibit a characteristic flat band dispersion near $k = 0$, which is distinctly different from the back-bending behavior at k_F expected in the BCS regime. Such a quasiparticle dispersion can be directly observed by ARPES.

A signature of the BCS-BEC crossover has been reported by ARPES measurements in several iron-based superconductors. In $\text{Ba}_{1-x}\text{K}_x\text{Fe}_2\text{As}_2$ ¹²³⁾ and $\text{LiFe}_{1-x}\text{Co}_x\text{As}$,¹²⁴⁾ the crossover condition $\Delta/\varepsilon_F \sim 1$ has been reported. However, in these compounds, the crossover condition is satisfied only in a minor band with small Fermi energy, and the Fermi energy is much larger than the gap energy in the main bands, $\Delta/\varepsilon_F \ll 1$. In $\text{Fe}_{1+y}\text{Se}_x\text{Te}_{1-x}$, the Δ/ε_F increases and Bogoliubov quasiparticles band changes from BCS-like to flat band like by changing the concentration of excess Fe.¹²⁵⁻¹²⁷⁾ However, in this system, due to the crystal imperfection and

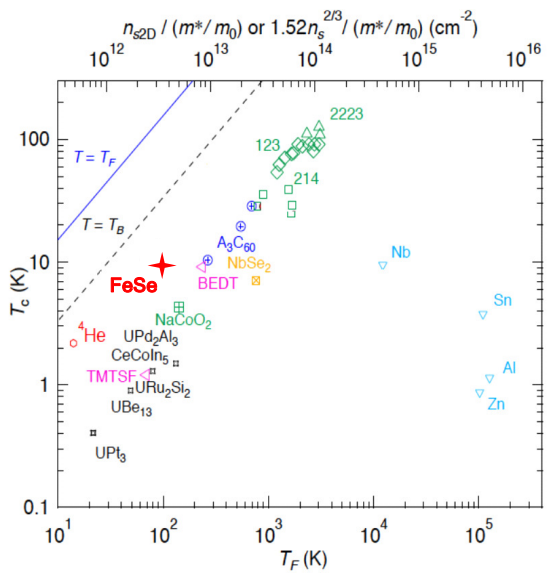


Fig. 13. Uemura plot. T_c is plotted as a function of Fermi temperature T_F evaluated from $1/\lambda^2(0)$ for various 2D and 3D superconductors, including the conventional superconductors such as Nb, high- T_c cuprates such as $\text{La}_{2-x}\text{Sr}_x\text{CuO}_4$ (214), $\text{YBa}_2\text{Cu}_3\text{O}_{7-\delta}$ (123), and $\text{Bi}_2\text{Sr}_2\text{Ca}_2\text{Cu}_3\text{O}_y$ (2223), organic and heavy fermion compounds. The dashed line is the BEC temperature T_B for the ideal 3D Bose gas.

excess Fe-atoms, the superconducting gap is spatially inhomogeneous, compared with $\text{FeSe}_{1-x}\text{S}_x$. In addition, the Fermi energy of electron band is not well known.

Very recently, flat energy dispersions, which are characteristic of the crossover regime, have been reported at the hole pocket in the superconducting state of FeSe. As the Fermi energy of electron pocket in FeSe is much smaller than that of hole pocket, all the bands satisfy the crossover condition.^{91,113)} Moreover, it has been reported that the crossover signature is more pronounced with sulfur substitution. In particular, in $\text{FeSe}_{1-x}\text{S}_x$ with $x = 0.18$ in the tetragonal regime, an unusual quasiparticle dispersion, which is close to that expected in the BEC regime displayed in Fig. 12(b), has been observed.¹¹³⁾

4.2.3 Quasiparticle interference (QPI)

STM/STS can also be used to investigate the electronic dispersions through the QPI effect. The QPI patterns are nothing but the electronic standing waves scattered off defects and appear in the energy-dependent conductance images. Fourier transformation of the conductance images allows us to determine the energy-dependent scattering vectors $\mathbf{q}(E)$, from which one can infer the quasiparticle dispersions in momentum space. Unlike ARPES, QPI can access not only the filled state but also the empty state above ε_F , being useful to explore the electron bands in FeSe.

The QPI patterns of FeSe (Fig. 14) are highly anisotropic due to nematicity. The obtained QPI dispersions consist of one electron branch and multiple hole branches (Fig. 14), and the electron and hole branches disperse along orthogonal axes.^{88,91,128)} There are at least two hole-like QPI branches that cross ε_F , while there is only one hole band at ε_F (§2.1). It has been argued that these two branches come from different k_z states at $k_z = 0$ and $k_z = \pi$.^{88,129)} These QPI signals may be associated with the scattering vectors that correspond to the minor axes of the cross sections of the nematicity-deformed hole and electron Fermi pockets.^{88,91,128)}

Besides these features, one can estimate Fermi energies and Fermi momenta from the QPI dispersions, which faithfully represent the band dispersions. The top and bottom of the hole and electron branches correspond to ε_F^h and ε_F^e , respectively, allowing us to estimate $\varepsilon_F^h \sim 10\text{-}20 meV and $\varepsilon_F^e \sim 5\text{-}10 meV (Fig. 14). The Fermi momenta can be obtained from the scattering vectors at zero energy and are estimated to be $k_F^h \approx 0.5\text{--}0.8$ nm⁻¹ and $k_F^e \approx 0.4$ nm⁻¹ for hole and electron cylinders, respectively. These correspond to the minor axes of the deformed Fermi cylinder and the k_F 's along the major axes may be a few times larger. Such shallow bands are consistent with those reported by the quantum oscillations and ARPES measurements.^{43,44)}$$

STM/STS can also directly evaluate the superconducting-gap size from the tunneling spectrum. As discussed in §3.3, FeSe possesses highly anisotropic superconducting gap and there are at least two distinct superconducting gaps $\Delta_l \approx 3.5$ meV and $\Delta_s \approx 2.5$ meV, which may represent the gaps opening on different Fermi surfaces.^{88,91)} It is still unclear which gap opens on which Fermi surface. Nevertheless, since $\varepsilon_F \lesssim 20$ meV and $\Delta \gtrsim 2.5$ meV, the ratio Δ/ε_F must be larger than 0.1 for both bands, placing FeSe in the BCS-BEC crossover regime. Additional strong support of the BCS-BEC crossover is provided by extremely small $k_F\xi$. Since ξ_{ab} ,

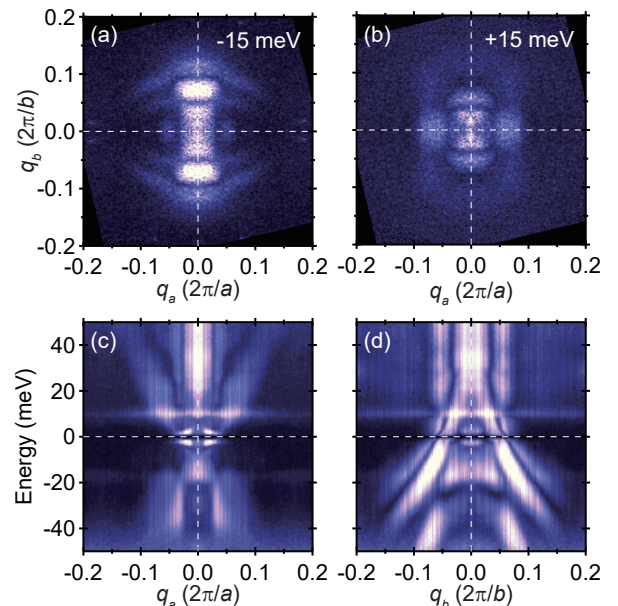


Fig. 14. QPI patterns of FeSe at a low temperature (1.5 K). Magnetic field $\mu_0H = 12$ T was applied along the c axis to suppress superconductivity. (a) and (b) Fourier-transformed normalized conductance images at -15 meV and +15 meV, respectively. Uniaxial patterns are observed due to nematicity. Here, the axes of the orthorhombic unit cell is defined to be $a < b < c$. (c) and (d) QPI dispersions obtained by taking line cuts from the energy-dependent Fourier-transformed QPI patterns along principle axes q_a and q_b in scattering space. Electron-like and hole-like dispersions are identified along q_a and q_b , respectively. Adopted from Ref. 88

which is an average value in 2D plane, determined from the upper critical field (~ 17 T) in perpendicular field ($\mathbf{H} \parallel c$) is roughly 5 nm, $k_F\xi$ should be of the order of unity, again indicating the BCS-BEC crossover superconductivity.

4.2.4 Quantum-limit vortex core

The large value of Δ/ε_F should give rise to novel features in the vortex core. Since the vortex core is a sort of potential well, quantized bound states (Caroli-de Gennes-Matricone states) should be formed inside, as schematically shown in Fig. 15(a). Such vortex-core states can be investigated by STM/STS, in principle. The energies of these states are given by $\pm\mu_c\Delta^2/\varepsilon_F$, where $\mu_c = 1/2, 3/2, 5/2, \dots$ is the quantum number that represents the angular momentum. In the BCS limit, owing to the small ratio of Δ/ε_F , Δ^2/ε_F is order of μeV for most of superconductors so far known. The number of the bound state is roughly ε_F/Δ , which is usually very large, more than 1000. Therefore, because of inevitable smearing effects (e.g. thermal broadening), it is almost impossible to observe the individual Caroli-de Gennes-Matricone states by STM/STS. Instead, a large number of bound states overlap to form a broad particle-hole symmetric peak at zero energy in the tunneling spectrum at the vortex center. With increasing distance from the center, this zero-energy peak splits and continuously approaches to $\pm\Delta$.¹³⁰⁾

By contrast, in the BCS-BEC-crossover regime, ε_F/Δ should be of the order of unity and thus the vortex core accommodates only a few levels, resulting in a so-called quantum-limit vortex.¹³¹⁾ Here, Δ^2/ε_F can become large enough and each bound state may be resolved by STM/STS. Spatial evolution of the bound states should be no longer continuous but

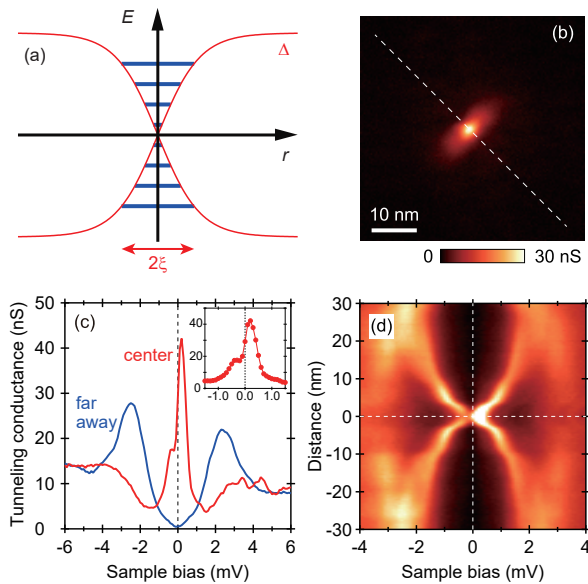


Fig. 15. (a) Schematic energy E diagram of an s -wave superconductor as a function of the distance r from the center of the vortex core. Superconducting gap Δ (red) recovers over the coherence length ξ and the discrete Caroli-de Gennes-Matricon states (blue) are formed in the core region. (b) Zero-energy conductance map showing a single vortex at zero energy at 0.4 K in a magnetic field of 0.25 T along the c axis. (c) Tunneling spectra taken at the vortex center (red) and away from vortices (blue). Inset shows a magnified spectrum at the vortex center. (d) Spatial evolution of tunneling spectra along the dashed in (b). Adopted from Ref. 104

shows the Friedel-like oscillations.¹³¹⁾

Such characteristic signatures of BCS-BEC crossover has been reported in FeSe.¹⁰⁴⁾ Figure 15(b) shows the vortex image of FeSe in a magnetic field of 0.25 T along the c axis. The vortex is elongated due to the nematicity. As shown in Fig. 15(c), the lowest-energy local-DOS (LDOS) peak of FeSe is not at zero energy, representing the lowest bound state in the quantum-limit vortex core. The spatial evolution of the bound states exhibits an oscillatory behavior.¹⁰⁴⁾ The wave length of such spatial oscillations corresponds to π/k_F , being consistent with the theoretical prediction of the Friedel-like oscillations.¹³¹⁾

4.3 Superconducting fluctuations, preformed pairs and pseudogap

4.3.1 Giant superconducting fluctuations

It is well known that Cooper pairs can survive even above T_c as thermally fluctuating droplets. These fluctuations arise from amplitude fluctuations of the superconducting order parameter and have been investigated for many decades.¹³²⁾ It has been shown that their effects on thermodynamic, transport, and thermo-electric quantities in most superconductors are well understood in terms of the standard Gaussian fluctuation theories. However, in the presence of preformed pairs associated with the BCS-BEC crossover, superconducting fluctuations are expected to be strikingly enhanced compared to the Gaussian theories due to additional phase fluctuations.¹¹⁷⁾ Of particular interest is the pseudogap formation, which is the central enigma of the underdoped cuprates.¹¹⁹⁾ The origin of the pseudogap has been discussed in terms of the preformed pairs associated with the crossover phenomenon, which can lead to a partial reduction of the DOS near the Fermi level.¹¹¹⁾

However, it is still highly controversial. Another important issue associated with the BCS-BEC crossover is the breakdown of Landau's Fermi-liquid theory due to the strong interaction between fermions and fluctuating bosons. In ultracold-atomic systems, a Fermi-liquid-like behavior has been reported in thermodynamics even in the crossover regime, but more recent photoemission experiments have suggested a sizable pseudogap opening and a breakdown of the Fermi-liquid description.¹³³⁾

Thus the superconducting fluctuations and pseudogap formation in FeSe are highly intriguing. Superconducting fluctuations give rise to the reduction of the normal-state resistivity. In zero field, $d\rho_{xx}/dT$ of FeSe shows a minimum at around $T^* \sim 20$ K, which can be attributed to the appearance of the additional conductivity due to the fluctuation of the order parameter (paraconductivity) below T^* .¹³⁴⁾ However, a quantitative analysis of the paraconductivity is difficult to achieve because its evaluation strongly depends on the extrapolation of the normal-state resistivity above T^* to lower T . The fluctuation-induced magnetoresistance of FeSe is also difficult to analyze owing to a large and complicated magnetoresistance, which is characteristic of compensated semimetals (see Fig. 2).

The superconducting fluctuations in FeSe have been examined through the magnetic measurements by several groups.^{134–136)} The diamagnetic response due to superconducting fluctuations is clearly observed in the magnetization $M(H)$ for $\mathbf{H} \parallel c$, which exhibits a pronounced decrease below T^* . A crossing point in the diamagnetic response in magnetization, where $M_{\text{dia}}(T, H)$ exhibits a field independent value, is observed near T_c .¹³⁴⁾ Such a crossing behavior is also observed in cuprates, which has been pointed out to be a signature of large superconducting fluctuations.¹³⁷⁾ The fluctuation-induced diamagnetic susceptibility of most superconductors including multiband systems can be well described by the standard Gaussian type (Aslamasov-Larkin) fluctuation susceptibility χ_{AL} , which is given by

$$\chi_{\text{AL}} = -\frac{2\pi^2}{3} \frac{k_B T_c}{\Phi_0^2} \frac{\xi_{ab}^2}{\xi_c} \sqrt{\frac{T_c}{T - T_c}}, \quad (4)$$

in the zero-field limit, where Φ_0 is the flux quantum, and ξ_{ab} and ξ_c are the coherence lengths parallel and perpendicular to the ab plane at zero temperature, respectively.¹³²⁾ In the multi-band case, the behavior of χ_{AL} is determined by the shortest coherence length of the main band, which governs the orbital upper critical field.

The low-field diamagnetic response in FeSe, which is measured by the magnetic torque $\tau = \mu_0 V M \times \mathbf{H}$ (where V is the sample volume), has been reported to exhibit highly unusual nature of the superconducting fluctuations.¹³⁴⁾ From the torque measurements, the difference between the c axis and ab plane susceptibilities, $\Delta\chi = \chi_c - \chi_{ab}$, can be determined. It has been reported that $\Delta\chi(T)$ is strongly enhanced with decreasing T and exhibits divergent behavior near T_c , indicating the presence of the superconducting fluctuation-induced diamagnetic contribution.¹³⁴⁾ The Gaussian type fluctuation susceptibility given by Eq. 4 indicates that diamagnetic response of the magnetization is H -linear. In contrast, the observed diamagnetic response of FeSe contains both H -linear and non-linear contributions of the magnetization.¹³⁴⁾ Figure 16 and its inset show the temperature dependence of non-

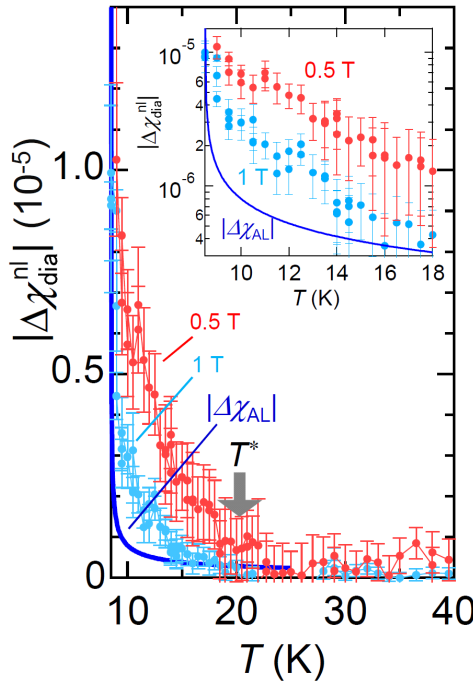


Fig. 16. Temperature dependence of the non-linear diamagnetic response at $\mu_0 H = 0.5$ T (red) and 1 T (blue) obtained by the magnetic torque measurements. Below T^* this diamagnetic response is largely enhanced. Blue line represents $|\Delta\chi_{AL}|$ in the standard Gaussian fluctuations theory calculated from Eq.(4). The inset shows $|\Delta\chi_{dia}^n|$ plotted in a semi-log scale at low temperatures. Adopted from Ref. 134.

linear part $\Delta\chi_{dia}^n$, which is estimated by subtracting the H -linear contribution obtained at the highest field as $\Delta\chi_{dia}^n(H) \approx \Delta\chi(H) - \Delta\chi(7$ T). In Fig. 16 and its inset, the contribution expected from the Gaussian fluctuation theory given by $\Delta\chi_{AL} \approx -\frac{2\pi^2}{3} \frac{k_B T_c}{\Phi_0^2} \left(\frac{\xi_{ab}^2}{\xi_c} - \xi_c \right) \sqrt{\frac{T_c}{T-T_c}}$ is also plotted, where we use $\xi_{ab} = 5.5$ nm and $\xi_c = 1.5$ nm. Near T_c , $\Delta\chi_{dia}^n$ at 0.5 T is nearly 10 times larger than $\Delta\chi_{AL}$.

The above results provide evidence that the amplitude of the diamagnetic fluctuations of FeSe is by far exceeding that expected in the standard Gaussian theory, implying that the superconducting fluctuations in FeSe are distinctly different from those in conventional superconductors. The superconducting fluctuations in FeSe have been further examined by several groups. The NMR relaxation rate divided by the temperature $(T_1 T)^{-1}$, which increases below T_s , starts to be suppressed below T^* . The NMR results report the presence of the superconducting fluctuations that deviate from the standard Gaussian theory. On the other hand, the magnetization measurements using a superconducting quantum interference device (SQUID) did not observe such a large superconducting fluctuation signal.¹³⁵⁾ Moreover, the magnetic torque measurements by using an optical detection technique report a considerably smaller fluctuation signal originating from the vortex liquid.¹³⁶⁾ The discrepancy between these measurements may be due to the sample quality. In fact, the crystals in which a giant superconducting fluctuation is observed exhibit very large magnetoresistance and distinct quantum oscillations at high magnetic fields.

Although giant superconducting fluctuations are observed in the diamagnetic response in FeSe, the jump of the heat ca-

pacity at T_c is still an ordinary mean-field BCS-like as shown in Fig. 8(c). However, recent detailed analysis of the heat capacity near T_c suggests the presence of superconducting fluctuations that substantially exceed Gaussian fluctuations.¹³⁹⁾ The heat capacity measurement report significant fluctuation effects not only in zero and but also in the vortex state with magnetic field applied both parallel and perpendicular to the *ab* plane.

Thermal fluctuations have a dramatic effect on the vortex system in type-II superconductors.¹⁴⁰⁾ One of the most prominent effect is the vortex lattice melting. The vortex lattice melts when the thermal displacement of the vortices is an appreciable fraction of the distance between vortices. In quasi-2D high- T_c cuprates, the magnetic field at which the melting transition occurs is much lower than the mean upper critical field H_{c2} . The strength of the thermal fluctuations is quantified by the dimensionless Ginzburg number, $G_i = [\epsilon k_B T_c / H_c^2(0) \xi_{ab}^3]^2/2$, which measures the relative size of the thermal energy $k_B T_c$ and the condensation energy within the coherence volume. Here $\epsilon \equiv \lambda_c / \lambda_{ab}$ (λ_c is the penetration depth for screening current perpendicular to the *ab* plane) is the anisotropy ratio and $H_c = \Phi_0 / 2\sqrt{2}\lambda_{ab}\xi_{ab}$ is the thermodynamic critical field. The large G_i leads to the reduction of the vortex lattice melting temperature T_{melt} . G_i is roughly proportional to $(\Delta/\varepsilon_F)^4$. In conventional low- T_c superconductors, G_i ranges from 10^{-11} to 10^{-7} , while in FeSe with large Δ/ε_F , G_i is estimated to be as large as 10^{-2} , which is comparable or even larger than that of YBa₂Cu₃O₇. We therefore expect a sizable separation of the melting transition below $T_c(H)$ over a large portion of the phase diagram, as it is the case in the high- T_c cuprates. Very recently, the vortex lattice melting transition has been reported by heat capacity measurements.¹⁴¹⁾ It has been reported that the melting line merges with H_{c2} at a finite temperature, which is consistent with the theory of the vortex lattice melting in strongly Pauli-limited superconductors.¹⁴²⁾

4.3.2 Pseudogap

An important question related to the preformed pairs is the formation of the pseudogap, which is a characteristic signature of BCS-BEC crossover other than the giant superconducting fluctuations. The pseudogap formation in FeSe is a nontrivial issue because FeSe is a compensated semimetal with hole and electron pockets, which may give rise to more complicated phenomena than in the single-band case.¹⁴³⁾ Below T^* , the NMR $(T_1 T)^{-1}$ is suppressed and exhibits a broad maximum at $T_p(H)$, which bears a resemblance to the pseudogap behavior in optimally doped cuprate superconductors.¹³⁸⁾ It has been reported that T^* and $T_p(H)$ decrease in the same manner as $T_c(H)$ with increasing H . This suggests that the pseudogap behavior in FeSe is ascribed to superconducting fluctuations, which presumably originate from the theoretically predicted preformed pairs.¹³⁸⁾

Spectroscopic signature for the pseudogap formation above T_c was first reported by the STM/STS measurements.¹⁴⁴⁾ However, as shown in Fig. 17(a), the subsequent STM/STS measurements reported the absence of the pseudogap.¹⁰⁴⁾ The absence of the spectroscopic pseudogap despite a large Δ/ε_F has been discussed in terms of the multi-band character and its compensated semimetal nature of FeSe. In the BCS-BEC crossover superconductivity of a single band system, the

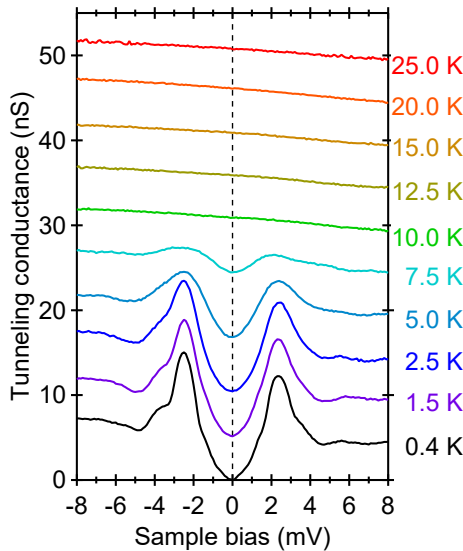


Fig. 17. Tunneling spectra taken at different temperatures. Each curve is shifted by 5 nS for clarity. Adopted from Ref. 104.

chemical potential is shifted outside of the band edge. However, if there are hole and electron bands, which nearly compensate each other and have strong interband interactions, the chemical potential should be pinned at the original energy position. In the case of perfectly symmetrical electron and hole bands, chemical potential should always be pinned at zero energy because $\mu_e + \mu_h = 0$ both in the normal and superconducting states, where μ_e and μ_h are chemical potentials of the electron and hole bands, respectively. It has been pointed out that in such a case, the splitting between T^* and T_c is largely reduced,¹⁴³⁾ leading to the suppression of the pseudogap formation even in the BCS-BEC crossover regime.

In a real material, however, there is a certain asymmetry between the electron and hole bands, which should cause a shift of the chemical potential as a function of temperature. The multiband character brings about another effect that suppresses the pseudogap formation.¹⁰⁴⁾ If there are electron and hole pockets, there should appear two pairing channels associated with the interband and intraband interactions. In the case of FeSe, superconductivity occurs in the nematic phase and the superconducting gap possesses strong anisotropy as discussed in §3. A possible scenario is that the anisotropy is caused by the mixture of *s*-wave and *d*-wave symmetries and the former and the latter are caused by interband and intraband interactions, respectively. Theoretical calculations based on such a model have been performed to estimate the pair-formation and the superconducting-transition temperatures.¹⁰⁴⁾ It has been shown that if the interband pairing is stronger than the intraband pairing, which may be the case for FeSe, the pair-formation and the superconducting-transition temperatures do not split despite of large Δ/ε_F .¹⁰⁴⁾ The BCS-BEC crossover in the multiband system may be difficult to realize in ultracold atomic systems. Therefore, FeSe is unique and can open a new research field for the BCS-BEC crossover.

4.3.3 Evolution of BCS-BEC crossover in $\text{FeSe}_{1-x}\text{S}_x$

Very recently, the evolution of the BCS-BEC crossover properties with sulfur substitution has been investigated in $\text{FeSe}_{1-x}\text{S}_x$. ARPES measurements reported that Δ/ε_F de-

creases with x , but it still remains large.¹¹³⁾ Therefore, it is expected that the crossover nature is less pronounced in $\text{FeSe}_{1-x}\text{S}_x$. Contrary to this expectation, it has been found that the crossover nature becomes more significant in $\text{FeSe}_{1-x}\text{S}_x$.^{113,139)} The ARPES experiments report that flat dispersion of the Bogoliubov quasiparticles is more pronounced with x in the nematic regime. Surprisingly, on entering the tetragonal regime beyond the nematic QCP, flat dispersion changes to BEC-like one, which shows the gap minimum at $\mathbf{k} = 0$.¹¹³⁾ The heat capacity measurements reveal the highly unusual BEC-like transition with strong fluctuations in tetragonal $\text{FeSe}_{1-x}\text{S}_x$,¹³⁹⁾ which appears to be consistent with the ARPES measurements.

However, the formation of the spectroscopic pseudogap in the tetragonal $\text{FeSe}_{1-x}\text{S}_x$ is controversial. Although ARPES measurements report the distinct pseudogap-like reduction of the DOS in the hole pocket above T_c ,¹¹³⁾ no discernible reduction of the DOS is observed in STS measurements.¹³⁹⁾ The evolutions of the BCS-BEC crossover behavior in $\text{FeSe}_{1-x}\text{S}_x$ again suggest that a multiband system may possess a unique feature that is absent in a single band system. Thus $\text{FeSe}_{1-x}\text{S}_x$ offers a unique playground to search for as-yet-unknown novel phenomena in strongly interacting fermions, which deserves future attention.

5. Exotic Superconducting State Induced by Magnetic Field

5.1 Field-induced superconducting phase

The emergence of a novel superconducting phase at high magnetic fields, whose pairing state is distinctly different from that of the low-field phase, has been a longstanding issue in the study of superconductivity. One intriguing issue related with this field-induced phase concerns whether the spin imbalance or spin polarization will lead to a strong modification of the properties of the electron systems. This problem has been of considerable interest not only for superconductors in solid state physics, but also in the studies of neutral Fermion superfluid in the field of ultracold atomic systems and for the color superconductivity in high-energy physics. Among several possible exotic states associated with the spin imbalance, a spatially nonuniform superconducting state caused by the paramagnetism of conduction electrons has been one of the most intensively studied topics in the past half-century after the pioneering work by Fulde and Ferrell (FF) as well as Larkin and Ovchinnikov (LO).^{145–149)} In the FFLO state, an inhomogeneous superconducting state with modulated superconducting order parameter is formed.

It has been reported that in FeSe, a new superconducting phase appears at the low-temperature/high-field corner in the superconducting state of the H - T phase diagram for both $\mathbf{H} \parallel ab$ plane^{150,151)} and $\mathbf{H} \parallel c$ axis.⁹¹⁾ It has been discussed that the field-induced phase for $\mathbf{H} \parallel ab$ is at least consistent with the FFLO phase. However, even if the FFLO state is realized in FeSe, its physical properties are expected to be very different from those of the originally predicted FFLO state in several aspects, such as the extremely highly spin polarized state,⁹¹⁾ coexistence of the FFLO and the Abrikosov vortex states,¹⁵¹⁾ strongly orbital-dependent pairing interaction,¹⁰⁵⁾ nontrivial Zeeman effect due to spin-orbit coupling,¹⁵¹⁾ and multiband electronic structure. In particular, the magnetic field-induced superconducting phase in

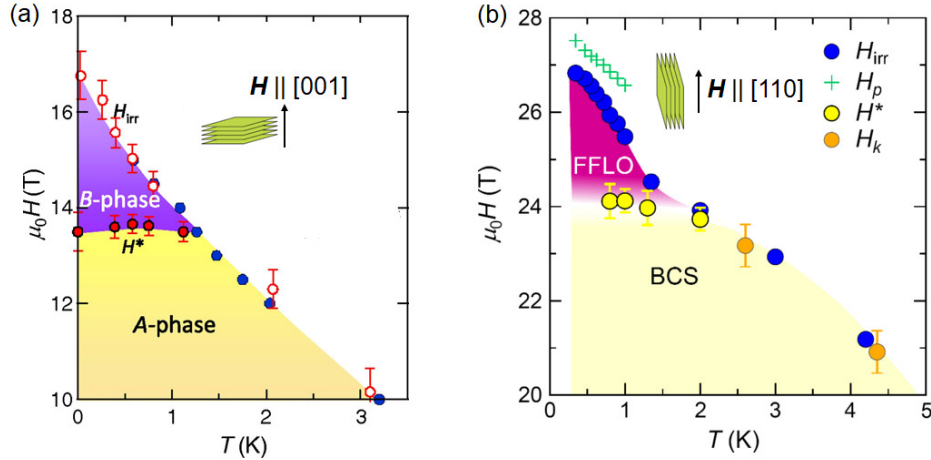


Fig. 18. (a) High-field phase diagram of FeSe for $\mathbf{H} \parallel c$. Solid blue and open red circles represent the irreversible field H_{irr} determined by the resistivity and the magnetic torque, respectively. The mean-field upper critical field is above H_{irr} . Solid red circles represent H^* determined by the cusp of the field dependence of the thermal conductivity. High-field superconducting B-phase separated from the low-field A phase, which is the BCS pairing ($\mathbf{k} \uparrow, -\mathbf{k} \downarrow$) phase, has been proposed. Adopted from Ref. 91. (b) Phase diagram for $\mathbf{H} \parallel ab$ plane. Blue circles and green crosses show H_{irr} and H_p determined by resistivity measurements. Orange and yellow circles show H_k and H^* determined by thermal-conductivity measurements, respectively. Above the first-order phase transition field H^* a distinct field-induced superconducting phase emerges at low temperatures. High-field phase has been attributed to the FFLO pairing ($\mathbf{k} \uparrow, -\mathbf{k} + \mathbf{q} \downarrow$) state. Adopted from Ref. 151.

FeSe provides insights into previously poorly understood aspects of the highly spin-polarized Fermi liquid in the BCS-BEC crossover regime.

5.2 FeSe in strong magnetic field

The presence of the high-field superconducting phase separated from the low-field one has been reported by several measurements, including resistivity, magnetic torque, heat capacity and thermal transport measurements. The phase diagram in magnetic field applied parallel to the c axis ($\mathbf{H} \parallel c$) is shown in Fig. 18(a).⁹¹⁾ At a field H^* , the thermal conductivity exhibits a cusp-like feature. As the Cooper pair condensate does not contribute to heat transport, the thermal conductivity can probe quasiparticle excitations out of the superconducting condensate.¹⁵²⁾ Moreover, the thermal conductivity has no fluctuation corrections, the cusp of κ/T usually corresponds to a mean-field phase transition. The presence of H^* has also been reported by a distinct kink anomaly of the thermal Hall conductivity κ_{xy} . The analysis of the thermal Hall angle κ_{xy}/κ indicates a change of the quasiparticle scattering rate at H^* .¹⁵³⁾ Very recently, the anomaly at H^* is also confirmed by heat capacity measurements.

The irreversibility field H_{irr} caused by the vortex pinning is determined by the magnetic torque, which measures the bulk properties, and by the resistivity. The irreversibility line at low temperatures extends to high fields well above H^* , demonstrating that H^* is located inside the superconducting state. These results suggest the presence of a field-induced superconducting phase (B-phase in Fig. 18(a)). However, the presence of B-phase is controversial between different groups.^{91, 141, 153)}

The H - T phase diagram of FeSe for $\mathbf{H} \parallel ab$ has also been studied recently by several groups via the measurements of in-plane electrical resistivity, thermal conductivity,¹⁵¹⁾ magnetocaloric effect¹⁵⁰⁾ and heat capacity¹⁴¹⁾ up to 35 T. All measurements appear to consistently show the presence of field-induced superconducting phase in this geometry. Figure 18(b)

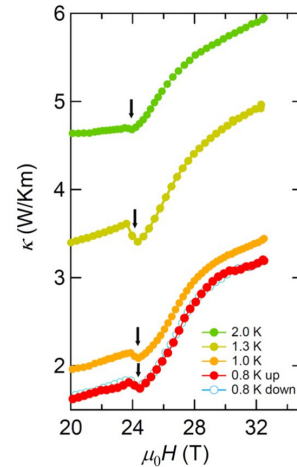


Fig. 19. Magnetic field dependence of thermal conductivity in the high field regime at low temperatures in FeSe for $\mathbf{H} \parallel ab$. A discontinuous downward jump appears at $\mu_0 H^* \approx 24$ T inside the superconducting state as indicated by black arrows. Adopted from Ref. 151.

displays the H - T phase diagram. The anomaly in the superconducting state has been first reported by the magnetocaloric effect.¹⁵⁰⁾ The most remarkable anomaly has been reported by the thermal conductivity measurements on a twinned crystal in \mathbf{H} applied along the diagonal direction in the ab plane ($\mathbf{H} \parallel [110]_0$, in orthorhombic notation). As displayed in Fig. 19, $\kappa(H)$ exhibits a discontinuous downward jump at $\mu_0 H^* \approx 24$ T inside the superconducting state. At H^* , $\kappa(H)$ shows a large change of the field slope and increases steeply with H above H^* . It should be stressed that the jump of $\kappa(H)$, which is caused by a jump in entropy, is a strong indication of a first-order phase transition, as reported for CeCoIn₅¹⁵⁴⁾ and URu₂Si₂.¹⁵⁵⁾

In the H - T phase diagram, the irreversibility field, H_{irr} , determined by the onset field of non-zero resistivity is also shown. Below ~ 2 K, H_{irr} exhibits an anomalous upturn. It

should be stressed that H^* is deep inside the superconducting state at low temperatures, as evidenced by the fact that H^* is well below H_{irr} . No discernible anomaly of $\kappa(H)$ is observed above about 2 K, indicating that the first-order transition occurs only within the superconducting state. It has been reported that the resistive transition under magnetic fields exhibits a significant broadening at high temperatures. This is attributed to a strongly fluctuating superconducting order parameter, which gives rise to the drift motion of vortices in the liquid state. On the other hand, below ~ 1 K, the resistive transition becomes very sharp.¹⁵¹⁾ Thus, there is a distinct high-field superconducting phase, which is well separated by a first-order phase transition from the low-field phase, also for $\mathbf{H} \parallel ab$. The quantum oscillation measurements exclude the possibility that the high-field superconducting phases observed for both $\mathbf{H} \parallel c$ and $\mathbf{H} \parallel ab$ are AFM ordered phases.

5.3 Fulde-Ferrell Larkin-Ovchinnikov (FFLO) state

Superconductivity is destroyed by external magnetic field through the orbital and Pauli pair breaking effects. The former effect is associated with the Lorentz force acting on electrons, which results in the formation of vortices. This orbital pair-breaking field is given as $H_{\text{orb}} = \Phi_0/2\pi\xi^2$. The latter effect is associated with the spin paramagnetic effect that tries to align the spin of the original singlet Cooper pairs through the Zeeman effect. This Pauli pair-breaking limit takes place when the paramagnetic energy in the normal state $E_P = \frac{1}{2}\chi_n H^2$, where $\chi_n = g\mu_B^2 N(\epsilon_F)$ is the normal-state spin susceptibility, where g is the g -factor and μ_B the Bohr magneton, coincides with the superconducting condensation energy $E_s = \frac{1}{2}N(\epsilon_F)\Delta^2$, which yields $H_P = \Delta/\sqrt{g\mu_B}$. The ratio of H_{orb} and H_P , which is called Maki parameter, is given by

$$\alpha_M \equiv \sqrt{2} \frac{H_{\text{orb}}}{H_P} \approx \frac{m^*}{m_0} \frac{\Delta}{\epsilon_F}, \quad (5)$$

where m^* is the effective mass of the conduction electron and m_0 is the free electron mass. The Maki parameter is usually much less than unity, indicating that the influence of the paramagnetic effect is negligibly small in most superconductors. However, in quasi-2D layered superconductors (for parallel fields) and heavy fermion superconductors, α_M is largely enhanced owing to large m^*/m_0 values, and thus the superconductivity may be limited by Pauli paramagnetic effect. It should be stressed that in superconductors in the BCS-BEC crossover regime, large Δ/ϵ_F leads to the enhancement of α_M value.

FFLO proposed that when the superconductivity is limited by the Pauli paramagnetic effect, the upper critical field can be enhanced by forming an exotic pairing state.^{145,146)} In contrast with the $(\mathbf{k} \uparrow, -\mathbf{k} \downarrow)$ pairing in the traditional BCS state, as shown in Fig. 20(a), the Cooper pair formation in the FFLO state occurs between Zeeman splitted parts of the Fermi surface leading to a new type of $(\mathbf{k} \uparrow, -\mathbf{k} + \mathbf{q} \downarrow)$ pairing with $|\mathbf{q}| \sim g\mu_B H/\hbar v_F$ (v_F is the Fermi velocity), as shown in Fig. 20(b); the Cooper pairs have finite center-of-mass momenta. Because of the finite $q \equiv |\mathbf{q}|$, the superconducting order parameter $\Delta(\mathbf{r}) \propto \langle \psi_{\downarrow}^{\dagger}(\mathbf{r}) \psi_{\uparrow}^{\dagger}(\mathbf{r}) \rangle$ has an oscillating component $\exp(i\mathbf{q} \cdot \mathbf{r})$. The FF superconducting state has a spontaneous modulation in the phase of the order parameter,¹⁴⁵⁾ while the LO state has a spatial modulation of Cooper pair density.¹⁴⁶⁾ It is generally found that the LO states are fa-

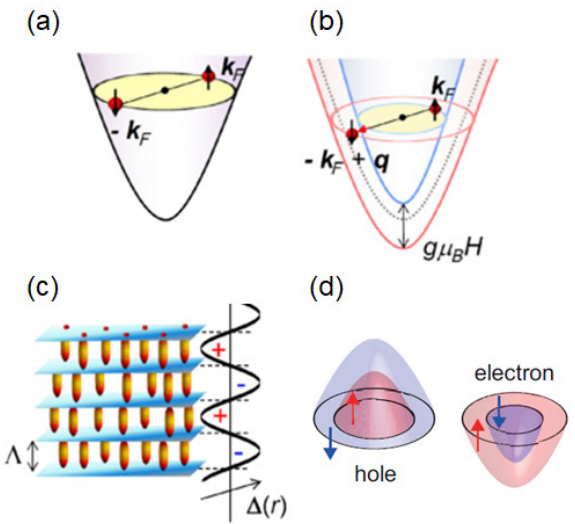


Fig. 20. (a) Schematic illustration of Cooper pairing ($\mathbf{k} \uparrow, -\mathbf{k} \downarrow$) in the BCS state. (b) Pairing state with $(\mathbf{k} \uparrow, -\mathbf{k} + \mathbf{q} \downarrow)$ in the FFLO state. (c) Schematic illustration of the superconducting order parameter Δ in real space and segmentation of the magnetic flux lines by planar nodes. (d) Schematic electronic structures of hole and electron pockets at fields around H^* in FeSe. Both Fermi surfaces are highly spin imbalanced. Adopted from Ref. 151.

vored over the FF states, but henceforth both states are simply refer to as FFLO state. In the FFLO state, spatial symmetry breaking originating from the appearance of the \mathbf{q} -vector appears, in addition to gauge symmetry breaking. A fascinating aspect of the FFLO state is that it exhibits inhomogeneous superconducting phases with a spatially oscillating order parameter. In its simplest form, order parameter is modulated as $\Delta(\mathbf{r}) \propto \sin(\mathbf{q} \cdot \mathbf{r})$, and periodic planar nodes appear perpendicular to the magnetic field, leading to a segmentation of the vortices into pieces of length $\Lambda = \pi/q$, as illustrated in Fig. 20(c).

Despite considerable research efforts in the search for the FFLO states in the past half century, the FFLO state still constitutes a challenge for the researchers. Very stringent conditions are required for the realization of the FFLO state. In real bulk type-II superconductors, the orbital effect is invariably present, which is detrimental to the formation of the FFLO state. The FFLO state can exist at finite temperatures if α_M is larger than 1.8, but the FFLO region shrinks considerably from that in the absence of the orbital effect. Moreover, the FFLO state is highly sensitive to disorder. Despite tremendous studies of the FFLO state, its firm experimental confirmation is still lacking. Some signatures of the FFLO state have been reported in only a few candidate materials, including heavy fermion¹⁴⁷⁾ and quasi-2D organic superconductors.^{148,149)} Among them, organic κ -(ET)₂Cu(NCS)₂ and heavy fermion CeCoIn₅ have been studied most extensively. In both systems, a thermodynamic phase transition occurs below upper critical fields and a high-field superconducting phase emerges at low temperatures.^{156–159)} In the former, each superconducting layer is very weakly coupled via the Josephson effect. A possible FFLO state is reported in a magnetic field applied parallel to the layers, where the magnetic flux is concentrated in the regions between the layers forming coreless Josephson vortices. However, the position of the first order transition in H - T phase diagram has been controver-

sial, depending on the measurement method. Moreover, it has been pointed out that vortex phase transitions have given rise to considerable ambiguity in the interpretation of the experimental data. The presence of the FFLO phase in CeCoIn₅ remains a controversial issue. In fact, the H - T phase diagram of CeCoIn₅ is very different from that expected in the original FFLO state. Moreover, the magnetic order occurs simultaneously at the putative FFLO transition,¹⁶⁰⁾ indicating that this phase is not a simple FFLO phase.^{161–163)} Possible FFLO states have also been discussed recently in other systems, including heavy fermion CeCu₂Si₂¹⁶⁴⁾ and iron-pnictide KFe₂As₂.¹⁶⁵⁾

FeSe may satisfy some of the prerequisites for the realization of the FFLO state. In FeSe in the vicinity of the BCS-BEC crossover regime, an estimate gives $\Delta/\varepsilon_F \sim 0.1\text{--}0.3$ for the hole band and even larger Δ/ε_F for the electron band.^{88,91)} By using $m^* \approx 7m_0$ ($4m_0$) for hole (electron) pocket determined by SdH oscillation experiments,⁴⁴⁾ α_M is found to be as large as ~ 5 (~ 2.5) for the electron (hole) pocket. This fulfills a requirement for the formation of the FFLO state. Moreover, the analyses of magnetoresistance and quantum oscillations show that high-quality single crystals of FeSe, obtained through flux/vapor-transport growth techniques,¹⁶⁶⁾ are in the ultra-clean limit with extraordinary long mean free path ℓ .

On the other hand, there are several unique aspects in FeSe, which have not been taken into account in the original idea of the FFLO state. They arise from the extremely shallow pockets and multi-band character.

- Extremely large spin imbalance. The BCS-BEC crossover nature in FeSe gives rise to the large spin imbalance near the upper critical field, which will be discussed in the next subsection.
- Strong spin-orbit coupling, $\lambda_{so} \sim \varepsilon_F$, which yields largely orbital-dependent Zeeman effect. It has been suggested that this seriously modifies the Pauli limiting field through the g -factor.
- Orbital-dependent pairing interaction, which is expected to affect seriously the q -vector. The FFLO pairing may also be orbital dependent.

It has been discussed that the high-field phase for $\mathbf{H} \parallel ab$ can be associated with an FFLO phase for the following reasons. First, in the H - T phase diagram shown in Fig. 18(b), the steep enhancement of H_{c2}^{ab} at low temperatures and the first-order phase transition at a largely T -independent H^* are consistent with the original prediction of the FFLO state. Second, planar nodes perpendicular to \mathbf{H} are expected as the most optimal solution for the lowest Landau level. In the present geometry, where the thermal current density $j_T \parallel \mathbf{H}$, quasi-particles that conduct heat are expected to be scattered by the periodic planar nodes upon entering the FFLO phase. This leads to a reduction of $\kappa(H)$ just above H^* , which is consistent with the present results. Third, as the c -axis coherence length ($\xi_c \approx 1.5$ nm) well exceeds the interlayer distance (0.55 nm),^{4,44)} one-dimensional (1D) tube-like Abrikosov vortices are formed even in a parallel field. In this case, the planar node formation leads to a segmentation of the vortices into pieces of length Λ . The pieces are largely decoupled and, hence, better able than conventional vortices to position themselves at pinning centers, leading to an enhancement of the

pinning forces of the flux lines in the FFLO phase. This is consistent with the observed sharp resistive transition above H^* . Fourth, as will be discussed in the next subsection, the electron pocket is extremely spin polarized near the upper critical fields. Therefore, it is questionable that superconducting pairing is induced in the electron pocket in such a strongly spin-imbalanced state. It has been shown that the FFLO instability is sensitive to the nesting properties of the Fermi surface. When the Fermi surfaces have flat parts, the FFLO state is more stabilized through nesting. As the portion of the hole pocket derived from the d_{yz} orbital forms a Fermi-surface sheet that is more flattened than the other portion of the Fermi surface, this 1D-like Fermi sheet is likely to be responsible for the FFLO state.

In contrast to $\mathbf{H} \parallel ab$, the high field phase for $\mathbf{H} \parallel c$ remains elusive and its identification is a challenging issue. It cannot be simply explained by the FFLO state, although the H - T phase diagram has some common features with that for $\mathbf{H} \parallel ab$. The q -vector, which is always in the ab plane, does not stabilize FFLO state for $\mathbf{H} \parallel c$. Therefore, an FFLO state may be difficult to be formed due to the lack of q -vector for \mathbf{H} applied perpendicular to the quasi-2D Fermi surface of FeSe. According to the calculation of the effective g -factor obtained by the orbitally projected model,¹⁶⁷⁾ the formation of FFLO state is more favored for $\mathbf{H} \parallel ab$ than for $\mathbf{H} \parallel c$.¹⁵¹⁾ Recently a possible FFLO state has been proposed even for $\mathbf{H} \parallel c$.¹⁶⁶⁾

5.4 Highly spin polarized field-induced state in the BCS-BEC crossover regime

The field-induced superconducting phase provides insights into previously poorly understood aspects of the highly spin-polarized Fermi liquid in the BCS-BEC crossover regime. In the standard BCS theory of spin singlet pairing, the pairing occurs between the fermions with opposite spins. The question of what happens if a large fraction of the spin-up fermions cannot find spin-down partners has been widely discussed by researchers from different aspects. In conventional superconductors, however, a large unequal population of spin-up and down electrons is very difficult to be realized, essentially because superconductivity is usually destroyed by the orbital pair-breaking effects. Even when the superconductivity is destroyed by Pauli paramagnetic effect, such a spin imbalance is usually negligibly small.

In paramagnetic metals, the spin imbalance is caused by the Zeeman splitting in magnetic field, as shown in Fig. 20(d). The magnitude of the spin imbalance $P_{\text{spin}} = (N_\uparrow - N_\downarrow)/(N_\uparrow + N_\downarrow)$, where N_\uparrow and N_\downarrow are the numbers of up and down spins, respectively, is roughly estimated as $P_{\text{spin}} \approx \mu_B H/\varepsilon_F$. Therefore, P_{spin} is estimated to be $P_{\text{spin}} \approx \Delta/\varepsilon_F$ at H_P in Pauli-limited superconductors. In orbital-limited superconductors, where $H_{\text{orb}} < H_P$, P_{spin} at H_{orb} is smaller than that expected in Pauli-limited superconductor. Therefore, in almost all superconductors, P_{spin} is usually negligibly small, $P_{\text{spin}} < 10^{-2}$, near the upper critical field, i.e. the effect of the spin imbalance is not taken into account in the original FFLO proposal.

One intriguing issue concerns whether the large spin imbalance will lead to a strong modification of the properties of the correlated Fermi systems. Although highly spin-imbalanced Fermi systems have been realized in ultracold atomic gases, the nature of the spin imbalanced superfluid remains unexploited experimentally due to the difficulty in cooling the sys-

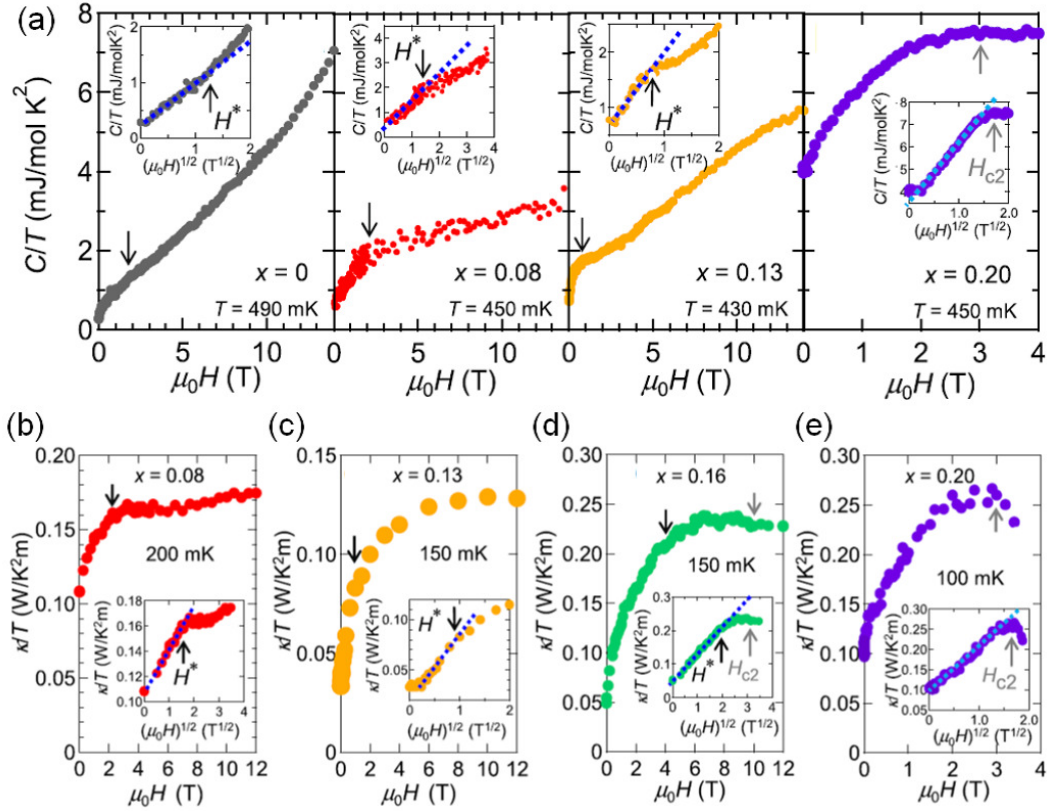


Fig. 21. (a) Field dependence of specific heat at low temperatures below ~ 0.5 K in $\text{FeSe}_{1-x}\text{S}_x$ covering orthorhombic ($x = 0, 0.08, 0.13$) and tetragonal ($x = 0.20$) phases. (b-e) Field dependence of thermal conductivity at low temperatures below ~ 0.2 K for orthorhombic $x = 0.08$ (b), 0.13 (c), 0.16 (d), and tetragonal 0.20 (e). The insets are the same data plotted against $H^{1/2}$. The dashed lines are the fits to \sqrt{H} dependence. Adopted from Ref. 89.

tems to sufficiently low temperatures. In FeSe in the BCS-BEC crossover regime, the Zeeman effect is particularly effective in shrinking the Fermi volume associated with the spin minority, giving rise to a highly spin-imbalanced phase where $\varepsilon_F \sim \Delta \sim \mu_B H_{c2}$ near the upper critical fields. For $\mathbf{H} \parallel ab$, an estimate yields $P_{\text{spin}} \sim 0.5$ and 0.2 for electron and hole pockets, respectively, assuming $g = 2$.¹⁵¹⁾ This indicates that electron pockets are extremely highly polarized. Therefore in the high-field phase of FeSe, a large fraction of the spin-up fermions cannot find spin-down partners.

The presence of a possible FFLO phase in FeSe should stimulate considerable further work in understanding and exploiting strongly interacting Fermi liquids near the BCS-BEC crossover regime, which remains largely unexplored and might bridge the areas of condensed-matter and ultracold-atom systems.

6. Superconductivity near the Nematic Critical Point

6.1 Abrupt change of superconducting gap

As discussed in §2.3, the electronic nematic phase in FeSe can be suppressed by isovalent S substitution for Se site. Near the nematic QCP ($x_c \approx 0.17$), the nematic fluctuations are strongly enhanced,³⁶⁾ and the transport properties show non-Fermi liquid properties.^{90,168)} The impact of such nematic quantum criticality on superconductivity is an important subject in the field of condensed matter physics.¹⁶⁹⁾ Inside the nematic phase ($x < x_c$), the superconducting transition temperature T_c shows a broad peak at $x \sim 0.08$ (see Fig. 7). At $x = x_c$, T_c jumps from ~ 8 K inside the nematic phase to ~ 4 K out-

side the nematic phase.^{89,139)} As can be seen in Fig. 21, the upper critical field for $H \parallel c$ is also strongly suppressed from ~ 10 T ($x = 0.16 < x_c$) to ~ 3 T ($x = 0.20 > x_c$).⁸⁹⁾ These significant changes of the superconducting properties at the nematic critical concentration implies that the nematicity, or rotational symmetry breaking, affects strongly on superconductivity.

The superconducting gap structure is changed abruptly at the nematic QCP, which is evidenced by the field dependence studies of specific heat C and thermal conductivity κ .⁸⁹⁾ Inside the nematic phase, the field dependence of both C/T and κ/T shows the \sqrt{H} behavior at low fields as expected in the nodal superconductors, while it deviates from \sqrt{H} at fields much lower than the upper critical field H_{c2} , as shown in Figs. 21(a)-(d). This deviation can be explained by the multigap effect, and the deviation field H^* has been attributed to the virtual upper critical field of the smaller gap. In contrast, in the tetragonal samples outside the nematic phase, such a multigap behavior is not observed, and as shown in Figs. 21(a) and (e), the field dependence of C/T and κ/T can be fitted to \sqrt{H} dependence in the entire field range up to H_{c2} . Near the nematic QCP, charge fluctuations of d_{xz} and d_{yz} orbitals are enhanced equally in the tetragonal side, while they develop differently in the nematic phase. From these results, it has been suggested that the orbital-dependent nature of the nematic fluctuations has a strong impact on the superconducting gap structure and hence on the pairing interaction.⁸⁹⁾

This drastic change of the superconducting gap has been corroborated by the systematic studies of scanning tunneling

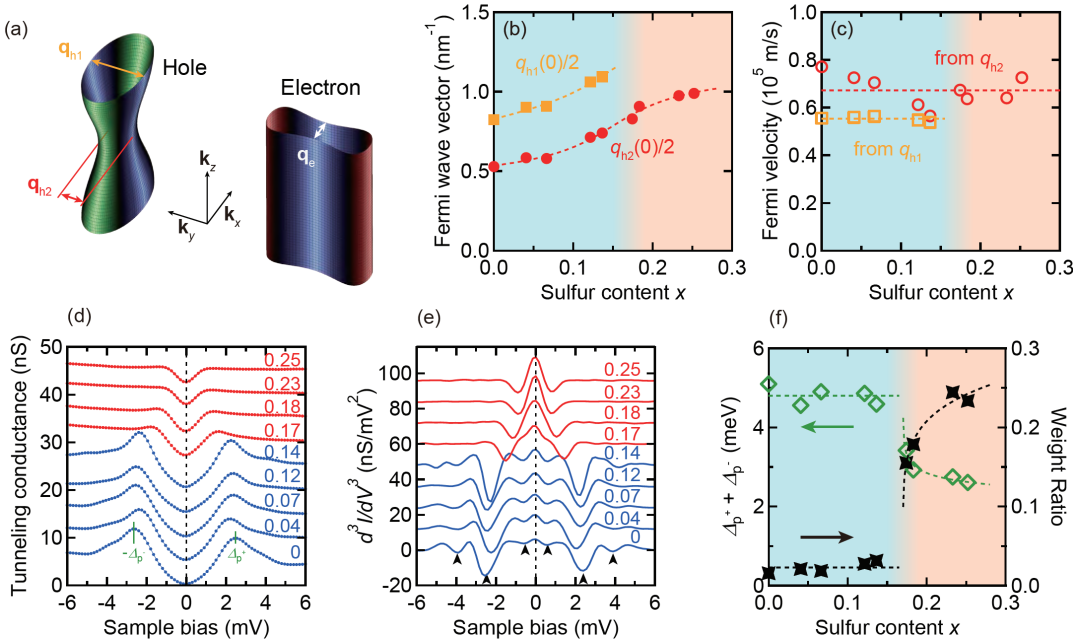


Fig. 22. Evolutions of electronic structure and low-energy excitations with S-substitution determined by QPI and STS measurements in $\text{FeSe}_{1-x}\text{S}_x$. (a) Schematics of the 3D constant energy surface of hole and electron bands, and definitions of characteristic scattering wave vectors q_{h1} and q_{h2} . (b) Evolutions of the scattering wave vectors as functions of sulfur content x . Lines are the guides to the eyes. (c) Evolution of the Fermi velocity with x . (d) Averaged tunneling conductance spectra of $\text{FeSe}_{1-x}\text{S}_x$ for $0 \leq x \leq 0.25$. Each curve is shifted vertically for clarity. Blue (red) curves are for the orthorhombic (tetragonal) phase. (e) Energy second derivative of averaged tunneling spectra. Each curve is shifted vertically clarity. (f) Evolutions of the apparent gap amplitude (green diamond) and the zero-energy spectral weight normalized by the weights at the gap-edge energies (black stars). Adopted from Ref. 88.

spectroscopy,⁸⁸⁾ which are summarized in Fig. 22. The tunneling conductance remains essentially unchanged with increasing sulfur content x inside the nematic phase, but once the nematicity vanishes at $x > x_c \approx 0.17$ the superconducting-gap spectrum shows a dramatic change (see Figs. 22(d)-(f)). Below x_c , clear quasiparticle peaks are observed at energies $\sim \pm 2.5$ meV and zero-energy conductance is very small. Above x_c , however, quasiparticle peaks are strongly damped with a reduced gap size below ~ 1.5 meV, and at the same time the zero-energy state is much more enhanced than that of the orthorhombic samples. The remarkable difference of the zero-bias conductance is also consistent with the thermodynamic properties, and the specific heat data shows a large residual DOS only for $x > x_c$.^{89,139)} By using the QPI technique, the evolution of normal-state electronic structure with x has been also studied by the same specimens (see Figs. 22(a)-(c)), which revealed that the Fermi surface structure changes smoothly across the nematic QCP. This implies that the abrupt change of the superconducting properties is not linked to the strength of nematicity, but the presence or absence of nematicity results in two distinct pairing states separated by the nematic QCP.⁸⁸⁾

6.2 Possible ultranodal pair state with Bogoliubov Fermi surface

An intriguing theoretical proposal that may account for these anomalous superconducting states in $\text{FeSe}_{1-x}\text{S}_x$ has been recently made by Setty *et al.*^{170,171)} This is based on the recent developed notion on a novel superconducting state, dubbed Bogoliubov Fermi surface.¹⁷²⁾

In unconventional superconductors, the superconducting gap is anisotropic in the momentum space, and often exhibits nodes at certain \mathbf{k} points. Thus there are three possible types

of superconducting gaps; the gap is nodeless, it has point nodes, or it has line nodes. It has been shown theoretically that when the even-parity superconductors break the time reversal symmetry (TRS), there is a possibility to have the fourth type having a surface of nodes in some circumstances.¹⁷²⁾ Such a novel state with Bogoliubov Fermi surface (see Fig. 23(a) as an example), which may also be called as a topological ultranodal pair state, can be realized when the Pfaffian of the Bogoliubov-de Gennes Hamiltonian, which is non-negative for TRS preserved states, becomes negative.

In FeSe , as discussed in §3, the gap structure has line nodes or deep minima, and the pairing is likely to be spin singlet. The theoretical calculations show that when the relative strength of intraband to interband pairing interactions is altered as a function of sulfur substitution, the Pfaffian may change sign to negative, providing that the TRS is broken, which gives rise to exotic superconducting states with Bogoliubov Fermi surfaces as shown in Figs. 23(b)-(e).¹⁷⁰⁾ If this condition is realized in the tetragonal phase of $\text{FeSe}_{1-x}\text{S}_x$, then the presence of Bogoliubov Fermi surface changes dramatically the zero-energy DOS, which is consistent with the experimental observations of the substantially large residual low-energy states in tunneling spectra as well as in specific heat (see Figs. 23(f) and (g)).

To realize such a state, the superconducting state must break TRS, and thus the question is whether the FeSe -based superconductors have TRS breaking states or not. The current experimental situation on TRS breaking is reviewed in the next section.

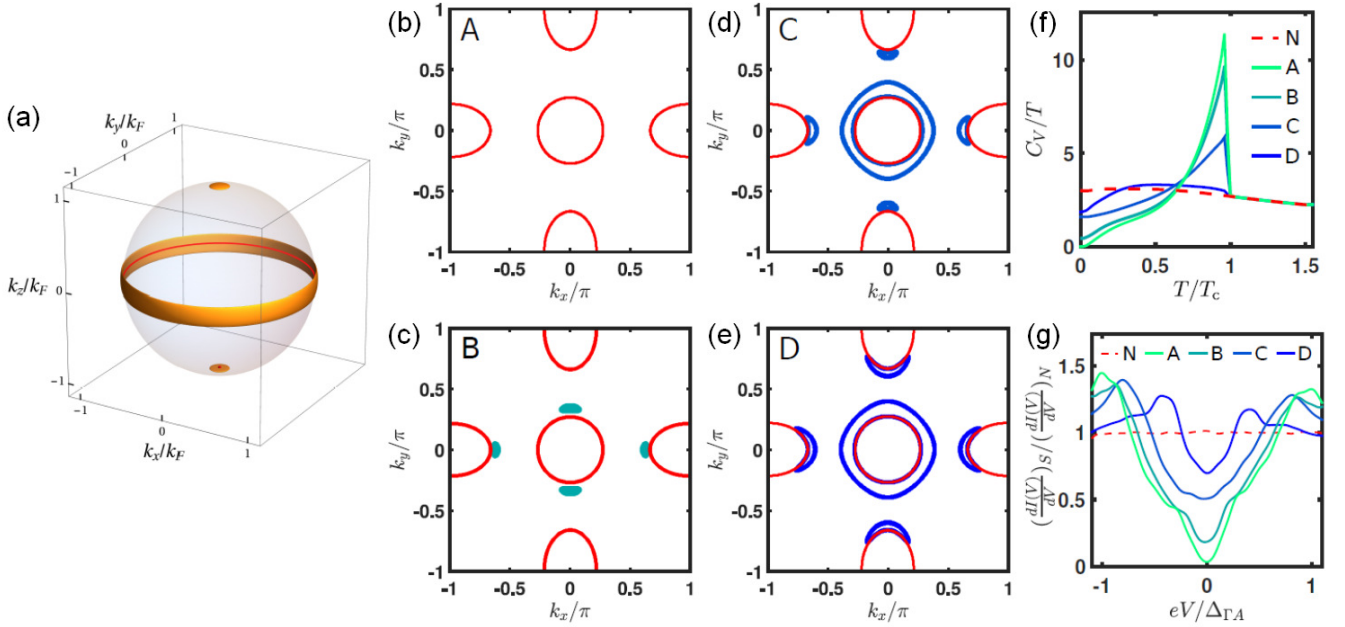


Fig. 23. Exotic superconducting state with Bogoliubov Fermi surfaces. (a) Schematics of the Bogoliubov Fermi surfaces (yellow region), which may appear near the point and line nodes (red points and lines) when time reversal symmetry is broken. Adopted from Ref. 172. (b)-(e) Schematic Fermi surfaces of FeSe-based superconductors in the normal (red) and superconducting states (green and blue patches), for different interband and intraband gap anisotropy parameters. (f) Corresponding temperature dependence of specific heat divided by temperature C/T . (g) Corresponding tunneling conductance spectra at low energies. Panels (b)-(g) are adopted from Ref. 170.

7. Time Reversal Symmetry Breaking

7.1 Effect of nematic twin boundary

Time reversal is simply equivalent to complex conjugation of the wave functions for a spinless system. Thus in spin sin-

glet superconductors, a TRS breaking state can be described by a complex order parameter $\Delta = \Delta_1 + i\Delta_2$, whose time reversal $\Delta^* = \Delta_1 - i\Delta_2$ is not identical to Δ . In a tetragonal D_{4h} system, the s -wave and d -wave even-parity pairing states belong to different irreducible representations, and thus these states in general have different transition temperatures. Usually one of the transition temperatures wins over the other one, but when the pairing interactions that drive these different states are comparable, these two states may mix in a form of $s+id$ state that onsets at a temperature lower than the actual T_c .

In the nematic phase with orthorhombic symmetry, the s -wave and d -wave states no longer belong to different irreducible representations, and they can mix in a real form $s+id$.¹⁷³⁾ This can be easily understood by the fact that the nematicity is characterized by the two-fold symmetry in the plane, and thus the superconducting order parameter should also be two-fold symmetric, as evidence by the observation of the elongated ellipsoidal shape of vortices,^{102–104)} which can be described by the sum of fourfold s -wave and twofold d -wave components.

In the nematic phase, another important aspect is the formation of domains with different nematic directions. Across a boundary of the two domains, namely nematic twin boundary, the crystal structure is rotated by 45 degrees as schematically shown in Fig. 24(a). Thus the twofold d -wave component of the superconducting order parameter must change sign across a twin boundary, i.e. one domain has an $s+d$ state and the other domain has an $s-d$ state. Then the question is how to reverse the sign near the twin boundary. One possibility is to change sign with keeping the order parameter real, and the magnitude of d -wave component shrinks when approaching the boundary and becomes zero at the twin boundary. Another

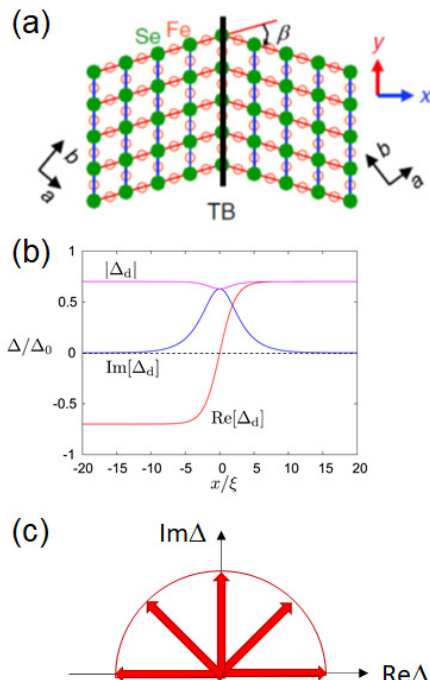


Fig. 24. Possible complex order parameter induced near nematic twin boundaries.^{103, 174)} (a) Schematic view of the crystal structure of FeSe near a twin boundary. Adopted from Ref. 103. (b) Possible position dependence of d -wave component near a twin boundary with finite imaginary part. The real part should change sign across the boundary, while the magnitude of the gap remains finite owing to the induced imaginary part. (c) Schematic trajectory of the gap function as a function of position in the complex plane.

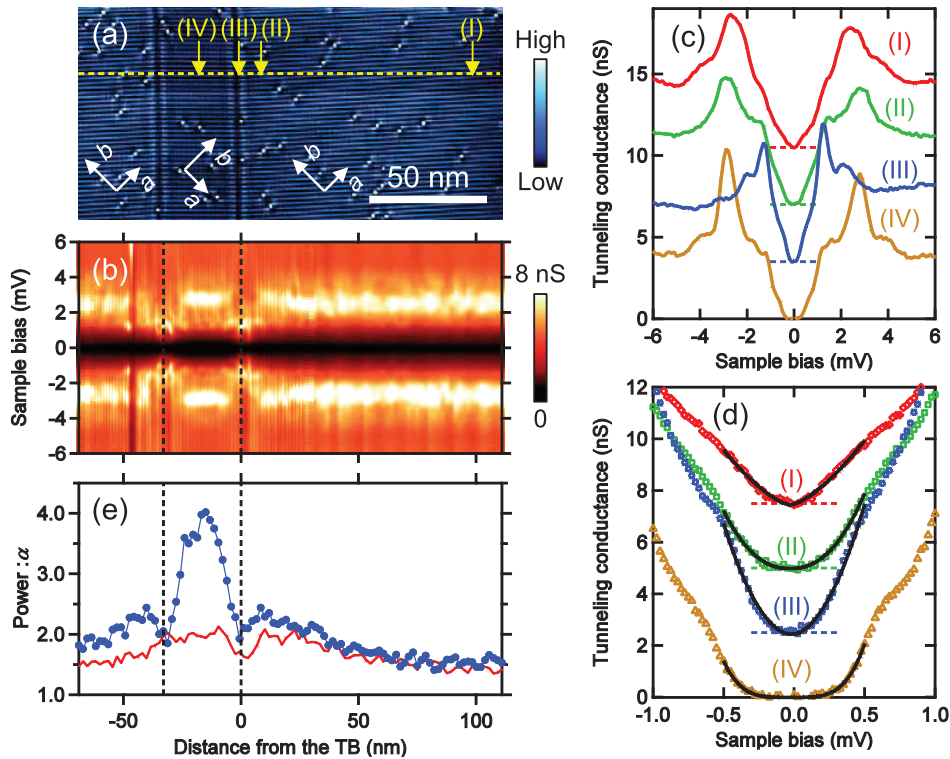


Fig. 25. Evolution of STM conductance spectra across nematic twin boundaries in FeSe. (a) STM topographic image in an area containing two vertical twin boundaries separated by ~ 33 nm. (b) Intensity plot for the position dependence of conductance spectra along the yellow dashed line in (a). (c) Tunneling spectra at 4 positions indicated in (a). Each curve is shifted vertically for clarity. (d) An expanded view of spectra at low energies. The solid lines are the fits to power-law energy dependence $|E|^\alpha$. (e) Position dependence of the exponent α obtained by the power-law fitting (blue circles), compared with the result for single twin boundary case. Adopted from Ref. 103.

possibility is to have an imaginary component to avoid vanishing order parameter as shown in Fig. 24(b); as a function of position across the boundary, the order parameter follows an arch trajectory in the complex plane from $s - d$ to $s + d$ through $s + id$ state (see Fig. 24(c)). Such a problem has been first considered by Sigrist *et al.*, who developed a theory for a $d+s$ order parameter in the orthorhombic $\text{YBa}_2\text{Cu}_3\text{O}_{7-\delta}$ high- T_c superconductor with twin boundaries.¹⁷⁴⁾ They found that the imaginary component may appear near twin boundaries in a length scale much longer than the coherence length ξ .

7.2 Evidence from gap structure

One of the consequences of the presence of imaginary component in the superconducting order parameter $\Delta(\mathbf{k}) = \Delta_1(\mathbf{k}) + i\Delta_2(\mathbf{k})$ is that the low-energy quasiparticle excitations given by

$$E_k = \sqrt{(\varepsilon_k - \mu)^2 + |\Delta(\mathbf{k})|^2} = \sqrt{(\varepsilon_k - \mu)^2 + \Delta_1(\mathbf{k})^2 + \Delta_2(\mathbf{k})^2} \quad (6)$$

are strongly modified. In general, the momentum dependence of imaginary part $\Delta_2(\mathbf{k})$ is different from that of real part, so the low-lying excitations that are determined by nodes in $\Delta_1(\mathbf{k})$ are expected to be gapped out.

The detailed position-dependent STM/STS studies in FeSe clean crystals have shown that the nematic twin boundaries can be considered as ideal interfaces with no noticeable structural distortion in an atomic scale.¹⁰³⁾ The low-energy conductance spectra at positions far away from the boundaries have a V shape, indicating the presence of low-lying quasiparticle excitations. In contrast, the STS conductance curves

near a twin boundary show a flattening behavior at low energies, without exhibiting a zero-energy conductance peak that may be expected when the order parameters at neighboring domains change sign without having the imaginary part. As shown in Fig. 25, this flattening behavior is more pronounced at the positions in between two twin boundaries, and the presence of the finite excitation gap is clearly resolved. These observations of the twin-boundary-induced gap opening are consistent with the complex order parameter near the twin boundaries, and the essential features of conductance spectra have been reproduced by theoretical calculations assuming the presence of imaginary component near boundaries.¹⁰³⁾

The low-energy flattening behaviors are found over an extended length scale of $\gtrsim 50$ nm (see Fig. 25), an order of magnitude longer than the averaged in-plane coherence length $\xi_{ab} \approx 5$ nm. This can also be explained by the above theory of complex order parameter, where the characteristic length scale $\bar{\xi}$ can be much longer than the coherence length and diverges when approaching the phase boundary between the time-reversal symmetric $s+d$ state and the TRS broken $s+id$ state in the bulk. This phase boundary is determined by the closeness of transition temperatures of s and d states and by the amount of orthorhombicity. In $\text{YBa}_2\text{Cu}_3\text{O}_{7-\delta}$, the superconducting order parameter is dominated by the d -wave component and the orthorhombicity-induced s -wave component is much smaller. Thus the onset temperature of TRS-breaking state may be much lower than the actual transition temperature, and there have been no report showing clear evidence for such a TRS-breaking state near twin boundaries. This may also be related to the fact that the STM/STS measurements

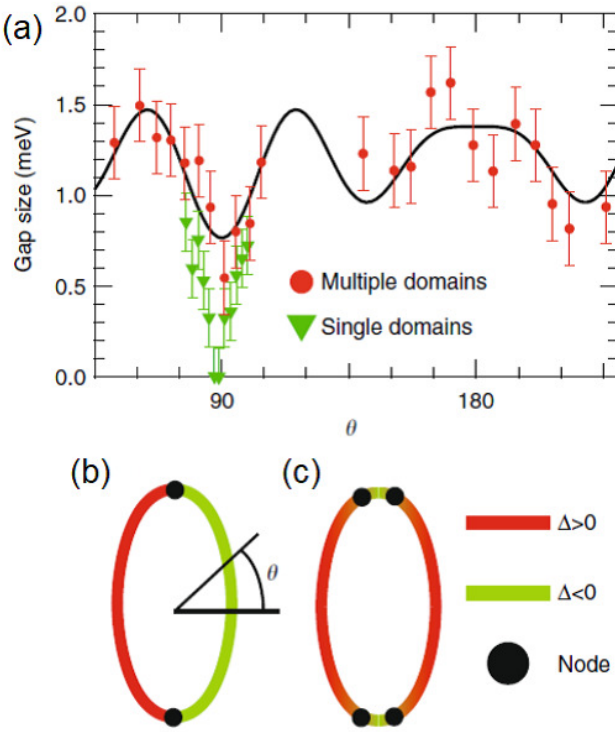


Fig. 26. ARPES measurements of the superconducting gap for the hole band in single-domain and multiple-domain samples of FeSe. (a) Momentum dependence of the gap along the hole Fermi surface ellipsoid in single-domain (green triangles) and multiple-domain (red circles) samples. Solid line is a fit for $\Delta(\mathbf{k})$ in multi-domain sample. (b) Possible positions of nodes for a spin-triplet p -wave state. (c) Possible positions of nodes for a spin-singlet $s+d$ state. Adopted from Ref. 99

in $\text{YBa}_2\text{Cu}_3\text{O}_{7-\delta}$ single crystals are quite challenging due to the difficulties of cleavage. In FeSe, in contrast, the superconducting order parameter has comparable s and d components as discussed in §3, which may lead to the observation of such a state.

In a laser-ARPES study, the angle dependence of superconducting gap in the hole band near the Γ point has been compared between almost single-domain and multiple-domain samples.⁹⁹⁾ In the former, the anisotropic gap reaches almost zero along the long axis of the ellipsoidal underlying Fermi surface, but in the latter the nodes are lifted and the gap minima are found as shown in Fig. 26. This difference in gap structure between samples with different domain structures has been interpreted as another piece of experimental evidence that the finite gap opens near twin boundary. This observation is quite consistent with the STS results, although another laser-ARPES study from a different group does not confirm such a node lifting behavior in samples with multiple domains.¹⁰⁰⁾ The results in multiple-domain samples may depends on the density of twin boundary, and further studies are required to fully understand how $\Delta(\mathbf{k})$ evolves as a function of position near the boundaries.

7.3 Evidence from muon spin rotation (μ SR)

The studies of gap structure can provide only indirect information on the TRS breaking in the superconducting state. A more direct consequence of the TRS breaking is that a finite magnetic field is induced inside the superconducting sample.

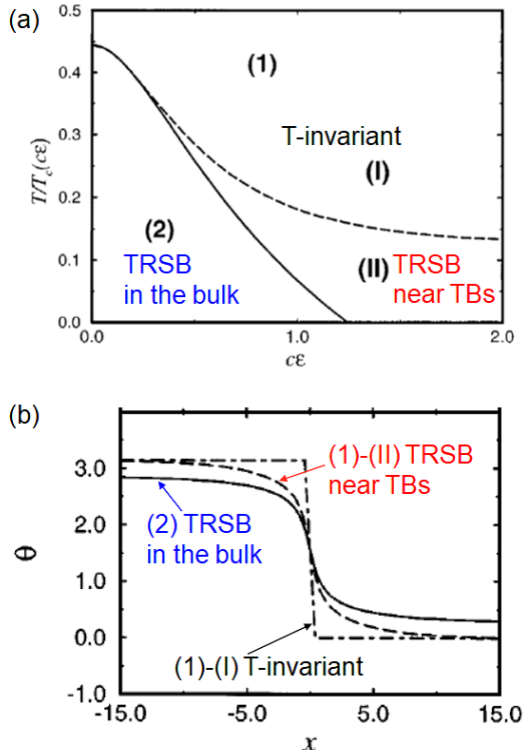


Fig. 27. Phase diagram of TRS-breaking (TRSB) state and corresponding phase difference between d and s components. (a) Temperature versus orthorhombic distortion (ϵ) phase diagram of TRSB states calculated for a $d+s$ state in which s -wave transition temperature is assumed as $0.5T_c$. (b) Phase difference θ between d and s components in a $d+e^{i\theta}s$ state as a function of position near a twin boundary. Three curves correspond to the three phases in (a). In the TRSB state in bulk, phase (2) in (a), the characteristic length scale ξ diverges and a finite phase difference is present deep in the bulk but the dependence near the boundary is similar to that in phase (1)-(II). Adopted from Ref. 174.

This is related to the fact that the $s+id$ and $s-id$ states are energetically degenerate, forming chiral domains, which is analogous to the magnetic domain formation at zero field in ferromagnets. Near the boundaries and the impurities, small but finite magnetic field is induced, which can be detected by experimental probes. The μ SR at zero external field is one of the very sensitive magnetic probes that have been used as direct probes of TRS breaking states in unconventional superconductors. Very recent zero-field μ SR measurements in vapor-grown single crystals of FeSe have shown that while the muon relaxation rate is almost independent of temperature above T_c , which is consistent with the absence of magnetic order in FeSe, it starts to develop just below $T_c \approx 9$ K and continues to increase down to the lowest measured temperature of ~ 2 K.¹⁷⁵⁾

These results also provide strong evidence for a TRS breaking state in FeSe. The onset temperature of the magnetic induction is very close to T_c , which may be explained by the comparable magnitudes of s and d -wave components of the order parameter. The magnitude of the magnetic induction at low temperatures is estimated as small as ~ 0.15 G. Whether this TRS breaking state occurs only in the vicinity of nematic twin boundaries or not cannot be concluded by this μ SR result in FeSe alone. This motivates similar experiments in tetragonal $\text{FeSe}_{1-x}\text{S}_x$, which we discuss below.

7.4 TRSB in the bulk

In the tetragonal phase of $\text{FeSe}_{1-x}\text{S}_x$ ($x > 0.17$), the nematic twin boundaries do not exist, and thus μSR measurements in tetragonal $\text{FeSe}_{1-x}\text{S}_x$ can test TRS breaking inside the bulk. Most recent data of zero-field μSR for $x \gtrsim 0.20$ show similar enhancements of relaxation rate just below $T_c \approx 4$ K, as found in orthorhombic FeSe .¹⁷⁵⁾ This immediately implies that tetragonal $\text{FeSe}_{1-x}\text{S}_x$ has a superconducting state with broken TRS in the bulk. In addition, the observations of finite induced magnetic fields with similar magnitudes in orthorhombic and tetragonal samples suggest that in orthorhombic FeSe TRS breaking occurs not only near the nematic twin boundaries but also deep in the single domains. Indeed, the phase diagram in Fig. 27(a) studied by Sigrist *et al.* for orthorhombic superconductors indicates that the bulk TRS breaking state exists in a wide range of parameters at temperatures below the state of broken TRS only near the twin boundaries.¹⁷⁴⁾ We note that the difference between these two TRS breaking states in the orthorhombic phase is characterized by the presence or absence of small phase difference between s and d components away from the boundaries, and in both cases the position dependence of the phase difference is similarly significant near the twin boundaries as shown in Fig. 27(b). The presence of small phase difference deep in the single domain implies that the tiny gap opening may be present in low-energy quasiparticle excitations. The observation of such a tiny gap requires measurement techniques having very high energy resolutions at very low temperatures.

The TRS breaking in $\text{FeSe}_{1-x}\text{S}_x$ superconductors fulfills one of the strong requirements to realize a novel ultranodal superconducting state with Bogoliubov Fermi surface introduced in the previous section. The μSR experiments under magnetic fields provide further support for this. The transverse-field μSR measurements in type-II superconductors can provide quantitative information on the magnetic penetration depth that characterizes the field distributions around superconducting vortices. The magnitude of penetration depth $\lambda(0)$ is directly related to the density of superconducting electrons, which participate in the supercurrent flows that screen the magnetic field. It is found that the magnitude of $\lambda(0)$ is larger in tetragonal $\text{FeSe}_{1-x}\text{S}_x$ than in orthorhombic FeSe . This shows an opposite trend to that expected from the increase of Fermi surface with S substitution found in quantum oscillations.⁸⁷⁾ This immediately indicates that the density of normal electrons is larger in tetragonal side, whereas the density of superconducting electrons is smaller. This surprising result can be consistently explained by the presence of Bogoliubov Fermi surface in the superconducting ground state for tetragonal side of $\text{FeSe}_{1-x}\text{S}_x$, which reduces the density of superconducting electrons from the normal one. This is also consistent with the large residual density of states observed in the STS⁸⁸⁾ and thermodynamic measurements.¹³⁹⁾

It has been widely established that in unconventional superconductors with line nodes, the application of magnetic field gives rise to a rapid increase of low-energy density of state as discussed in §3.1.2. To some extent, the Bogoliubov Fermi surface is related to the induced zero-energy states at momentum regions close to the original line nodes, owing to virtual “magnetic field” associated with the spontaneous TRS breaking, which may be called as spontaneous Volovik effect.

The reason why such a state can appear only in the tetragonal side of $\text{FeSe}_{1-x}\text{S}_x$ deserves further theoretical and experimental investigations. It is also intriguing to study how this is related to BEC-like superconducting state found in tetragonal $\text{FeSe}_{1-x}\text{S}_x$ as discussed in §4.

8. Topological Superconducting State

8.1 Topological quantum phenomena

This section reviews a rather different aspect of the FeSe -family compound, namely the topological nature. Topological quantum physics is one of the most active areas in recent condensed-matter research, which was ignited by the theoretical prediction of quantum spin-Hall insulator^{176–178)} followed by the experimental verification.¹⁷⁹⁾ Quantum spin-Hall insulator, or 2D topological insulator (TI), is a 2D insulator with a band gap across which the order of the energy bands are inverted from that expected from the energies of the corresponding atomic orbitals. Such a situation can be caused by the spin-orbit interaction. Unlike ordinary insulators, quantum spin-Hall insulators always host spin-polarized helical edge states with a linear energy-momentum dispersion, which can be described by a massless Dirac equation. Such edge states are not related to chemical and structural properties of the edge but are robust and nontrivial in the sense that they are associated with the topological nature of the Bloch wavefunctions due to the band inversion.

The topological nature can be classified by the topological invariant $Z_2 = \{0, 1\}$.¹⁷⁶⁾ The Z_2 invariants in ordinary and quantum spin-Hall insulators are 0 and 1, respectively. The concept of the quantum spin-Hall insulator can be extended in three dimensions, where the topological nature is classified by a set of four Z_2 invariants.^{180,181)} There are two types of 3D TIs, namely the weak TI and the strong TI. The strong TI is an insulator in the bulk but possesses spin-polarized Dirac surface states all over the surfaces, irrespective of the chemical and structural properties of the surface, corresponding to the quantum spin-Hall insulator with the Dirac edge states. In weak TIs, such a Dirac surface state appears only on particular surfaces.

Experimental realization of the quantum spin-Hall insulator was achieved in a HgTe quantum well in 2007,¹⁷⁹⁾ and $\text{Bi}-\text{Sb}$ alloy was identified as a 3D strong TI in 2008.¹⁸²⁾ This was just around the same time when iron-based superconductivity was discovered. Since then, iron-based superconductivity and topological quantum physics have been investigated actively but in parallel, and thus there have been little interaction between them. Nevertheless, in principle, if the concept of topology is applied to superconductors, unique and useful phenomena may emerge. Here the prerequisite is that the superconducting state should be topologically nontrivial. There is growing evidence that Te substitution for Se in FeSe gives rise to topological superconductivity at the surface. In the following we describe the topological phenomena in $\text{FeSe}_{1-x}\text{Te}_x$, in particular paying attention to the Majorana quasiparticle in a vortex core.

8.2 Topological superconductivity and Majorana quasiparticle

We start by briefly introducing topological superconductivity. For details, text books^{183,184)} and a review article¹⁸⁵⁾ are available. A topological superconductor can be viewed

as a superconducting counterpart of TI, where the Cooper-pair wavefunction possesses topologically nontrivial nature. Here, superconducting gap corresponds to the band gap in TI. As similar to the case of TIs, gapless boundary states with linear quasiparticle dispersion appears in topological superconductors. Such quasiparticles can take exactly zero energy, whereas all the quasiparticle states in an ordinary superconductor appear at finite energies. Irrespective of the topological nature, quasiparticle states in the superconducting state are coherent superpositions of electron and hole states. The zero-energy state in the topological superconductor is unique because electron and hole weights are exactly equal. Such a half-electron half-hole state can be regarded as an quasiparticle that is its own antiparticle, which is known as the Majorana quasiparticle. Majorana quasiparticles can be used as a fundamental building block for future fault-tolerant quantum computing,^{185–189)} and thus are attracting much attention.

8.3 Potential platforms for topological superconductivity

Unfortunately, topological superconductivity and therefore Majorana quasiparticles have been elusive. The early proposals mostly focused on chiral *p*-wave superconductors,¹⁹⁰⁾ but such superconductors have yet to be established experimentally. To overcome this situation, there have been proposed several ways to realize effective chiral *p*-wave superconductivity in artificial systems. These include 1D Rashba semiconductor nanowires¹⁹¹⁾ and magnetic-atom chains^{192, 193)} in which superconductivity is induced via the proximity effect from an ordinary *s*-wave superconductor attached.

In 2008, Fu and Kane proposed a novel way to realize 2D topological superconductivity using a heterostructure that consists of ordinary *s*-wave superconductor and 3D strong TI.¹⁸⁹⁾ If superconductivity is induced in the spin-polarized Dirac surface state of TI via the proximity effect, it can be effectively regarded as a chiral *p*-wave superconducting state owing to the spin polarization of the Dirac surface state.¹⁸⁹⁾ Magnetic field applied perpendicular to the interface generates quantized superconducting vortices, in which Majorana quasiparticles would be localized to form Majorana bound state (MBS).¹⁸⁹⁾ Since the MBS has exactly zero energy, it may show up as a zero-bias peak (ZBP) in the LDOS spectra measured by STM/STS, in principle.

However, there are two immediate issues to be addressed to implement actual experiments. First, in the Fu-Kane proposal, topological superconductivity emerges at the interface, which is buried beneath either TI or *s*-wave superconductor films. Therefore, surface sensitive probes such as STM/STS cannot directly access to the MBS, even if it exists. Second, even though the topologically trivial vortex bound states are expected to appear only at finite energies, their lowest energy $\sim \Delta^2/\epsilon_F$ is generally very small $\sim \mu\text{eV}$ (see §4). This is below the energy resolutions of the conventional electron spectroscopy techniques.

The experimental challenges using STM/STS were made on heterostructures where Bi₂Te₃ (TI) thin films were epitaxially grown on the NbSe₂ (*s*-wave superconductor) substrate by molecular-beam epitaxy.¹⁹⁴⁾ The superconducting-gap size observed at the Bi₂Te₃ surface decayed exponentially with increasing film thickness, being consistent with the proximity-induced superconductivity. This suggests that the observed LDOS spectra include information at the interface although it

is indirect. The above mentioned energy-resolution issue remained but other characters, such as spatial dependence of the LDOS spectrum and the spin polarization, were investigated to argue the features that may signify the MBS.¹⁹⁴⁾

Obviously, it is desirable to investigate a system where the MBS is exposed at the surface and is energetically well separated from other trivial vortex bound states. To have topological superconductivity at the surface, one can think of a superconductor that has TI-like character in its normal-state bulk band structure. This is possible if the superconductor is a certain semimetal. As in the case of insulators, semimetals possess a band gap although it meanders in the Brillouin zone and turns out to place the highest energy of the valence band above the lowest energy of the conduction band. If such a meandering band gap is topologically nontrivial, spin-polarized Dirac surface state should emerge and can cross ϵ_F . Further, if the bulk of such a semimetal is an *s*-wave superconductor, the spin-polarized Dirac surface state may turn out to exhibit topological superconductivity due to the self-proximity effect from the bulk. This is the natural realization of the Fu-Kane proposal at the exposed surface, providing a platform to investigate the MBS by surface sensitive probes. There are several candidate materials for such *connate topological superconductors*,¹⁹⁵⁾ such as β -PdBi₂^{196, 197)} and PbTaSe₂.¹⁹⁸⁾ FeSe_{1-x}Te_x can also be categorized as a connate topological superconductor.

8.4 Basic properties of FeSe_{1-x}Te_x

Before discussing topological nature, we briefly summarize basic properties of FeSe_{1-x}Te_x. As in the case of S substitution, Te substitution keeps the compensation condition because Te is isovalent to Se. Sample preparation in the low Te-concentration regime has been challenging because of the possible miscibility gap in $0.1 \lesssim x \lesssim 0.3$.¹⁹⁹⁾ Very few attempts have been reported in this regime using pulsed laser deposition²⁰⁰⁾ and flux growth.²⁰¹⁾ Single crystals with higher x can be obtained by melt-growth technique but they tend to contain excess iron atoms at the interstitial sites, which affect various properties.^{126, 202)} Subsequent annealing process is generally required to remove the excess irons.²⁰³⁾ In short, high quality single crystals are more difficult to prepare in FeSe_{1-x}Te_x than in FeSe_{1-x}S_x and the samples so far available inevitably contain certain amount of disorders.²⁰⁴⁾

As in the case of S substitution, nematicity tends to be suppressed upon Te substitution and diminishes above $x \sim 0.4$.¹⁹⁹⁾ T_c is rather insensitive to x between $0.3 \lesssim x \lesssim 0.7$ and reaches as high as 14.5 K, which is higher than that of FeSe. Unlike FeSe_{1-x}S_x with highly anisotropic superconducting gaps, rather isotropic superconducting gap $\Delta \sim 1.5$ meV has been observed in FeSe_{1-x}Te_x.¹⁰⁷⁾ A double-stripe-type long-range magnetic order appears at $x \gtrsim 0.8$ where the superconductivity diminishes.¹⁹⁹⁾

Besides topological nature discussed in the next subsection, FeSe_{1-x}Te_x is advantageous for the MBS search because it is in a BCS-BEC crossover regime (see §4). ARPES experiments suggest that $\epsilon_F^h \sim \epsilon_F^e \sim 10$ meV.^{125–127)} Considering $\Delta \sim 1.5$ meV,¹⁰⁷⁾ we can estimate the lowest trivial bound-state energy $\Delta^2/2\epsilon_F$ to be as large as 100 μeV . This is still small but enough to distinguish the MBS from the trivial states, if the highest energy resolution STM/STS technology is employed. Therefore, except for the issue associated with

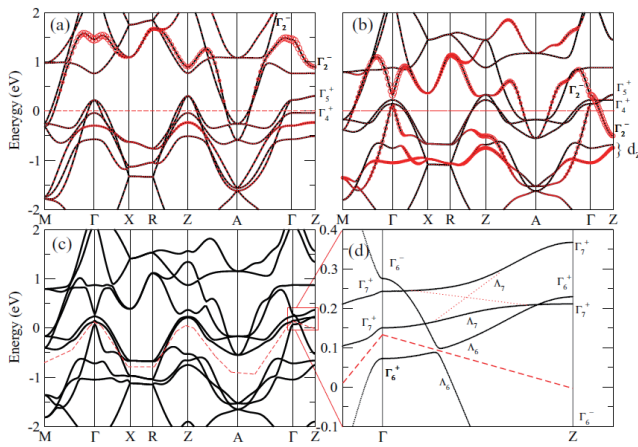


Fig. 28. (a) and (b) Calculated band structures without the spin-orbit interaction for FeSe and for FeSe_{0.5}Te_{0.5}, respectively. The size of the red circle denotes the weight of the chalcogen p_z orbitals. (c) and (d) Calculated band structure for FeSe_{0.5}Te_{0.5} with the spin-orbit interaction. A gap opens at one of the band crossing points along the Γ – Z direction, giving rise to the meandering band gap indicated by the red dashed line. Adopted from Ref. 208.

the disorders, FeSe_{1-x}Te_x provides an excellent platform to search for the MBS.

8.5 Topological phenomena in FeSe_{1-x}Te_x

8.5.1 Band structure and ARPES experiments

Early experimental signature that suggested topological nature of FeSe_{1-x}Te_x was the ZBP found in the tunneling spectra at the interstitial excess irons.²⁰⁵⁾ The ZBP was robust in the sense that it did not split nor shift to finite energies, even if the STM tip was moved away from the excess iron site and even if magnetic fields were applied.²⁰⁵⁾ Such an apparent robustness triggered theoretical analyses of the topological nature of FeSe_{1-x}Te_x, including a proposal of quantum anomalous vortex generated by the magnetic excess iron atom and the spin-orbit interaction.^{206,207)}

First principles band-structure calculations for FeSe and FeSe_{0.5}Te_{0.5} revealed that topological nature indeed emerges upon Te substitution.²⁰⁸⁾ As discussed in §2, band structure of FeSe is complicated but trivial from band topology point of view. Te substitution alters this original band structure through the following two effects. First, Te 5p orbital is more extended than Se 4p orbital. This brings about stronger coupling between chalcogen p_z orbitals and thus larger band dispersion along the Γ – Z direction for the associated band (Fig. 28(b)). This gives rise to additional band crossings along the Γ – Z, resulting in the band inversion at the Z point. Second, because Te is heavier than Se, stronger spin-orbit interaction is expected. Indeed, the spin-orbit interaction opens a gap at one of the additional band crossing points along the Γ – Z and brings about the meandering band gap that is topologically nontrivial (Figs. 28(c) and (d)). The topologically nontrivial nature has been pointed out from different points of view in FeSe_{1-x}Te_x^{209,210)} and also discussed in other iron-based superconductors.^{195,211)}

The above band structure results in the spin-polarized Dirac surface states, which are a hallmark of the topological nature and provide an important platform to host topological superconductivity. Experimental observation of such surface

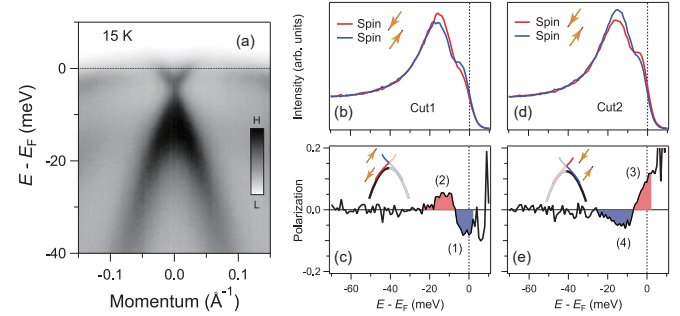


Fig. 29. (a) ARPES intensity map showing the Dirac dispersion at the (001) surface of FeSe_{0.45}Te_{0.55}. (b) and (c) Spin-resolved energy distribution curves and their difference, respectively, taken at one side of the Dirac cone. Spin polarizations are illustrated in the inset of (c). (d) and (e) Same as (b) and (c) but taken at the other side of the cone. Spin polarizations are reversed as being consistent with the helical spin structure. Adopted from Ref. 212.

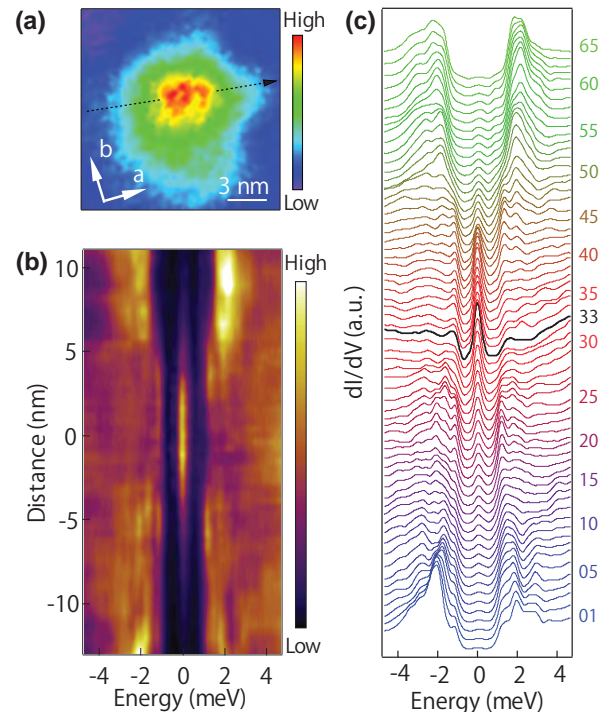


Fig. 30. (a) An image of the vortex obtained by mapping the zero-bias tunneling conductance. Magnetic field of 0.5 T was applied perpendicular to the observed (001) surface. (b) A line profile of the tunneling conductance taken along the black dashed arrow in (a), showing a non-splitting ZBP. (c) A waterfall plot of the same data shown in (b). The spectrum taken at the vortex center is shown in black. Adopted from Ref. 213.

states was challenging because they are in the close vicinity of ε_F and a bulk band, demanding high energy resolution for ARPES along with the spin resolution. Later on, ultra-high resolution laser-based spin ARPES was utilized and the spin-polarized Dirac surface state was successfully observed at the (001) surface of a FeSe_{0.45}Te_{0.55} single crystal (Fig. 29).²¹²⁾

8.5.2 Majorana bound state (MBS) in the vortex core

Given the observation of the spin-polarized Dirac surface state in FeSe_{1-x}Te_x, there is an enough hope that MBS would be formed in the vortex cores. The first STM/STS experiment in this context succeeded in detecting the ZBP in the vortex cores of FeSe_{0.45}Te_{0.55} (Fig. 30).²¹³⁾ Unlike trivial vortex

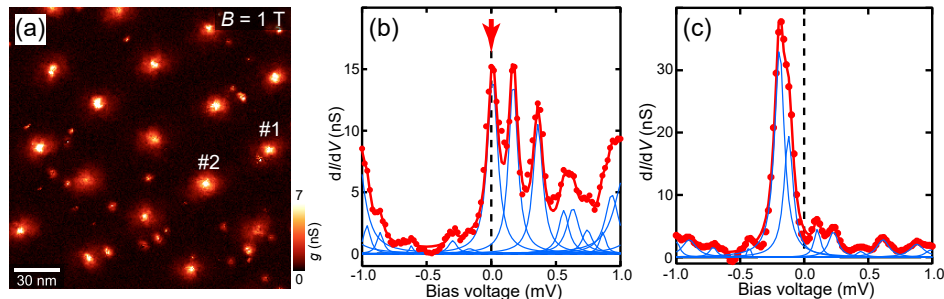


Fig. 31. (a) Zero-energy conductance map g showing of the disordered vortex lattice in $\text{FeSe}_{0.4}\text{Te}_{0.6}$ under magnetic field 1 T applied perpendicular to the observed (001) surface. (b) A high-energy resolution tunneling spectrum taken at the center of the vortex labeled as 1 in (a). A ZBP is observed as indicated by the red arrow. (c) A high-energy resolution tunneling spectrum taken at the center of the vortex labeled as 2 in (a). No ZBP is observed. Adopted from Ref. 204.

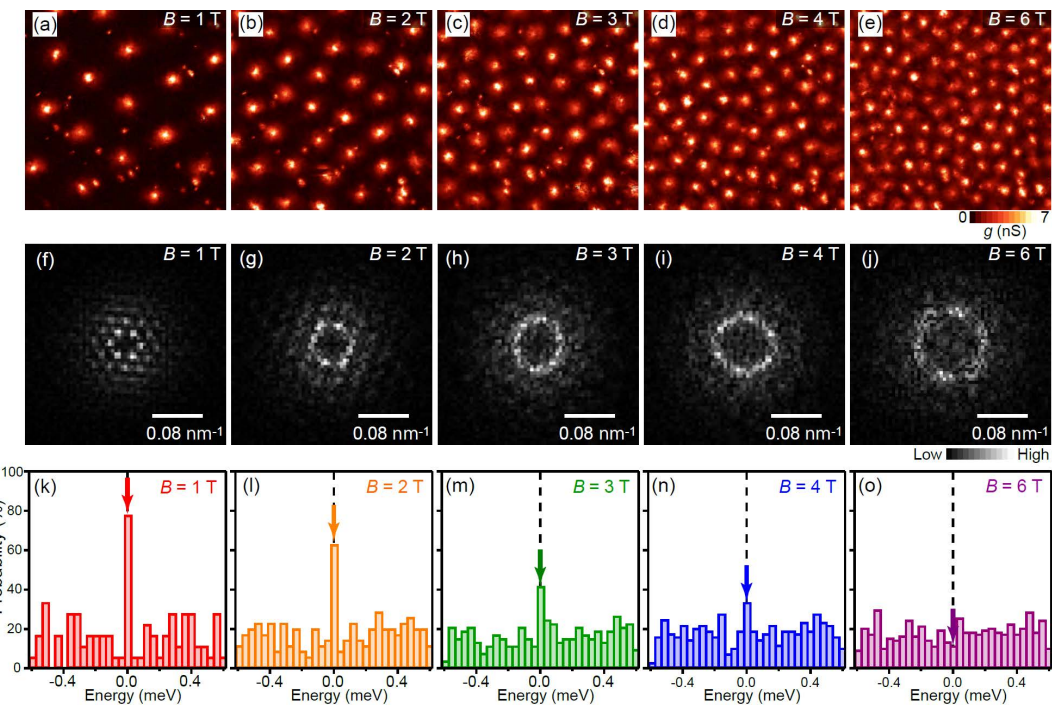


Fig. 32. (a)-(e) Series of zero-energy conductance g map showing the vortex lattice in $\text{FeSe}_{0.4}\text{Te}_{0.6}$ under different magnetic fields. (a) 1 T, (b) 2 T, (c) 3 T, (d) 4 T, (e) 6 T. (f)-(j) Fourier-transformed images from (a)-(e), respectively. Ring-like features mean that there is a distance correlation while the long-range orientation order is lost. (k)-(o) The respective histograms of the appearance frequency of the conductance peaks at given energies. The probability to find the ZBP decreases with increasing magnetic field. Adopted from Ref. 204.

bound states, the observed ZBP stays at zero energy over certain distance from the vortex center and its intensity evolution agrees with that expected from the theoretical spatial profile of the MBS.²¹³⁾ Similar ZBP has also been observed in other iron-based superconductors such as $(\text{Li}_{0.84}\text{Fe}_{0.16})\text{OHFeSe}^{214)}$ and $\text{CaKFe}_4\text{As}_4^{215})$.

The early experiments were done at about 0.5 K with an energy resolution of $\sim 250 \mu\text{eV}^{213, 216}$ which is somewhat larger than the estimated energy of the lowest trivial bound states in the vortex core ($\sim 100 \mu\text{eV}$). Therefore, there still remained an ambiguity whether the observed ZBP indeed represents the MBS or it is a bundle of trivial vortex bound states that are thermally broadened to form an apparent peak at zero energy. In addition, there is a puzzle that the ZBP has been observed only in a fraction of vortices and the rest of vortices do not host the ZBP.^{213, 216)} The problem is that $\text{FeSe}_{1-x}\text{Te}_x$ samples inevitably contain various chemical and electronic dis-

orders as mentioned above. It is important to clarify what kind of disorder governs the ZBP.

Subsequent STM/STS experiments addressed these issues.²⁰⁴⁾ A dilution-fridge-based STM²¹⁷⁾ was employed to reach ultra-low temperatures below 90 mK. As a result, the energy resolution as high as $\sim 20 \mu\text{eV}$ was achieved. This is enough to distinguish the ZBP from the finite-energy trivial bound states and gave a strong constraint that the origin of the ZBP is the MBS²⁰⁴⁾ (Fig. 31). The correlations between vortices with and without the ZBP and various quenched disorders were also investigated systematically.²⁰⁴⁾ Interestingly, any chemical and electronic disorders preexisting in the sample do not affect the presence or absence of the ZBP. Meanwhile, it was found that the fraction of vortices with the ZBP decreases with increasing applied magnetic field, namely increasing vortex density (Fig. 32).²⁰⁴⁾ This suggests that interactions among the MBSs in different vortices may be re-

sponsible for the diminishing ZBP at higher fields. Moreover, since there are two kinds of vortices with and without the ZBP, and the quenched disorders do not play any roles for this distinction, one can infer that the disorder in the vortex-lattice structure may affect the ZBP. Large scale theoretical simulations have been performed to confirm this idea.²¹⁸⁾ The employed model includes the Majorana-Majorana interaction and disorder in the vortex lattice. The results reproduced the basic features of the experimental observations.²¹⁸⁾ Very recently, alternative theoretical model based on the spatially-inhomogeneous Zeeman effect has been proposed.²¹⁹⁾

8.5.3 Search for other Majorana features

Strictly speaking, the ZBP is nothing more than one of the necessary conditions for the MBS. Further challenges to detect the features that are unique to the MBS have been done. The detailed energy spectrum in the vortex core should provide an important clue. As described in §4, quantized energies of the low-lying vortex bound states are given by $\pm\mu_c\Delta^2/\varepsilon_F$, where μ_c are half-odd integers. This is actually the case for the vortices in topologically trivial superconductors. In the case of the topological vortex with the MBS, the quantized sequence becomes $\pm\mu_t\Delta^2/\varepsilon_F$, where μ_t are integers.²²⁰⁾ There is a 1/2 shift between the two cases and the MBS corresponds to the $\mu_t = 0$ state. Experiments have been performed on two kinds vortices in $\text{FeSe}_{1-x}\text{Te}_x$ with and without the ZBP.²²⁰⁾ Half-odd integer and integer level sequences are reported in the former and the latter vortices, respectively, suggesting that $\text{FeSe}_{1-x}\text{Te}_x$ hosts both topologically trivial and non-trivial vortices depending on the location.²²⁰⁾ Apparently, this is incompatible to the observation that the quenched disorders have nothing to do with the ZBP.²⁰⁴⁾ The LDOS spectrum and its spatial evolution are different from vortex to vortex in $\text{FeSe}_{1-x}\text{Te}_x$,^{204,213,216,220)} making it difficult to reach clear conclusions. Experiments on more homogeneous samples are highly desired.

Another signature that is expected to be unique for the MBS is the quantization of the tunneling conductance. It has been theoretically predicted that if the Majorana quasiparticles are involved in the tunneling process, induced resonant Andreev reflections may quantize the tunneling conductance to be $2e^2/h$.²²¹⁾ This has been experimentally tested using the Majorana state formed at the superconducting InSb nanowire covered with a superconductor (Al) shell.²²²⁾ In the case of the MBS in the vortices, STM/STS is a powerful tool but the challenge is that extra-ordinary high tunneling conductance must be achieved to see the expected quantization. Such experiments have been performed in $\text{FeSe}_{1-x}\text{Te}_x$ ²²³⁾ and related compound ($\text{Li}_{0.84}\text{Fe}_{0.16}\text{O}$)OHFeSe.²²⁴⁾ Plateau-like behaviors in the tunneling conductance have indeed been observed. However, the quantization behavior is not so clear yet. Moreover, multiple tunneling paths can exist because of the contributions from the multiple bulk bands. This should affect the quantization condition. Further experimental and theoretical efforts are anticipated.

The vortex core at the surface of $\text{FeSe}_{1-x}\text{Te}_x$ can be regarded as a zero-dimensional boundary in the 2D topological superconductor. Extended 1D boundary, namely the edge, may also host Majorana quasiparticles that can move along the edge. STM/STS has been utilized to detect such dispersing Majorana quasiparticles in $\text{FeSe}_{1-x}\text{Te}_x$.²²⁵⁾ The platform was

a novel naturally-formed domain boundary across which the crystal lattice exhibits a half-unit-cell shift in its structure.²²⁵⁾ The LDOS spectrum observed at the domain boundary is constant as a function of energy, just like an LDOS spectrum of normal metals. It has been argued that this behavior is consistent with the Majorana quasiparticles moving along the 1D channel because of the linear energy-momentum dispersion. The actual edge of the superconducting nano-island may provide more direct opportunity to investigate the details of the dispersing Majorana quasiparticles, and the development of sample fabrication technique is awaited.

9. Summary

In this review, we have discussed a wide variety of exotic superconducting states observed in bulk FeSe-based superconductors. What makes this system unique from other superconductors lies in its peculiar electronic structure, in particular the extremely small Fermi energy, multiband nature and orbital-dependent electron correlations. Because of these properties, spin and orbital degrees of freedom, i.e. magnetism and nematicity, both of which are intimately related to the electron pairing, can be largely tuned by non-thermal parameters, such as pressure, chemical substitution and magnetic field. Therefore, it is natural to consider that many different pairing states emerge as a result of this large tunability.

While more experimental and theoretical works are clearly needed to arrive at a more quantitative description of the data, we feel confident that FeSe-based materials serve as a novel platform of many kinds of exotic pairing states, some of which have never been realized in any other superconductors so far. However, we believe that the following questions regarding the superconducting states in FeSe-based materials remain to be answered.

- The electron Fermi surface still remains for thorough and comprehensive investigations. The precise shape of the Fermi surface and the detailed superconducting-gap properties are yet to be determined.
- The most fundamental question is whether the prevailing s_{\pm} pairing state with the sign reversal between electron and hole Fermi surfaces is realized even in $\text{FeSe}_{1-x}\text{S}_x$ near the nematic QCP, where no sizable spin fluctuations are observed and nematic fluctuations are strongly enhanced.
- Closely related to the above issue, it is an open question why the superconducting gap function dramatically changes at the nematic QCP. In addition, it is also intriguing to clarify whether the highly unusual superconducting gap function in the tetragonal phase of $\text{FeSe}_{1-x}\text{S}_x$ at $x \geq 0.17$ is related to the Bogoliubov Fermi surface.
- It appears that the BCS-BEC crossover properties are largely modified by the multiband and orbital dependent nature. However, we still lack a quantitative description why the pseudogap is hardly observed despite of giant superconducting fluctuations.
- The field-induced superconducting phase can be attributed to the FFLO state. However, it is not a conventional FFLO state because of a large spin polarization and orbital dependent pairing.

- To confirm the time reversal symmetry breaking, more direct measurements, such as the observation of chiral domains in the superconducting state, are desired.
- The correspondence between the zero-energy conductance peak in the vortex core of $\text{FeSe}_{1-x}\text{Te}_x$ and the Majorana bound state should be examined further to find the features that represent "Majorana nature". The obvious goal is to manipulate the Majorana state. More homogeneous samples are indispensable for this purpose.

Evidence for exotic superconducting states of FeSe-based materials have continued to motivate researchers to further investigate and develop novel type superconducting states, which are at the forefront of modern research. We hope that this overview presented here is helpful.

Acknowledgments

The authors acknowledge the collaboration of S. Arsenijević, A. E. Böhmer, J.-G. Chen, A. I. Coldea, I. Eremin, N. Fujiwara, T. Fukuda, A. Furusaki, Y. Gallais, S. K. Goh, T. Hashimoto, S. Hosoi, N. E. Hussey, K. Ishida, K. Ishizaka, K. Iwaya, Y. Kasahara, W. Knafo, Y. Kohsaka, M. Konczykowski, S. Licciardello, H. v. Löhneysen, T. Machida, K. Matsuura, C. Meingast, A. H. Nevidomskyy, K. Okazaki, T. Sasagawa, Y. Sato, T. Shimojima, S. Shin, M. Sigrist, T. Tamegai, T. Terashima, Y. Tsutsumi, Y. J. Uemura, Y. Uwamoto, T. Watanabe, T. Watanuki, T. Watashige, M. D. Watson, T. Wolf, and J. Wosnitza. We especially thank the long-term collaboration with S. Kasahara and Y. Mizukami. We are grateful to D. Agterberg, A. V. Chubkov, P. Dai, R. M. Fernandes, P. J. Hirschfeld, R. Ikeda, J. S. Kim, S. A. Kivelson, H. Kontani, E.-G. Moon, S. Onari, R. Prozorov, J. Schmalian, J. Wang, Y. Yamakawa, and Y. Yanase for valuable discussions. This work was supported by Grants-in-Aid for Scientific Research (KAKENHI) (Nos. JP19H00649, JP18H05227, JP15H02106, JP16H04024, JP25220710, JP25610096, and JP24244057) and Innovative Areas "Quantum Liquid Crystals" (No. JP19H05824), "Topological Material Science" (No. JP15H05852), and "3D Active-Site Science" (No. 26105004) from Japan Society for the Promotion of Science (JPSJ), and JST CREST (Nos. JPMJCR18T2, JP-MJCR16F2).

- 10) J. Paglione and R. L. Greene, Nat. Phys. **6**, 645-658(2010).
- 11) G. R. Stewart, Rev. Mod. Phys. **83**, 1589 (2011).
- 12) *Iron-based Superconductors: Materials, Properties and Mechanism* ed. N. Wang, H. Hosono and P.-C. Dai, (Pan Stanford Publishing, 2012).
- 13) H.-H. Wen and S. Li, Annu. Rev. Condens. Matter Phys. **2**, 121 (2011).
- 14) P.-C. Dai, Rev. Mod. Phys. **87**, 855 (2015).
- 15) T. Shibauchi, A. Carrington, and Y. Matsuda, Annu. Rev. Condens. Matter Phys. **5**, 113 (2014).
- 16) K. Kuroki, S. Onari, R. Arita, H. Usui, Y. Tanaka, H. Kontani, and H. Aoki, Phys. Rev. Lett. **101**, 087004 (2008).
- 17) M. Yi, D. Lu, J. -H. Chu, J. G. Analytis, A. P. Sorini, A. F. Kemper, B. Moritz, S. -K. Mo, R. G. Moore, M. Hashimoto, W. S. Lee, Z. Hussain, T. P. Devereaux, I. R. Fisher, and Z.-X. Shen, Proc. Natl. Acad. Sci. USA **108**, 6878 (2011).
- 18) R. M. Fernandes, A. V. Chubkov, and J. Schmalian, Nat. Phys. **10**, 97 (2014).
- 19) S. Kasahara, H. J. Shi, K. Hashimoto, S. Tonegawa, Y. Mizukami, T. Shibauchi, K. Sugimoto, T. Fukuda, T. Terashima, A. H. Nevidomskyy, and Y. Matsuda, Nature **486**, 382 (2012).
- 20) U. R. Singh, S. C. White, S. Schmaus, V. Tsurkan, A. Loidl, J. Deisenhofer, and P. Wahl, Science Advances **16**, e1500206 (2015).
- 21) E. Thewalt, I. M. Hayes, J. P. Hinton, A. Little, S. Patankar, L. Wu, T. Helm, C. V. Stan, N. Tamura, J. G. Analytis, and J. Orenstein, Phys. Rev. Lett. **121**, 027001 (2018).
- 22) J.-H. Chu, H.-H. Kuo, J. G. Analytis, and I. R. Fisher, Science **337**, 710 (2012).
- 23) H.-H. Kuo, J.-H. Chu, J. C. Palmstrom, S. A. Kivelson, and I.R. Fisher, Science **352**, 958 (2016).
- 24) H. Kontani and S. Onari, Phys. Rev. Lett. **104**, 157001 (2010).
- 25) A. V. Chubkov, M. Khodas, and Rafael M. Fernandes, Phys. Rev. X **6**, 041045 (2016).
- 26) Y. Yamakawa, S. Onari, and H. Kontani, Phys. Rev. X **6**, 021032 (2016).
- 27) C. C. Lee, W. G. Yin, and W. Ku, Phys. Rev. Lett. **103**, 267001 (2009).
- 28) R. Daou, J. Chang, D. LeBoeuf, O. Cyr-Choinière, F. Laliberté, N. Doiron-Leyraud, B. J. Ramshaw, R. Liang, D. A. Bonn, W. N. Hardy, and L. Taillefer, Nature **463**, 08716 (2010).
- 29) V. Hinkov, D. Haug, B. Fauqué, P. Bourges, Y. Sidis, A. Ivanov, C. Bernhard, C. T. Lin, B. Keimer, Science **319**, 597 (2008).
- 30) C. V. Parker, P. Aynajian, E. H. da Silva Neto, A. Pushp, S. Ono, J. Wen, Z. Xu, G. Gu, and A. Yazdani, Nature **468**, 677 (2010).
- 31) Y. Kohsaka, C. Taylor, K. Fujita, A. Schmidt, C. Lupien, T. Hanaguri, M. Azuma, M. Takano, H. Eisaki, H. Takagi, S. Uchida, and J.C. Davis, Science **315**, 1380 (2007).
- 32) Y. Sato, S. Kasahara, H. Murayama, Y. Kasahara, E. -G. Moon, T. Nishizaki, T. Loew, J. Porras, B. Keimer, T. Shibauchi, and Y. Matsuda, Nat. Phys. **13**, 1074 (2017).
- 33) H. Murayama, Y. Sato, R. Kurihara, S. Kasahara, Y. Mizukami, Y. Kasahara, H. Uchiyama, A. Yamamoto, E.-G. Moon, J. Cai, J. Freyermuth, M. Greven, T. Shibauchi, and Y. Matsuda, Nat. Commun. **10**, 3282 (2019).
- 34) K. Ishida, S. Hosoi, Y. Teramoto, T. Usui, Y. Mizukami, K. Itaka, Y. Matsuda, T. Watanabe, and T. Shibauchi, J. Phys. Soc. Jpn. (to be published); arXiv:1908.07167.
- 35) A. E. Böhmer, F. Hardy, F. Eilers, D. Ernst, P. Adelmann, P. Schweiss, T. Wolf, and C. Meingast, Phys. Rev. B **87**, 180505(R) (2013).
- 36) S. Hosoi, K. Matsuura, K. Ishida, H. Wang, Y. Mizukami, T. Watashige, S. Kasahara, Y. Matsuda, and T. Shibauchi, Proc. Natl. Acad. Sci. USA **113**, 8139 (2016).
- 37) D. Huang and J. E. Hoffman, Annu. Rev. Condens. Matter Phys. **8**, 311 (2017).
- 38) Z. Wang, C. Liu, Y. Liu, and J. Wang, J. Phys.: Condens. Matter **29**, 153001 (2017).
- 39) Yu. V. Pustovit and A. A. Kordyuk, Low Temperature Physics **42**, 995 (2016).
- 40) A. I. Coldea and M. D. Watson, Annu. Rev. Condens. Matter Phys. **9**, 125 (2018).
- 41) A. E. Böhmer and A. Kreisel, J. Phys.: Condens. Matter **30**, 023001 (2018).
- 42) J. Maletz, V. B. Zabolotnyy, D. V. Evtushinsky, S. Thirupathaiah, A. U. B. Wolter, L. Harnagea, A. N. Yaresko, A. N. Vasiliev, D. A. Chareev, A. E. Böhmer, F. Hardy, T. Wolf, C. Meingast, E. D. L. Rienks,

- 1) Y. Kamihara, H. Hiramatsu, M. Hirano, R. Kawamura, H. Yanagi, T. Kamiya, and H. Hosono, J. Am. Chem. Soc. **128**, 10012 (2006).
- 2) Y. Kamihara, T. Watanabe, M. Hirano, and H. Hosono, J. Am. Chem. Soc. **130**, 3296 (2008).
- 3) C. Wang, L. Li, S. Chi, Z. Zhu, Z. Ren, Y. Li, Y. Wang, X. Lin, Y. Luo, S. Jiang, X. Xu, G. Cao, and Z. Xu, Europhys. Lett. **83**, 37006 (2008).
- 4) F.-C. Hsu, J.-Y. Luo, K.-W. Yeh, T.-K. Chen, T.-W. Huang, Y.-C. Lee, Y.-L. Huang, Y.-Y. Chu, D.-C. Yan, and M.-K. Wu, Proc. Natl. Acad. Sci. USA **105**, 14262 (2008).
- 5) S. Medvedev, T. M. McQueen, I. A. Troyan, T. Palasyuk, M. I. Eremets, R. J. Cava, S. Naghavi, F. Casper, V. Ksenofontov, G. Wortmann, and C. Felser Nat. Mat. **8**, 630 (2009).
- 6) Q. -Y. Wang, Z. Li, W. -H. Zhang, Z. -C. Zhang, J. -S. Zhang, W. Li, H. Ding, Y. -B. Ou, P. Deng, K. Chang, J. Wen, C. -L. Song, K. He, J. -F. Jia, S. -H. Ji, Y. -Y. Wang, L. -L. Wang, X. Chen, X. -C. Ma, Q. -K. Xue, Chin. Phys. Lett. **29**, 037402 (2012).
- 7) I.I. Mazin, Nature **464**, 183 (2010).
- 8) P. J. Hirschfeld, M. M. Korshunov, and I. I. Mazin, Rep. Prog. Phys. **74**, 124508 (2011).
- 9) A. Chubukov, Annu. Rev. Condens. Matter Phys. **3**, 57 (2012).

- B. Büchner, and S. V. Borisenko, Phys. Rev. B **89**, 220506(R) (2014).
- 43) M. D. Watson, T. K. Kim, A. A. Haghishirad, N. R. Davies, A. McCollam, A. Narayanan, S. F. Blake, Y. L. Chen, S. Ghannadzadeh, A. J. Schofield, M. Hoesch, C. Meingast, T. Wolf, and A. I. Coldea, Phys. Rev. B **91**, 155106 (2015).
- 44) T. Terashima, N. Kikugawa, A. Kiswandhi, E.-S. Choi, J. S. Brooks, S. Kasahara, T. Watashige, H. Ikeda, T. Shibauchi, Y. Matsuda, T. Wolf, A. E. Böhmer, F. Hardy, C. Meingast, H. v. Löhneysen, and S. Uji, Phys. Rev. B **90**, 144517 (2014).
- 45) K. Nakayama, Y. Miyata, G. N. Phan, T. Sato, Y. Tanabe, T. Urata, K. Tanigaki, and T. Takahashi, Phys. Rev. Lett. **113**, 237001 (2014).
- 46) T. Shimojima, Y. Suzuki, T. Sonobe, A. Nakamura, M. Sakano, J. Omachi, K. Yoshioka, M. Kuwata-Gonokami, K. Ono, H. Kumigashira, A. E. Böhmer, F. Hardy, T. Wolf, C. Meingast, H. v. Löneysen, H. Ikeda, and K. Ishizaka, Phys. Rev. B **90**, 121111(R) (2014).
- 47) Y. Suzuki, T. Shimojima, T. Sonobe, A. Nakamura, M. Sakano, H. Tsuji, J. Omachi, K. Yoshioka, M. Kuwata-Gonokami, T. Watashige, R. Kobayashi, S. Kasahara, T. Shibauchi, Y. Matsuda, Y. Yamakawa, H. Kontani, and K. Ishizaka, Phys. Rev. B **92**, 205117 (2015).
- 48) P. Zhang, T. Qian, P. Richard, X. P. Wang, H. Miao, B. Q. Lv, B. B. Fu, T. Wolf, C. Meingast, X. X. Wu, Z. Q. Wang, J. P. Hu, and H. Ding, Phys. Rev. B **91**, 214503 (2015).
- 49) M. D. Watson, T. K. Kim, L. C. Rhodes, M. Eschrig, M. Hoesch, A. A. Haghishirad, and A. I. Coldea Phys. Rev. B **94**, 201107(R) (2016).
- 50) M. D. Watson, A. A. Haghishirad, L. C. Rhodes, M. Hoesch, and T. K. Kim, New J. Phys. **19**, 103021 (2017).
- 51) Y. Yamakawa and H. Kontani, private communication.
- 52) L. Fanfarillo, J. Mansart, P. Toulemonde, H. Cercellier, P. Le Fèvre, F. Bertran, B. Valenzuela, L. Benfatto, and V. Brouet, Phys. Rev. B **94**, 155138 (2016).
- 53) M. Yi, H. Pfau, Y. Zhang, Y. He, H. Wu, T. Chen, Z. R. Ye, M. Hashimoto, R. Yu, Q. Si, D. -H. Lee, Pengcheng Dai, Z. -X. Shen, D. H. Lu, and R. J. Birgeneau, Phys. Rev. X **9**, 041049 (2019).
- 54) S. Kasahara, private communication.
- 55) A. Fedorov, A. Yaresko, T. K. Kim, Y. Kushnirenko, E. Haubold, T. Wolf, M. Hoesch, A. Grüneis, B. Büchner, and S. V. Borisenko, Sci. Rep. **3**, 36834 (2016).
- 56) Y. S. Kushnirenko, A. A. Kordyuk, A. V. Fedorov, E. Haubold, T. Wolf, B. Büchner, and S. V. Borisenko, Phys. Rev. B **96**, 100504(R) (2017).
- 57) L. C. Rhodes, M. D. Watson, A. A. Haghishirad, D. V. Evtushinsky and T. K. Kim, arXiv:2004.04660.
- 58) S. S. Huh, J. J. Seo, B. S. Kim, S. H. Cho, J. K. Jung, S. Kim, C. I. Kwon, Jun Sung Kim, Y. Y. Koh, W. S. Kyung, J. D. Denlinger, Y. H. Kim, B. N. Chae, N. D. Kim, Y. K. Kim, and C. Kim, Commun. Phys. **3**, 52 (2020).
- 59) C. Li, X. Wu, L. Wang, D. Liu, Y. Cai, Y. Wang, Q. Gao, C. Song, J. Huang, C. Dong, J. Liu, P. Ai, H. Luo, C. Yin, G. Liu, Y. Huang, Q. Wang, X. Jia, F. Zhang, S. Zhang, F. Yang, Z. Wang, Q. Peng, Z. Xu, Y. Shi, J. Hu, T. Xiang, L. Zhao, and X. Zhou, arXiv:1911.08753.
- 60) M. Bendele, A. Ichsanow, Yu. Pashkevich, L. Keller, Th. Strässle, A. Gusev, E. Pomjakushina, K. Conder, R. Khasanov, and H. Keller, Phys. Rev. B **85**, 064517 (2012).
- 61) T. Terashima, N. Kikugawa, S. Kasahara, T. Watashige, T. Shibauchi, Y. Matsuda, T. Wolf, A. E. Böhmer, F. Hardy, C. Meingast, H. v. Löhneysen, and S. Uji, J. Phys. Soc. Jpn. **84**, 063701 (2015).
- 62) K. Kothapalli, A. E. Böhmer, W. T. Jayasekara, B. G. Ueland, P. Das, A. Sapkota, V. Taufour, Y. Xiao, E. Alp, S. L. Bud'ko, P. C. Canfield, A. Kreyssig, and A. I. Goldman, Nat. Commun. **7**, 12728 (2016).
- 63) J. P. Sun, K. Matsuura, G. Z. Ye, Y. Mizukami, M. Shimozawa, K. Matsubayashi, M. Yamashita, T. Watashige, S. Kasahara, Y. Matsuda, J.-Q. Yan, B. C. Sales, Y. Uwatoko, J. -G. Cheng, and T. Shibauchi, Nat. Commun. **7**, 12146 (2016).
- 64) K. Matsuura, Y. Mizukami, Y. Arai, Y. Sugimura, N. Maejima, A. Machida, T. Watanuki, T. Fukuda, T. Yajima, Z. Hiroi, K. Y. Yip, Y. C. Chan, Q. Niu, S. Hosoi, K. Ishida, K. Mukasa, S. Kasahara, J.-G. Cheng, S. K. Goh, Y. Matsuda, Y. Uwatoko, and T. Shibauchi, Nat. Commun. **8**, 1143 (2017).
- 65) L. Xiang, U. S. Kaluarachchi, A.E. Böhmer, V. Taufour, M. A. Tanatar, R. Prozorov, S.L. Bud'ko, and P. C. Canfield, Phys. Rev. B **96**, 024511 (2017).
- 66) K. Y. Yip, Y. C. Chan, Q. Niu, K. Matsuura, Y. Mizukami, S. Kasahara, Y. Matsuda, T. Shibauchi, and S. K. Goh, Phys. Rev. B **96**, 020502(R) (2017).
- 67) E. Gati, A. E. Böhmer, S. L. Bud'ko, and P. C. Canfield, Phys. Rev. Lett. **123**, 167002 (2019).
- 68) S. Holenstein, J. Stahl, Z. Shermadini, G. Simutis, V. Grinenko, D. A. Chareev, R. Khasanov, J.-C. Orain, A. Amato, H.-H. Klauss, E. Morenzoni, D. Johrendt, and H. Luetkens, Phys. Rev. Lett. **123**, 147001 (2019).
- 69) P. Reiss, D. Graf, A.A. Haghishirad, W. Knafo, .L Drigo, M. Bristow, A.J. Schofield, and A.I. Coldea, Nat. Phys. **16**, 89 (2020).
- 70) A. V. Chubukov, R. M. Fernandes, and J. Schmalian, Phys. Rev. B **91**, 201105(R) (2015).
- 71) J. K. Glasbrenner, I. I. Mazin, Harald O. Jeschke, P. J. Hirschfeld, R. M. Fernandes, and R. Valentí, Nat. Phys. **11**, 953 (2015).
- 72) F. Wang, S. A. Kivelson, and D. -H. Lee, Nat. Phys. **11**, 959 (2015).
- 73) R. Yu and Q. Si, Phys. Rev. Lett. **115**, 116401 (2015).
- 74) A. E. Böhmer, T. Arai, F. Hardy, T. Hattori, T. Iye, T. Wolf, H. v. Löhneysen, K. Ishida, and C. Meingast, Phys. Rev. Lett. **114**, 027001 (2015).
- 75) Q. Wang, Y. Shen, B. Pan, Y. Hao, M. Ma, F. Zhou, P. Steffens, K. Schmalzl, T. R. Forrest, M. Abdel-Hafiez, X. Chen, D. A. Chareev, A. N. Vasiliev, P. Bourges, Y. Sidis, H. Cao, and J. Zhao, Nat. Mat. **15**, 159-163(2016).
- 76) Q. Wang, Y. Shen, B. Pan, X. Zhang, K. Ikeuchi, K. Iida, A. D. Christianson, H. C. Walker, D. T. Adroja, M. Abdel-Hafiez, X. Chen, D. A. Chareev, A. N. Vasiliev, and J. Zhao, Nat. Commun. **7**, 12182 (2016).
- 77) T. Imai, K. Ahilan, F. L. Ning, T. M. McQueen, and R. J. Cava, Phys. Rev. Lett. **102**, 177005 (2009).
- 78) S.-H. Baek, D. V. Efremov, J. M. Ok, J. S. Kim, J. van den Brink, and B. Büchner, Nat. Mater. **14**, 210 (2015).
- 79) Y. Su, H. Liao, and T. Li, J. Phys. Condens. Matter **27**, 105702 (2015).
- 80) K. Jiang, J. -P. Hu, H. Ding, and Z. Wang, Phys. Rev. B **93**, 115138 (2016).
- 81) P. Wiecki, K. Rana, A. E. Böhmer, Y. Lee, S. L. Bud'ko, P. C. Canfield, and Y. Furukawa, Phys. Rev. B **98**, 020507(R) (2018).
- 82) R. X. Cao, J. Hu, J. Dong, J. B. Zhang, X. S. Ye, Y. F. Xu, D. A. Chareev, A. N. Vasiliev, Bing Wu, X. H. Zeng, Q. L. Wang, and G. Wu, New J. of Phys. **21**, 103033 (2019).
- 83) P. Massat, D. Farina, I. Paul, S. Karlsson, P. Strobel, P. Toulemonde, M.-A. Measson, M. Cazayous, A. Sacuto, S. Kasahara, T. Shibauchi, Y. Matsuda, and Y. Gallais, Proc. Natl. Acad. Sci. USA **113**, 9177 (2016).
- 84) D. D. Scherer, A. C. Jacko, C. Friedrich, E. Şaşoğlu, S. Blügel, R. Valentí, and B. M. Andersen, Phys. Rev. B **95**, 094504 (2017).
- 85) Y. Yamakawa and H. Kontani, Phys. Rev. B **96**, 144509 (2017).
- 86) T. Shimojima, Y. Suzuki, A. Nakamura, N. Mitsuishi, S. Kasahara, T. Shibauchi, Y. Matsuda, Y. Ishida, S. Shin, and K. Ishizaka, Nat. Commun. **10**, 1946 (2019).
- 87) A.I. Coldea, S.F. Blake, S. Kasahara, A. A. Haghishirad, M.D. Watson, W. Knafo, E. S.Chi, A. McCollam, P. Reiss, T. Yamashita, M. Bruma, S. C. Speller, Y. Matsuda, T. Wolf, T. Shibauchi, and A. J. Schofield, npj Quant Mater **4**, 2 (2019).
- 88) T. Hanaguri, K. Iwaya, Y. Kohsaka, T. Machida, T. Watashige, S. Kasahara, T. Shibauchi, Y. Matsuda, Science Advances **4**, eaar6419 (2018).
- 89) Y. Sato, S. Kasahara, T. Taniguchi, X.Z. Xing, Y. Kasahara, Y. Tokiwa, Y. Yamakawa, H. Kontani, T. Shibauchi, and Y. Matsuda, Proc. Natl. Acad. Sci. USA **115**, 1227 (2018).
- 90) S. Licciardello, J. Buhot, J. Lu, J. Ayres, S. Kasahara, Y. Matsuda, T. Shibauchi, and N. E. Hussey, Nature **567**, 213 (2019).
- 91) S. Kasahara, T. Watashige, T. Hanaguri, Y. Kohsaka, T. Yamashita, Y. Shimoyama, Y. Mizukami, R. Endo, H. Ikeda, K. Aoyama, T. Terashima, S. Uji, T. Wolf, H. v. Löhneysen, T. Shibauchi, and Y. Matsuda, Proc. Natl. Acad. Sci. USA **111**, 16309-16313 (2014).
- 92) M. Li, N. R. Lee-Hone, S. Chi, R. Liang, W. N. Hardy, D. A. Bonn, E. Girt, and D. M. Broun, New J. Phys. **18**, 082001 (2016).
- 93) F. Hardy, M. He, L. Wang, T. Wolf, P. Schweiss, M. Merz, M. Barth, P. Adelmann, R. Eder, A.-A. Haghishirad, and C. Meingast, Phys. Rev. B **99**, 035157 (2019).
- 94) L. Jiao, C. -L. Huang, S. Rößler, C. Koz, U. K. Rößler, U. Schwarz, and S. Wirth, Sci. Rep. **7**, 44024 (2017).
- 95) G.-Y. Chen, X. Zhu, H. Yang, and H.-H. Wen, Phys. Rev. B **96**, 064524 (2017).
- 96) A. V. Muratov, A. V. Sadakov, S. Y. Gavrilkin, A. R. Prishchepa, G. S. Epifanova, D. A. Chareev, and M. Pudalov, Physica B **536**, 785 (2018).
- 97) P. Bourgeois-Hope, S. Chi, D. A. Bonn, R. Liang, W. N. Hardy, T. Wolf, C. Meingast, N. Doiron-Leyraud, and L. Taillefer, Phys. Rev. Lett. **117**,

- 097003 (2016).
- 98) Y. Kasahara, Y. Nakajima, K. Izawa, Y. Matsuda, K. Behnia, H. Shishido, R. Settai, and Y. Onuki, *Phys. Rev. B* **72**, 214515 (2005).
 - 99) T. Hashimoto, Y. Ota, H. Q. Yamamoto, Y. Suzuki, T. Shimojima, S. Watanabe, C. Chen, S. Kasahara, Y. Matsuda, T. Shibauchi, K. Okazaki, and S. Shin, *Nat. Commun.* **9**, 282 (2018).
 - 100) D. Liu, C. Li, J. Huang, B. Lei, L. Wang, X. Wu, B. Shen, Q. Gao, Y. Zhang, X. Liu, Y. Hu, Y. Xu, A. Liang, J. Liu, P. Ai, L. Zhao, S. He, L. Yu, G. Liu, Y. Mao, X. Dong, X. Jia, F. Zhang, S. Zhang, F. Yang, Z. Wang, Q. Peng, Y. Shi, J. Hu, T. Xiang, X. Chen, Z. Xu, C. Chen, and X. J. Zhou, *Phys. Rev. X* **8**, 031033 (2018).
 - 101) R. M. Fernandes and J. Schmalian, *Phys. Rev. B* **84**, 012505 (2011).
 - 102) C.-L. Song, Y.-L. Wang, P. Cheng, Y.-P. Jiang, W. Li, T. Zhang, Z. Li, K. He, L. Wang, J.-F. Jia, H.-H. Hung, C. Wu, X. Ma, X. Chen, and Q.-K. Xue, *Science* **332**, 1410-1413 (2011).
 - 103) T. Watashige, Y. Tsutsumi, T. Hanaguri, Y. Kohsaka, S. Kasahara, A. Furusaki, M. Sigrist, C. Meingast, T. Wolf, H. v. Löhneysen, T. Shibauchi, and Y. Matsuda, *Phys. Rev. X* **5**, 031022 (2015).
 - 104) T. Hanaguri, S. Kasahara, J. Böker, I. Eremin, T. Shibauchi, and Y. Matsuda, *Phys. Rev. Lett.* **122**, 077001 (2019).
 - 105) P. O. Sprau, A. Kostin, A. Kreisel, A. E. Böhmer, V. Taufour, P. C. Canfield, S. Mukherjee, P. J. Hirschfeld, B. M. Andersen, and J. C. S. Davis, *Science* **357**, 75 (2017).
 - 106) P. J. Hirschfeld, D. Altenfeld, I. Eremin, and I. I. Mazin, *Phys. Rev. B* **92**, 184513 (2015).
 - 107) T. Hanaguri, S. Niitaka, K. Kuroki, and H. Takagi, *Science* **328**, 474 (2010).
 - 108) Y. Mizukami, M. Konczykowski, Y. Kawamoto, S. Kurata, S. Kasahara, K. Hashimoto, V. Mishra, A. Kreisel, Y. Wang, P. J. Hirschfeld, Y. Matsuda, and T. Shibauchi, *Nat. Commun.* **5**, 5657 (2014).
 - 109) *The BCS-BEC Crossover and the Unitary Fermi Gas*, ed. Wilhelm Zwerger (Springer, 2012).
 - 110) P. Nozières and S. Schmitt-Rink, *J. Low Temp. Phys.* **59**, 195 (1985).
 - 111) Q. Chen, J. Stajic, S. Tan, and K. Levin, *Phys. Rep.* **412**, 1 (2005).
 - 112) M. Randeria, and E. Taylor, *Annu. Rev. Condens. Matter Phys.* **5**, 209 (2014).
 - 113) T. Hashimoto, private communication.
 - 114) D. H. Lee, *Is FeSe a superconductor in the Bose-Einstein condensation limit?* <https://www.condmatclub.org/?p=3264>.
 - 115) A.J. Leggett, in *Modern Trends in the Theory of Condensed Matter*, ed. A. Pekalski and J. Przystawa (Springer, Berlin, 1980) p. 13.
 - 116) Y. J. Uemura, G. M. Luke, B. J. Sternlieb, J. H. Brewer, J. F. Carolan, W. N. Hardy, R. Kadono, J. R. Kempton, R. F. Kiefl, S. R. Kreitzman, P. Mulhern, T. M. Riseman, D. Ll. Williams, B. X. Yang, S. Uchida, H. Takagi, J. Gopalakrishnan, A. W. Sleight, M. A. Subramanian, C. L. Chien, M. Z. Cieplak, Gang Xiao, V. Y. Lee, B. W. Statt, C. E. Stronach, W. J. Kossler, and X. H. Yu, *Phys. Rev. Lett.* **62**, 2317 (1989).
 - 117) V. J. Emery and S. A. Kivelson, *Nature* **374**, 434 (1995).
 - 118) M. Franz, *Nat. Phys.* **3**, 686 (2007).
 - 119) B. Keimer, S. A. Kivelson, M. R. Norman, S. Uchida, and J. Zaanen, *Nature* **518**, 179 (2015).
 - 120) R. Prozorov and R.W. Giannetta, *Supercond. Sci. Technol.* **19**, R41 (2006).
 - 121) A. Pourret, L. Malone, A. B. Antunes, C. S. Yadav, P. L. Paulose, B. Fauqué, and K. Behnia, *Phys. Rev. B* **83**, 020504(R) (2011).
 - 122) K. Hashimoto, K. Cho, T. Shibauchi, S. Kasahara, Y. Mizukami, R. Katsumata, Y. Tsuruhara, T. Terashima, H. Ikeda, M. A. Tanatar, H. Kitano, N. Salovich, R. W. Giannetta, P. Walmsley, A. Carrington, R. Prozorov, and Y. Matsuda, *Science* **336**, 1554 (2012).
 - 123) T. Shimojima, W. Malaeb, A. Nakamura, T. Kondo, K. Kihou4, C.-H. Lee, A. Iyo, H. Eisaki, S. Ishida, M. Nakajima, S. Uchida, K. Ohgushi, K. Ishizaka and S. Shin, *Science Advances* **3**, e1700466 (2017).
 - 124) H. Miao, T. Qian, X. Shi, P. Richard, T. K. Kim, M. Hoesch, L. Y. Xing, X.-C. Wang, C.-Q. Jin, J.-P. Hu, and H. Ding, *Nat. Commun.* **6**, 6056 (2015).
 - 125) Y. Lubashevsky, E. Lahoud, K. Chashka, D. Podolsky, and A. Kanigel, *Nat. Phys.* **8**, 309 (2012).
 - 126) S. Rinott, K. B. Chashka, A. Ribak, E. D. L. Rienks, A. Taleb-Ibrahimi, P. L. Fevre, F. Bertran, M. Randeria, and A. Kanigel, *Science Advances* **3**, e1602372 (2017).
 - 127) K. Okazaki, Y. Ito, Y. Ota, Y. Kotani, T. Shimojima, T. Kiss, S. Watanabe, C.-T. Chen, S. Niitaka, T. Hanaguri, H. Takagi, A. Chainani, and S. Shin, *Sci. Rep.* **4**, 4109 (2015).
 - 128) A. Kostin, P. O. Sprau, A. Kreisel, Y. X. Chong, A. E. Böhmer, P. C. Canfield, P. J. Hirschfeld, B. M. Andersen, and J. C. S. Davis, *Nat. Mater.* **17**, 869 (2018).
 - 129) L. C. Rhodes, M. D. Watson, T. K. Kim, and M. Eschrig, *Phys. Rev. Lett.* **123**, 216404 (2019).
 - 130) H. Suderow, I. Guillamón, J. G. Rodrigo, and S. Vieira, *Supercond. Sci. Technol.* **27**, 063001 (2014).
 - 131) N. Hayashi, T. Isoshima, M. Ichioka, and K. Machida, *Phys. Rev. Lett.* **80**, 2921 (1998).
 - 132) A.I. Larkin, and A. Varlamov, *Theory of Fluctuations in Superconductors* (Clarendon, 2005).
 - 133) J. P. Gaebler, J. T. Stewart, T. E. Drake, D. S. Jin, A. Perali, P. Pieri, and G. C. Strinati, *Nat. Phys.* **6**, 569 (2010).
 - 134) S. Kasahara, T. Yamashita, A. Shi, R. Kobayashi, Y. Shimoyama, T. Watashige, K. Ishida, T. Terashima, T. Wolf, F. Hardy, C. Meingast, H. v. Löhneysen, A. Levchenko, T. Shibauchi, and Y. Matsuda, *Nat. Commun.* **7**, 12843 (2016).
 - 135) H. Yang, G. Chen, X. Zhu, J. Xing, and H.-H. Wen, *Phys. Rev. B* **96**, 064501 (2017).
 - 136) H. Takahashi, F. Nabeshima, R. Ogawa, E. Ohmichi, H. Ohta, and A. Maeda, *Phys. Rev. B* **99**, 060503 (2019).
 - 137) U. Welp, S. Fleshler, W. K. Kwok, R. A. Klemm, V. M. Vinokur, J. Downey, B. Veal, and G. W. Crabtree, *Phys. Rev. Lett.* **67**, 3180 (1991).
 - 138) A. Shi, T. Arai, S. Kitagawa, T. Yamanaka, K. Ishida, A. E. Böhmer, C. Meingast, T. Wolf, M. Hirata, and T. Sasaki, *J. Phys. Soc. Jpn.* **87**, 013704 (2018).
 - 139) Y. Mizukami private communication.
 - 140) G. Blatter, M. V. Feigel'man, V. B. Geshkenbein, A. I. Larkin, and V. M. Vinokur, *Rev. Mod. Phys.* **66**, 1125 (1994).
 - 141) F. Hardy, L. Doussoulin, T. Klein, M. He, A. Demuer, R. Willa, K. Willa, A. -A. Haghghirad, T. Wolf, M. Merz, C. Meingast, and C. Marcenat, arXiv:2004.10848.
 - 142) H. Adachi and R. Ikeda, *Phys. Rev. B* **68**, 184510 (2003).
 - 143) A. V. Chubukov, I. Eremin, and D. V. Efremov, *Phys. Rev. B* **93**, 174516 (2016).
 - 144) S. Rößler, C. Koz, L.Jiao, U. K. Rößler, F. Steglich, U. Schwarz, and S. Wirth, *Phys. Rev. B* **92**, 060505(R) (2015).
 - 145) P. Fulde and R. A. Ferrell, *Phys. Rev.* **135**, A550 (1964).
 - 146) A. I. Larkin and Y. N. Ovchinnikov, *Sov. Phys. JETP* **20**, 762 (1965).
 - 147) Y. Matsuda and H. Shimahara, *J. Phys. Soc. Jpn.* **76**, 051005 (2007).
 - 148) G. Zwicknagl and J. Wosnitza, *Int. J. Mod. Phys. B* **24**, 3915 (2010).
 - 149) J. Wosnitza, *Ann. Phys. (Berlin)* **530**, 1700282 (2018).
 - 150) J. M. Ok, C. I. Kwon, Y. Kohama, J. S. You, J.-h. Kim, Y. J. Jo, E. S. Choi, K. Kindo, W. Kang, E. G. Moon, A. Gurevich, K. S. Kim, and J. S. Kim, arXiv:2003.12351.
 - 151) S. Kasahara, Y. Sato, S. Licciardello, M. Čulo, S. Arsenijević, T. Ottenbros, T. Tominaga, J. Böker, I. Eremin, T. Shibauchi, J. Wosnitza, N. E. Hussey, and Y. Matsuda, *Phys. Rev. Lett.* **24**, 107001 (2020).
 - 152) Y. Matsuda, K. Izawa, and I. Vekhter, *J. Phys.: Condens. Matter* **18**, R705 (2006).
 - 153) T. Watashige, S. Arsenijević, T. Yamashita, D. Terazawa, T. Onishi, L. Opherden, S. Kasahara, Y. Tokiwa, Y. Kasahara, T. Shibauchi, H. v. Löhneysen, J. Wosnitza, and Y. Matsuda, *J. Phys. Soc. Jpn.* **86**, 014707 (2017).
 - 154) K. Izawa, H. Yamaguchi, Y. Matsuda, H. Shishido, R. Settai, and Y. Onuki, *Phys. Rev. Lett.* **87**, 057002 (2001).
 - 155) Y. Kasahara, T. Iwasawa, H. Shishido, T. Shibauchi, K. Behnia, Y. Haga, T.D. Matsuda, Y. Onuki, .M Sigrist, and Y. Matsuda *Phys. Rev. Lett.* **99**, 116402 (2007).
 - 156) H. A. Radovan, N. A. Fortune, T. P. Murphy, S. T. Hannahs, E. C. Palm, S. W. Tozer, and D. Hall, *Nature* **425**, 51 (2003).
 - 157) A. Bianchi, R. Movshovich, C. Capan, P. G. Pagliuso, and J. L. Sarrao *Phys. Rev. Lett.* **91**, 187004 (2003).
 - 158) R. Lortz, Y. Wang, A. Demuer, P. H. M. Böttger, B. Bergk, G. Zwicknagl, Y. Nakazawa, and J. Wosnitza, *Phys. Rev. Lett.* **99**, 187002 (2007).
 - 159) C. C. Agosta, N. A. Fortune, S. T. Hannahs, S. Gu, L. Liang, J. H. Park, and J. A. Schleuter *Phys. Rev. Lett.* **118**, 267001 (2017).
 - 160) M. Kenzelmann, Th. Strässle, C. Niedermayer, M. Sigrist, B. Padmanabhan, M. Zolliker, A. D. Bianchi, R. Movshovich, E. D. Bauer, J. L. Sarrao, and J. D. Thompson, *Science* **321**, 1652 (2008).
 - 161) D. F. Agterberg, M. Sigrist, and H. Tsunetsugu, *Phys. Rev. Lett.* **102**, 207004 (2009).

- 162) Y. Yanase and M. Sigrist, *J. Phys. Soc. Jpn.* **78**, 14715 (2009).
- 163) Y. Hatakeyama and R. Ikeda, *Phys. Rev. B* **91**, 094504 (2015).
- 164) S. Kitagawa, G. Nakamine, K. Ishida, H. S. Jeewan, C. Geibel, and F. Steglich, *Phys. Rev. Lett.* **121**, 157004 (2018).
- 165) C.-w. Cho, J. H. Yang, N. F. Q. Yuan, J. Shen, T. Wolf, and R. Lortz, *Phys. Rev. Lett.* **119**, 217002 (2017).
- 166) K. W. Song and A. E. Koshelev, *Phys. Rev. X* **9**, 021025 (2019).
- 167) J. Kang, R. M. Fernandes, and A. Chubukov, *Phys. Rev. Lett.* **120**, 267001 (2018).
- 168) W. K. Huang, private communication.
- 169) S. Lederer, Y. Schattner, E. Berg, and S. A. Kivelson, *Proc. Natl. Acad. Sci. USA* **114**, 4905 (2017).
- 170) C. Setty, S. Bhattacharyya, Y. Cao, A. Kreisel, and P. J. Hirschfeld, *Nat. Commun.* **11**, 523 (2020).
- 171) C. Setty, Y. Cao, A. Kreisel, S. Bhattacharyya, and P. J. Hirschfeld, arXiv:2004.00621.
- 172) D. F. Agterberg, P. M. R. Brydon, and C. Timm, *Phys. Rev. Lett.* **118**, 127001 (2017).
- 173) J. Kang, A. V. Chubukov, and R. M. Fernandes, *Phys. Rev. B* **98**, 064508 (2018).
- 174) M. Sigrist, K. Kuboki, P. A. Lee, A. J. Millis, and T. M. Rice, *Phys. Rev. B* **53**, 2835 (1996).
- 175) K. Matsurra, private communication.
- 176) C. L. Kane, and E. J. Mele, *Phys. Rev. Lett.* **95**, 146802 (2005).
- 177) C. L. Kane, and E. J. Mele, *Phys. Rev. Lett.* **95**, 226801 (2005).
- 178) B. A. Bernevig, T. L. Hughes, S. -C. Zhang, *Science* **314**, 1757 (2006).
- 179) M. König, S. Wiedmann, C. Brüne, A. Roth, H. Buhmann, L. W. Molenkamp, X. -L. Qi, S. -C. Zhang, *Science* **318**, 766 (2007).
- 180) J. E. Moore, and L. Balents, *Phys. Rev. B* **75**, 121306(R) (2007).
- 181) L. Fu and C. L. Kane, *Phys. Rev. B* **76**, 045302 (2007).
- 182) D. Hsieh, D. Qian, L. Wray, Y. Xia, Y. S. Hor, R. J. Cava, and M. Z. Hasan, *Nature* **452**, 970 (2008).
- 183) B. A. Bernevig, *Topological Insulators and Topological Superconductors* (Princeton University Press, Princeton, 2013).
- 184) K. Nomura, *Toporojikaru zetsuentai · choudendoutai* (Topological insulators, superconductors) (Maruzen, Tokyo, 2016) [in Japanese].
- 185) M. Sato, and Y. Ando, *Rep. Prog. Phys.* **80**, 076501 (2017).
- 186) C. Nayak, S. H. Simon, A. Stern, M. Freedman, and S. Das Sarma, *Rev. Mod. Phys.* **80**, 1083 (2008).
- 187) J. Alicea, *Rep. Prog. Phys.* **75**, 076501 (2012).
- 188) D. A. Ivanov, *Phys. Rev. Lett.* **86**, 268 (2001).
- 189) L. Fu, and C. L. Kane, *Phys. Rev. Lett.* **100**, 096407 (2008).
- 190) N. Read, and D. Greene, *Phys. Rev. B* **61**, 10267 (2000).
- 191) V. Mourik, K. Zuo, S. M. Frolov, S. R. Plissard, E. P. A. M. Bakkers, L. P. Kouwenhoven, *Science* **336**, 1003 (2012).
- 192) S. Nadj-Perge, I. K. Drozdov, J. Li, H. Chen, S. Jeon, J. Seo, A. H. MacDonald, B. A. Bernevig, A. Yazdani, *Science* **346**, 602 (2014).
- 193) H. Kim, A. Palacio-Morales, T. Posske, L. Rózsa, K. Palotás, L. Szunyogh, M. Thorwart, and R. Wiesendanger, *Science Advances* **4**, eaar5251 (2018).
- 194) H. -H. Sun, and J. -F. Jia, *npj Quantum Mater.* **2**, 34 (2017).
- 195) N. Hao, and J. Hu *Natl. Sci. Rev.* **6**, 213 (2019).
- 196) M. Sakano, K. Okawa, M. Kanou, H. Sanjo, T. Okuda, T. Sasagawa, and K. Ishizaka, *Nat. Commun.* **6**, 8595 (2015).
- 197) K. Iwaya, Y. Kohsaka, K. Okawa, T. Machida, M. S. Bahramy, T. Hanaguri, and T. Sasagawa, *Nat. Commun.* **8**, 976 (2017).
- 198) S. -Y. Guan, P. -J. Chen, M. -W. Chu, R. Sankar, F. Chou, H. -T. Jeng, C. -S. Chang, T. -M. Chuang, *Science Advances* **2**, e1600894 (2016).
- 199) Y. Mizuguchi, and Y. Takano, *J. Phys. Soc. Jpn.* **79**, 10 (2010).
- 200) Y. Imai, Y. Sawada, F. Nabeshima, and A. Maeda, *Proc. Natl. Acad. Sci. USA* **112**, 1937 (2015).
- 201) K. Terao, T. Kashiwagi, T. Shizu, R. A. Klemm, and K. Kadokawa, *Phys. Rev. B* **100**, 224516 (2019).
- 202) T. J. Liu, X. Ke, B. Qian, J. Hu, D. Fobes, E. K. Vehstedt, H. Pham, J. H. Yang, M. H. Fang, L. Spinu, P. Schiffer, Y. Liu, and Z. Q. Mao, *Phys. Rev. B* **80**, 174509 (2009).
- 203) Y. Sun, Y. Tsuchiya, T. Taen, T. Yamada, S. Pyon, A. Sugimoto, T. Ekino, Z. Shi, and T. Tamegai, *Sci. Rep.* **4**, 4585 (2014).
- 204) T. Machida, Y. Sun, S. Pyon, S. Takeda, Y. Kohsaka, T. Hanaguri, T. Sasagawa, and T. Tamegai, *Nat. Mater.* **18**, 811 (2019).
- 205) J. -X. Yin, Z. Wu, J. -H. Wang, Z. -Y. Ye, J. Gong, X. -Y. Hou, L. Shan, A. Li, X. -J. Liang, X. -X. Wu, J. Li, C. -S. Ting, Z. -Q. Wang, J. -P. Hu, P. -H. Hor, H. Ding, and S. H. Pan, *Nat. Phys.* **11**, 543 (2019).
- 206) K. Jiang, X. Dai, and Z. Wang, *Phys. Rev. X* **9**, 011033 (2019).
- 207) P. Fan, F. Yang, G. Qian, H. Chen, Y. -Y. Zhang, G. Li, Z. Huang, Y. Xing, L. Kong, W. Liu, K. Jiang, C. Shen, S. Du, J. Schneeloch, R. Zhong, G. Gu, Z. Wang, H. Ding, and H. -J. Gao, arXiv:2001.07376.
- 208) Z. Wang, P. Zhang, G. Xu, L. K. Zeng, H. Miao, X. Xu, T. Qian, H. Weng, P. Richard, A. V. Fedorov, H. Ding, X. Dai, and Z. Fang, *Phys. Rev. B* **92**, 115119 (2015).
- 209) X. Wu, S. Qin, Y. Liang, H. Fan, and J. Hu, *Phys. Rev. B* **93**, 115129 (2016).
- 210) G. Xu, B. Lian, P. Tang, X. -L. Qi, and S. -C. Zhang, *Phys. Rev. Lett.* **117**, 047001 (2016).
- 211) P. Zhang, Z. Wang, X. Wu, K. Yaji, Y. Ishida, Y. Kohama, G. Dai, Y. Sun, C. Bareille, K. Kuroda, T. Kondo, K. Okazaki, K. Kindo, X. Wang, C. Jin, J. Hu, R. Thomale, K. Sumida, S. Wu, K. Miyamoto, T. Okuda, H. Ding, G. D. Gu, T. Tamegai, T. Kawakami, M. Sato, and S. Shin, *Nat. Phys.* **15**, 41 (2019).
- 212) P. Zhang, K. Yaji, T. Hashimoto, Y. Ota, T. Kondo, K. Okazaki, Z. Wang, J. Wen, G. D. Gu, H. Ding, S. Shin, *Science* **360**, 182 (2018).
- 213) D. Wang, L. Kong, P. Fan, H. Chen, S. Zhu, W. Liu, L. Cao, Y. Sun, S. Du, J. Schneeloch, R. Zhong, G. Gu, L. Fu, H. Ding, and H. -J. Gao, *Science* **362**, 333 (2018).
- 214) Q. Liu, C. Chen, T. Zhang, R. Peng, Y. -J. Yan, C. -H. -P. Wen, X. Lou, Y. -L. Huang, J. -P. Tian, X. -L. Dong, G. -W. Wang, W. -C. Bao, Q. -H. Wang, Z. -P. Yin, Z. -X. Zhao, and D. -L. Feng, *Phys. Rev. X* **8**, 041056 (2018).
- 215) W. Liu, L. Cao, S. Zhu, L. Kong, G. Wang, M. Papaj, P. Zhang, Y. Liu, H. Chen, G. Li, F. Yang, T. Kondo, S. Du, G. Cao, S. Shin, L. Fu, Z. Yin, H. -J. Gao, and H. Ding, arXiv:1907.00904.
- 216) M. Chen, X. Chen, H. Yang, Z. Du, X. Zhu, E. Wang, and H. -H. Wen, *Nat. Commun.* **9**, 970 (2018).
- 217) T. Machida, Y. Kohsaka, and T. Hanaguri, *Rev. Sci. Instrum.* **89**, 093707 (2018).
- 218) C. -K. Chiu, T. Machida, Y. Huang, T. Hanaguri, and F. -C. Zhang, *Sci. Adv.* **6**, eaay0443 (2020).
- 219) X. Wu, S. B. Chung, C. Liu, and E. -A. Kim, arXiv:2004.13068.
- 220) L. Kong, S. Zhu, M. Papaj, H. Chen, L. Cao, H. Isobe, Y. Xing, W. Liu, D. Wang, P. Fan, Y. Sun, S. Du J. Schneeloch, R. Zhong, G. Gu, L. Fu, H. -J. Gao, and H. Ding, *Nat. Phys.* **15**, 1181 (2019).
- 221) K. T. Law, P. A. Lee, and T. K. Ng, *Phys. Rev. Lett.* **103**, 237001 (2009).
- 222) H. Zhang, C. -X. Liu, S. Gazibegovic, D. Xu, J. A. Logan, G. Wang, N. van Loo, J. D. S. Bommer, M. W. A. de Moor, D. Car, R. L. M. Op het Veld, P. J. van Veldhoven, S. Koelling, M. A. Verheijen, M. Pendharkar, D. J. Pennachio, B. Shojaei, J. S. Lee, C. J. Palmström, E. P. A. M. Bakkers, S. Das Sarma, and L. P. Kouwenhoven, *Nature* **556**, 74 (2018); *Nature* **581**, E4 (2020).
- 223) S. Zhu, L. Kong, L. Cao, H. Chen, M. Papaj, S. Du, Y. Xing, W. Liu, D. Wang, C. Shen, F. Yang, J. Schneeloch, R. Zhong, G. Gu, L. Fu, Y. -Z. Zhang, H. Ding, and H. -J. Gao, *Science* **367**, 189 (2020).
- 224) C. Chen, Q. Liu, T. Z. Zhang, D. Li, P. P. Shen, X. L. Dong, Z. -X. Zhao, T. Zhang, and D. L. Feng, *Chin. Phys. Lett.* **36**, 057403 (2019).
- 225) Z. Wang, J. Olivares Rodriguez, L. Jiao, S. Howard, M. Graham, G. D. Gu, T. L. Hughes, D. K. Morr, and V. Madhavan, *Science* **367**, 104 (2020).